

Dissertation zur Erlangung des Doktorgrades der Fakultät für Chemie und Pharmazie der
Ludwig-Maximilians-Universität München

Structural characterization of ribosomal complexes involved in ribosome biogenesis and protein folding



Marco Gartmann

aus

Eberswalde-Finow

2009

Erklärung

Diese Dissertation wurde im Sinne von §13 Abs. 3 der Promotionsordnung vom 29. Januar 1998 von Herrn Prof. Dr. Roland Beckmann betreut.

Ehrenwörtliche Versicherung

Diese Dissertation wurde selbständig, ohne unerlaubte Hilfe erarbeitet.

München, am 04.12.2009

Marco Gartmann

Dissertation eingereicht am:

1. Gutachter: Prof. Dr. Roland Beckmann
2. Gutachter: Prof. Dr. Karl-Peter Hopfner

Mündliche Prüfung am: 04.02.2010

Contents

Acknowledgement	5
Summary	6
I. Introduction	7
1. Ribosomes	8
1.1. <i>The role of eIF6 in translation and 60S ribosome biogenesis</i>	9
1.2. <i>Folding inside the ribosomal tunnel</i>	10
2. Molecular chaperones	13
2.1. <i>Ribosome-associated chaperones</i>	14
2.2. <i>The ribosome-associated chaperone triad in <i>S. cerevisiae</i></i>	16
3. Cryo-EM	19
3.1. <i>Cryo-EM and single-particle analysis</i>	19
3.2. <i>Limiting aspects in cryo-EM</i>	22
4. Aims of the study	24
II. Results and Discussion	25
5. Structure of the 60S-eIF6 complex	26
5.1. <i>Specific aim</i>	26
5.2. <i>Sample preparation and reconstitution</i>	27
5.3. <i>Cryo-EM analysis</i>	27
5.4. <i>Mechanism of eIF6-mediated inhibition of ribosomal subunit joining</i> . .	30
5.5. <i>Release of eIF6 by the yeast GTPase Efl1, implications from a model</i> .	31

5.6. <i>Conclusions</i>	33
6. <i>Folding inside the ribosomal tunnel</i>	35
6.1. <i>Specific aim</i>	35
6.2. <i>Sample preparation</i>	36
6.3. <i>Cryo-EM analysis</i>	36
6.4. <i>Secondary structure marker in the tunnel</i>	37
6.5. <i>α-helical nascent chains can fold in distinct tunnel region</i>	38
6.6. <i>Contacts of the nascent chain with the ribosomal tunnel</i>	41
6.7. <i>Conclusions</i>	42
7. <i>Folding beyond the ribosomal tunnel</i>	47
7.1. <i>Specific aim</i>	47
7.2. <i>Purification of RAC</i>	48
7.3. <i>Reconstitution experiments</i>	51
7.4. <i>Cryo-EM analysis</i>	55
7.5. <i>Conclusions</i>	61
III. <i>Materials and Methods</i>	65
8. <i>Biochemical experiments</i>	66
8.1. <i>Molecular cloning</i>	66
8.2. <i>Purification</i>	70
8.3. <i>Reconstitution experiments</i>	76
9. <i>Cryo electron microscopy</i>	77
9.1. <i>Negative stain electron microscopy</i>	77
9.2. <i>Data collection</i>	77
9.3. <i>Data processing</i>	77
IV. <i>Appendix</i>	81
<i>Bibliography</i>	84
<i>Curriculum vitae</i>	95

Acknowledgement

First of all I want to thank professor Roland Beckmann for his support during my work and his ideas. He managed to generate a pleasant working atmosphere in the group with a lot of freedom in the daily business. I joined the group already in Berlin times and I felt included from the first moment. I have to admit that these hearty atmosphere was always present. Especially I want to thank the members of the Beckmann lab, the major reason for the nice working atmosphere not only during the working hours. 'Singing Jens', it was great fun to work with you in the lab, you managed often to make even hard times enjoyable. In particular, I want to thank Thomas for the unforgettable time in our flat share at Rotkreuzplatz and for your helpful discussions, especially in the beginning when I started in Berlin. Thank you Birgit, for the nice cooperation during some projects and the enjoyable coffee breaks. Thanks a lot Christoph, for your enormous help in the RAC project during your Master thesis and beyond. I also want to give thanks to Steffen, for the motivated commitment on the RAC project during his Bachelor thesis. Special thanks to you Daniel, for your great help with calm in the helix project. Thanks to Birgit, for her important help with yeast genetics. Thanks to you, Alex for the nice atmosphere and to you JP, when we fiddled with computers. Thanks to Shashi for the successful cooperation in the Helix project. Thanks for your help, Mario, Michael, Birgitta and Otto. I also want to thank Heidi, who was always willing to help with questions and orders. In this context, I want to thank Joanna and Charlotte for her help. Also thanks to the other members of the lab, Eli, Sole, Anian, Andreas, Julian and Sibylle and the whole Wilson group, which are an enrichment for the group. Especially I want to thank professor Sabine Rospert for the collaboration in the RAC project, and Kristin, as a former member of the Rospert group. Thank you Claus, for the fantastic time during my excursion to the world of Polymerase I.

I want to eminently thank my parents who always supported me during my studies in Potsdam. A tremendous help in all various highs and lows during my thesis was certainly Susanne.

Summary

The synthesis of proteins is an essential process in all living cells that is well regulated and realized by the ribosome. Three separate topics dealing with aspects of ribosomal functions in eukaryotes were studied during this PhD thesis using mainly cryo-electron microscopy (cryo-EM) and single particle data analysis. In the first part the cryo-EM reconstruction of the 60S-eIF6 complex, which is essential in the ribosomal initiation phase revealed the structural basis of the mechanism of eIF6's anti-association activity. In the second part, the structures of two eukaryotic 80S Helix-RNCs showed that α -helix formation is indeed possible in the ribosomal tunnel and that folding is restricted to distinct tunnel regions. Third, the ribosome-associated chaperone triad of yeast composed of RAC and Ssb was studied. A first cryo-EM structure of the 80S-bound RAC could be solved, which opens the door for further studies and a better understanding of co-translational folding events beyond the ribosomal tunnel.

Part I.

Introduction

1. Ribosomes

In all living cells translation of mRNAs into polypeptides is realized by the ribosome. Molecular structures of the large ribosomal subunit revealed that these molecular machines are indeed ribozymes, using mainly RNA to catalyze peptide bond formation in the active center, the peptidyl transferase center (PTC). During the last few years a breakthrough in understanding the mechanism of protein synthesis was achieved by solving a number of ribosomal crystal structures at atomic resolution (Ramakrishnan, 2002). Starting with the first high-resolution structure of an archaean 50S subunit (Ban et al., 2000) and followed by the 30S structure of *T. thermophilus* (Schlunzen et al., 2000; Wimberly et al., 2000). Atomic structures of the complete 70S ribosome in different functional states (Schuwirth et al., 2005; Selmer et al., 2006; Korostelev et al., 2006; Berk et al., 2006) and recently with bound ligands (Blaha et al., 2009; Schmeing et al., 2009; Gao et al., 2009) allowed a detailed understanding of this molecular machine and its interaction with various ligands. Strikingly, a molecular structure of the eukaryotic 80S ribosome is still missing. The bacterial 70S ribosome has a molecular weight (MW) of $\sim 2,4$ MDa and consists of a small 30S and a large 50S subunit. In comparison, eukaryotic 80S ribosomes have a MW of ~ 4 MDa and they are composed of a 40S and 60S ribosomal subunit, which have additional ribosomal proteins and extra rRNA segments, referred to as rRNA expansion segments that are mainly found around the periphery of the subunits. Around 30 % of the total cell mass are ribosomes in bacteria and eukaryotes (Kramer et al., 2009). Bacterial ribosomes synthesize proteins with rates of about 20 aa (amino acids) per second, whereas eukaryotes translate only with a speed of 5-9 aa per second. Protein synthesis is a complicated process that combines high speed with high fidelity (Green & Noller, 1997) and that occurs in four phases: initiation, elongation, termination and ribosome recycling. In each step a large number of specific translation factors cooperate with the ribosome. One of them is eukaryotic IF6 which operates during the initiation phase. But not only protein synthesis is realized by the ribosome, there are data that show a participation of the ribosomal tunnel in folding, by providing an environment that allows formation of secondary structure elements like

α -helices Woolhead et al. (2004); Kosolapov & Deutsch (2009). However, folding occurs in- and outside of the ribosomal tunnel. As soon as the nascent polypeptide has left the ribosomal tunnel, a 'welcome committee' of several factors including chaperones interact co-translationally with the nascent protein chain.

1.1. The role of eIF6 in translation and 60S ribosome biogenesis

Eukaryotic initiation factor 6 (eIF6, p27BBP, Tif6p in *S. cerevisiae*) is an essential 25 kDa protein in archaea (aIF6) and eukaryotes (Si & Maitra, 1999). It is absent in eubacteria and has a sequence identity of 77 % between yeast and humans (Miluzio et al., 2009). In wheat germ and mammalian liver it was originally identified as a ribosomal anti-association factor and therefore classified as translation initiation factor (Russell & Spremulli, 1979; Valenzuela et al., 1982). eIF6 participates in the biogenesis

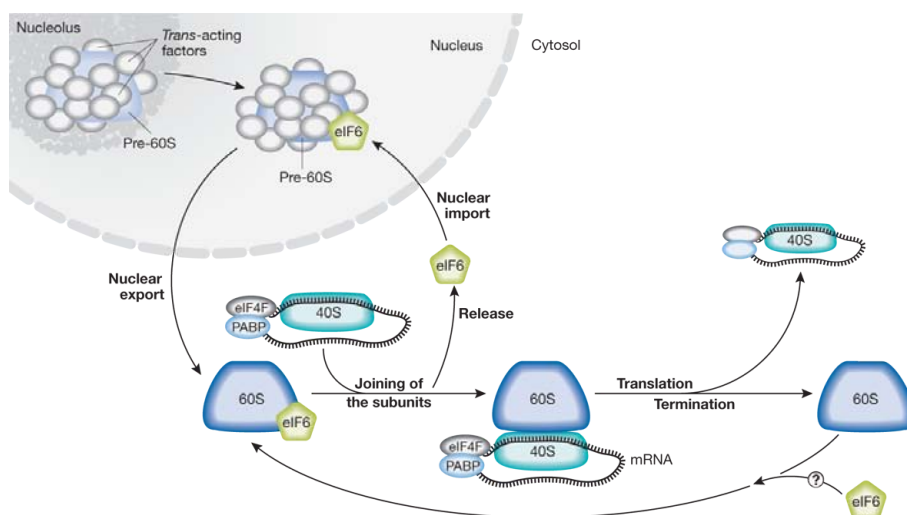


Figure 1.: Functions of eIF6. | In eukaryotes, eIF6 is involved in the biogenesis of ribosomes and in translational control. (from (Miluzio et al., 2009))

of ribosomes as well as in translational control (Fig. 1). During the process of ribosome biogenesis, eIF6 binds to 60S ribosomal subunits and prevents the premature association with the 40S ribosomal subunit to form the 80S initiation complex. The depletion of eIF6 in *S. cerevisiae* is lethal and lead to a slow down of translational activity due to a loss of available free 60S subunits (Si & Maitra, 1999), consistent with its role as anti-association factor. It is localized in the nucleus and in the cytoplasm of yeast and

mammalian cells (Sanvito et al., 1999; Lebreton et al., 2006). In the cytoplasm eIF6 is associated with free 60S particles (Si & Maitra, 1999) and in the nucleus it is part of the 66S pre-ribosomal particles (Horseley et al., 2004), wherefrom it is subsequently exported together with the mature 60S subunits. Nuclear shuttle was shown to be regulated in yeast and mammalian eIF6 by phosphorylation of Ser174 (major site) and Ser175 (minor site) (Basu et al., 2003). In yeast the cytoplasmic release of eIF6 from 60S subunits is promoted by two factors, the GTPase Efl1 (Efl1p) (Senger et al., 2001) and Sdo1 (Sdo1p), the yeast ortholog of the SBDS (Shwachman-Bodian-Diamond syndrome) protein (Menne et al., 2007). By contrast, recycling of eIF6 in mammalian is mediated by a RACK1 dependent PKC stimulation leading to a phosphorylation of eIF6 at Ser235 (Ceci et al., 2003). The characteristic structure of IF6 is called penten and is conserved between yeast and archaea. Five quasi identical α/β subdomains are arranged around an axis with five-fold pseudosymmetry (Groft et al., 2000) that is formed by a central cavity. Interestingly, it has recently been shown that eIF6 can be part of the mammalian RISC complex (Chendrimada et al., 2007) and that it may play important additional roles in global translation (Gandin et al., 2008) and tumorigenesis (Sanvito et al., 2000; Harris et al., 2004).

1.2. Folding inside the ribosomal tunnel

The ribosomal exit tunnel is a universal feature of all ribosomes (Frank et al., 1995; Ban et al., 2000; Morgan et al., 2000; Halic et al., 2006b). The tunnel spans a length of 80-100 Å, on average only 15 Å wide and composed predominantly of ribosomal RNA (rRNA). An overall electronegative potential of the tunnel is consistent with the dominating RNA environment (Lu & Deutsch, 2008; Lu et al., 2007). In addition to rRNA, the extensions of the ribosomal proteins rpL4 and rpL17 (L22p in bacteria) contribute to formation of the tunnel wall, and form a so-called “constriction” where the tunnel narrows to 10 Å ((Ban et al., 2000); 2a). The ribosomal protein rpL39 is present in eukaryotic and archaeal ribosomes, whereas in bacteria the extension of L23p (rpL25 in eukaryotes) occupies a similar position near the exit tunnel. Despite its universality, a functional role for the ribosomal tunnel is only beginning to emerge. For many years, the ribosomal tunnel was thought of only as a passive conduit for the nascent polypeptide chain. However, accumulating evidence indicates that, at least for some nascent chains, the tunnel plays an important and more active role. A number of leader peptides induce translational stalling in response to the presence or absence of an effector molecule, and

thus regulate translation of a downstream gene (Tenson & Ehrenberg, 2002). Leader peptides of SecM, TnaC and ErmC are well-characterized bacterial examples, for which mutations in the leader peptide sequence, or in the interacting ribosomal tunnel components can relieve the translational arrest (Gong & Yanofsky, 2002; Nakatogawa & Ito, 2002; Vazquez-Laslop et al., 2008). All these data imply a direct interaction between specific residues inside the leader peptide with distinct locations of the ribosomal tunnel. Dimensions of the tunnel preclude the folding of domains as large as an IgG domain (~ 17 kDa), whereas α -helix formation seems feasible ((Voss et al., 2006; Hardesty & Kramer, 2001); see also 2b and c). A transmembrane signal anchor sequence is compacted as it

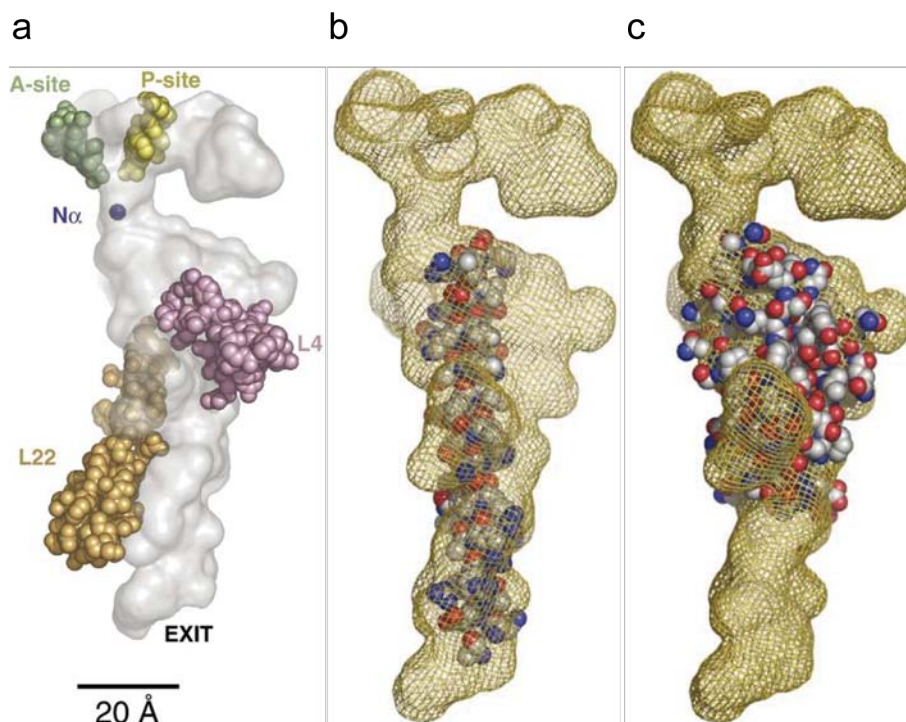


Figure 2.: Ribosomal exit tunnel. | (a) Overview of the ribosomal tunnel based on the structure of the archaeal 50S subunit. Fitting of an α -helix (b) and an IgG domain (c) into the ribosomal tunnel. Sterical clashes appear in (c). (adapted from (Voss et al., 2006))

traverses the tunnel, studied by Fluorescence resonance energy transfer (FRET), which indicates α -helix formation in the tunnel (Woolhead et al., 2004). Interestingly, in this study the compaction of the transmembrane nascent chain was lost upon exiting the tunnel, suggesting that the tunnel itself plays a pivotal role in stabilizing the proposed helical conformation. Independent biochemical analysis also support the potential of the nascent chain to adopt compacted or α -helical conformations inside the tunnel and

have even identified specific regions where compaction is favored (Kosolapov et al., 2004; Lu & Deutsch, 2005b,a). Assuming that folding of secondary structure elements in the ribosomal tunnel is possible, the subsequent action of downstream acting cytosolic chaperones would be influenced, because only unfolded parts are recognized, and thus the tunnel could act as the first part in the folding pathway with chaperone-like function.

2. Molecular chaperones

Many newly synthesized proteins require the assistance of molecular chaperones to efficiently fold into their characteristic three-dimensional structure. Chaperones protect their non-native protein substrates from aggregation and misfolding, but they do not contribute conformational information to the folding process. So the steric information of a protein is encoded in its primary structure and the efficiency of this assisted self-assembly process is enhanced by chaperones (Ellis & Hartl, 1999). Molecular chaperones

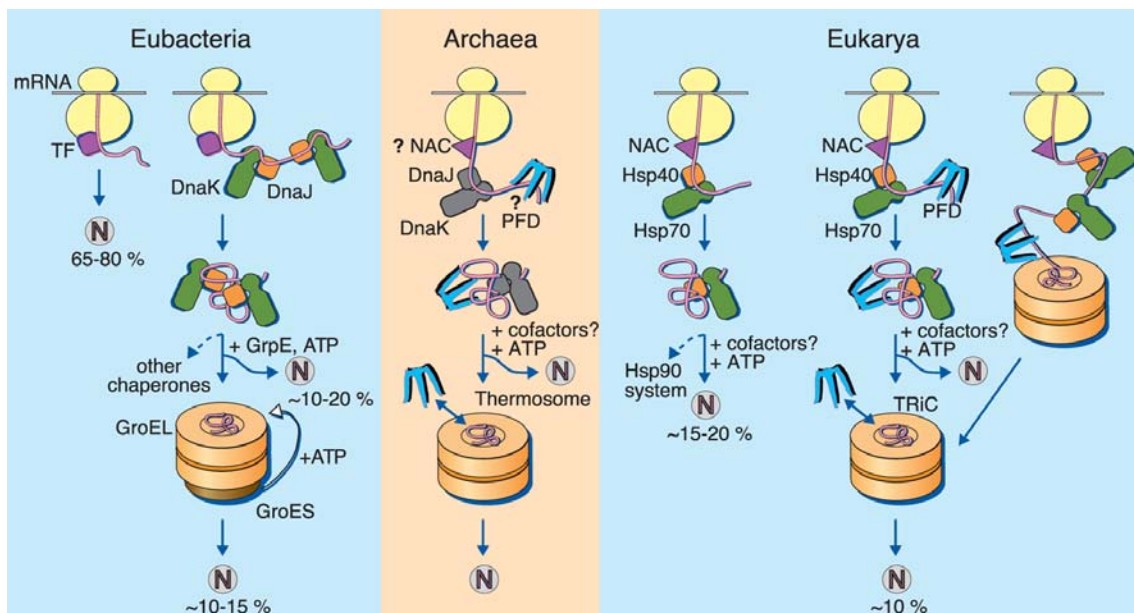


Figure 3.: Cytosolic chaperone system. | Overview of the travel of a newly synthesized protein through the cytosolic chaperone system in the three kingdoms of life. Besides the great diversity of components in chaperone-assisted folding it utilizes by the same principle. (from (Hartl & Hayer-Hartl, 2002))

are present in the cytosol and in eukaryotic organelles such as ER, mitochondria and chloroplasts. Based on the mechanism cytosolic chaperones can be structured in two classes, chaperonins and small chaperones. Chaperonins are large, cylindrical complexes with a defined inner compartment which provides an isolated environment for folding of

protein domains or whole proteins (Horwich et al., 2007). In contrast, the smaller chaperones assist in folding of nascent and newly synthesized polypeptide chains by holding them in a folding competent state (Hartl & Hayer-Hartl, 2002). The first chaperones which interact with newly synthesized proteins already after the nascent chain emerges from the ribosomal exit tunnel are nascent chain-binding chaperones, such as Hsp70s in eukaryotes and trigger factor (TF) in prokaryotes. These chaperones can be subdivided into ribosome-associated chaperones and others which do not directly bind to ribosomes, but act downstream by binding longer nascent chains. In all three kingdoms of life a chaperone network in the cytosol exists, where many newly synthesized proteins are guided through and which involves the action of nascent chain-binding chaperones, and subsequently chaperonins (Figure 3). Misfolding and aggregation of proteins in living cells are known to be the reason for misfolding diseases (Barral et al., 2004) and also involved in aging process (Cohen et al., 2006). Classic examples are neurodegenerative diseases, like Huntington's and Alzheimer's disease in humans. Apart from the potential of chaperones in treatment of diseases associated with protein misfolding they are interesting for many biotechnological processes, especially for recombinant protein production.

2.1. Ribosome-associated chaperones

One of the major challenges for the cell is to prevent aggregation and misfolding of newly synthesized proteins. A highly crowded cytosolic environment with concentrations of 300-400 g/l of proteins and other macromolecules in *E. coli*, leads to excluded volume effects (macromolecular crowding) that is predicted to enhance aggregation of non-native protein chains (van den Berg et al., 1999). In general, macromolecular crowding provides a non-specific driving force for macromolecular association (Minton, 2000) and for interactions with molecular chaperones (Martin & Hartl, 1997). It is thought that during translation on polyribosomes the tendency for aggregation is strongly increased, due to the close proximity of nascent chains of the same type with non-native, unfolded features (Frydman, 2001). This could be a potential reason for the requirement of ribosome-associated chaperones, which act directly at the exit tunnel to prevent aggregation and hold nascent chains in a folding-competent conformation (Hartl & Hayer-Hartl, 2002). The bacterial trigger factor is the best characterized ribosome-associated chaperone. It is only found in prokaryotes and chloroplasts. Trigger factor is a 48 kDa protein that binds to ribosomes in an ATP-independent way in a 1:1 stoichiometry.

Nascent chains as short as 57 aa can be crosslinked to TF, thus it is the first bacterial chaperone interacting with newly synthesized nascent chains (Hesterkamp et al., 1996). The preferred binding motif of TF consists of short hydrophobic sequences enriched in basic and aromatic residues (Patzelt et al., 2001). The bacterial Hsp70 DnaK has partially overlapping chaperone function with TF. A deletion of either DnaK or TF is tolerated by *E. coli* but a double deletion is lethal, showing the functional redundancy amongst the components of the nascent chain-binding chaperone system (Teter et al., 1999; Deuerling et al., 1999; Hartl & Hayer-Hartl, 2002). Recent studies showed that TF interacts with ribosomes and nascent chains in a dynamic reaction cycle, where the presence and nature of the nascent chain itself modulates the timing of TF binding to ribosomes (Kaiser et al., 2006; Raine et al., 2006; Rutkowska et al., 2008). The mechanistic details how TF exactly assists in folding of nascent polypeptide chains has not been clarified yet. The eukaryotic cytosol lacks TF but has evolved a Hsp70-Hsp40 based

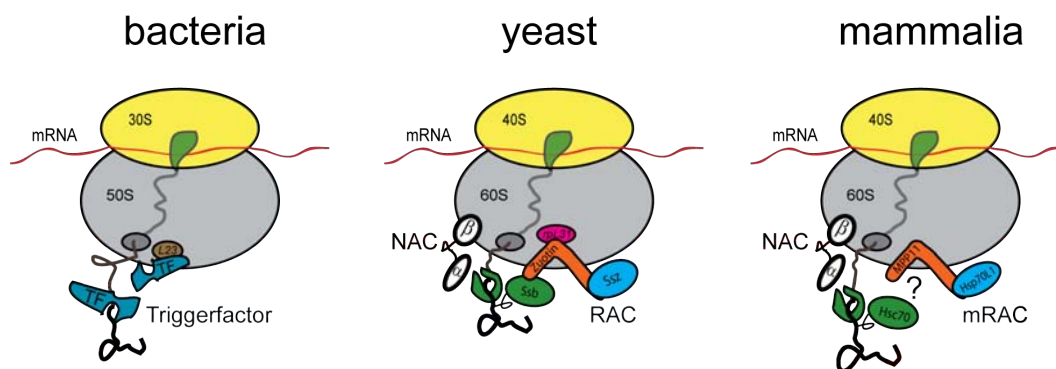


Figure 4.: Ribosome-associated chaperones vary from bacteria to eukaryotes. | Prokaryotes have only TF, whereas eukaryotes dispose of a more complex Hsp70 based system.

system that assists the early folding events (Fig. 4). Besides the Hsp70 based ribosome-binding chaperones, the heterodimeric nascent polypeptide-associated complex (NAC) is present in eukaryotes. The dimeric α/β NAC complex binds to short nascent chains and ribosomes in a 1:1 stoichiometry, whereas its β -subunit mediates ribosome binding (Wiedmann et al., 1994; Fünfschilling & Rospert, 1999; Beatrix et al., 2000). However, there is no direct evidence for a role of NAC in co-translational folding apart from its ribosome interactions.

Hsp70 chaperones

Apart from the ribosome-associated chaperones Ssz (Ssz1p in *S. cerevisiae*) and Ssb1/2 (Ssb1p and Ssb2p in yeast), there are four other non-ribosome-binding Hsp70s known in the cytosol of yeast, namely Ssa1-4 (Ssa1-4p). In addition, there are the Hsp70 relatives Sse1 and Sse2 in the yeast cytosol (Sse1/2p; Hsp110 chaperones). Common structural features of Hsp70 chaperones are the ~ 45 kDa N-terminal ATPase domain (NBD) and a ~ 15 kDa C-terminal substrate binding domain (SBD), which are connected by a flexible linker. The best studied Hsp70 is DnaK from *E. coli*. It binds preferentially to around seven aa long target sequences with a hydrophobic core that is flanked by basic residues (Rüdiger et al., 1997). Binding and release of unfolded substrates to Hsp70 chaperones are controlled by an ATPase cycle, in cooperation with Hsp40 cofactors and nucleotide exchange factors (NEFs). The known NEFs show a great diversity. Interestingly, Hsp110 was shown to act as NEF for canonical Hsp70s in yeast (Dragovic et al., 2006; Raviol et al., 2006). The Hsp70 chaperones are known to be flexible and show an enormous range of conformational changes depending on their nucleotide and substrate binding state (Saibil, 2008). So far, there are only two full-length crystal structures of Hsp70 family members available, one of bovine Hsc70 in a nucleotide-free state (Jiang et al., 2005) and the other of the yeast Sse1 in an ATP-bound state (Liu & Hendrickson, 2007). Hints for a direct substrate interaction of the NEF Sse1 and a cooperation of Hsp110 and Hsp70 in the protein folding cycle was provided by two co-crystal structures of Hsp110-Hsp70 complexes (Polier et al., 2008; Schuermann et al., 2008).

2.2. The ribosome-associated chaperone triad in *S. cerevisiae*

The eukaryotic ribosome-associated factors are best characterized for *S. cerevisiae* (Kramer et al., 2009). Yeast has several ribosome-associated protein biogenesis factors (RPBs) that interact and modify co-translationally the nascent chain, such as chaperones (Ssb and RAC), NAC, SRP (signal recognition particle) and modifying enzymes, for instance methionine aminopeptidase Map (Map1 and Map2) and the N-terminal acetyltransferase NatA, involved in N α -acetylation (Raue et al., 2007). The ribosome-associated chaperones Zuo (Zuo1p or Zuotin), Ssz and Ssb are genetically linked in *S. cerevisiae* and form a functional triad (Gautschi et al., 2002). Yeast mutants lacking either all or one of the three genes show the same phenotype involving slow growth, cold sensitivity and hy-

persensitivity to cations and translation-inhibiting antibiotics, like the aminoglycoside paromomycin (Hundley et al., 2002; Gautschi et al., 2002). The Hsp40 homolog Zuotin and the Hsp70 homolog Ssz form the stable ribosome-associated complex (RAC), which is anchored to yeast ribosomes via Zuotin (Gautschi et al., 2001). RAC is also found in

molecular chaperone	organism	% per ribosome	ribosome binding properties	nascent chain binding properties & Function
TF (ribosome-associated chaperone)	Bacteria	170	- interacts with L23p of the 70S - $K_d \approx 1 \mu\text{M}$	- sequence modulates binding (hydrophobic binding motif) - increased affinity for long chains
DnaK (non-ribosome-binding Hsp70)	Bacteria	100-200	- interacts only with nascent chains	- independent of chain length - can replace TF; deletion of DnaK and TF is lethal in <i>E.coli</i>
Ssb (Ssb1/2) (fungal-specific, ribosome-associated Hsp70)	Eukaryotes	89-300	- binding mainly mediated by nascent chain - salt sensitive interaction with 80S	- no binding motif known and no binding to peptide substrates <i>in vitro</i> - ATPase activity
RAC (ribosome-associated chaperone)	Eukaryotes	27	- Zuo interacts via rpL31 and rRNA - dynamic binding to 80S	- no interaction with nascent chain shown - no ATPase activity of Ssz - J-protein partner of Ssb

Table 1.: Properties of molecular chaperones in bacteria and yeast. (adapted from (Gigione et al., 2009)).

higher eukaryotes, where Hsp70L1 stably interacts with the J-protein MPP11 to form mammalian RAC (mRAC) (Otto et al., 2005) (Fig. 4). The two almost identical Hsp70 chaperones Ssb1/2 differ only in four amino acids. In contrast to RAC, Ssb interacts in addition to the ribosome also with the nascent polypeptide chain (Pfund et al., 1998; Raue et al., 2007). It can be crosslinked to short nascent chains having a length of only 54 aa, meaning that around 10-15 residues emerge from the tunnel (Hundley et al., 2002; Gautschi et al., 2001). Ssb seems to be a fungal-specific Hsp70 with unspecific substrate spectra, showing an overall homology of only 60 % and 48 % to Ssa and DnaK, respectively (Pfund et al., 2001). Zuotin can only act as J-protein partner for Ssb and stimulate its ATP hydrolysis when it is in complex with Ssz, thus forming functional RAC (Huang et al., 2005). RAC is positioned near the ribosomal exit tunnel via a mixed interaction, involving the protein rpL31 (Rpl31p in *S. cerevisiae*, no bacterial homolog) and exposed rRNA elements (Peisker et al., 2008). The function of the unusual Hsp70 Ssz in the chaperone triad of yeast is still enigmatic. It is not an ATPase *in vitro* and the *in vivo* function is independent of RAC formation, as well as the binding of ATP and of peptide substrates (Conz et al., 2007). The current understanding of the RAC-Ssb

chaperone system in yeast is based on biochemical studies. Structural data which could provide an access to a mechanistic understanding of the eukaryotic ribosome-associated chaperone system are still missing so far.

3. Cryo-EM

Cryo-EM has been established during the last years as the third method in structural biology, besides X-ray crystallography and NMR spectroscopy (Frank, 2002). All three methods are capable of solving structures of biological macromolecules to atomic or sub-nanometer resolution. The strength of cryo-EM, compared to NMR and crystallography, is the ability to get structural information of biological complexes in its native environment, using only tiny amounts of sample (μg range) and being not limited by the size of the investigated molecule. A large amount of pure sample is needed to get suitable crystals and also for NMR spectroscopy a pure, highly concentrated and isotope labeled sample is essential. Usually the complex of interest should be bigger than 150 kDa to get the signal-to-noise ratio (SNR) required in cryo-EM. In contrast to cryo-EM, NMR spectroscopy is highly limited by the size of the molecule, whereas X-ray crystallography can manage also huge molecular assemblies, like 70S ribosomes. Still X-ray crystallography and NMR are the only source, being capable to provide atomic details of a biological molecules. Taken together, the three structure methods have their intrinsic assets and drawbacks but cryo-EM is building the bridge to combine atomic information of crystal structures with intermediate resolved cryo-EM maps of the whole complex. The docking of atomic structures into cryo-EM reconstructions allows an interpretation of large multi-component assemblies, such as the ribosome with different ligands, at a molecular level.

3.1. Cryo-EM and single-particle analysis

Biological molecules in cryo-EM are weak phase objects with a poor phase contrast resulting in a low overall contrast, contrary to amplitude objects in negative stain EM. The cryo-EM sample is only embedded in its aqueous environment, and is therefore not stained. The contrast is further decreased by the small difference of the density between protein molecules with only $1,3 \text{ g/cm}^3$ and the surrounding water with 1 g/cm^3 . The sample is usually taken directly from the buffer solution and applied on a carbon coated

grid. Blotting is needed to get thin ice layers. Afterwards the blotted grid is flash frozen in liquid ethane. Rapid cooling of the aqueous sample with rates of more than $100.000^{\circ}\text{C/s}$ leads to the formation of amorphous ice. The random orientation of water molecules, comparable to liquid water, is preserved in the sample and no crystal lattice can be formed during the quick cooling procedure. A dataset of the vitrified sample is collected on a liquid nitrogen cooled transmission electron microscope (TEM) at low dose conditions, using around $20 \text{ e}^{-}/\text{\AA}^2$ (see Fig. 5). Data can be either recorded on CCDcamera or films. In order to digitize them, films have to be scanned at high resolution. With the help of computer clusters the digitized particle images will be aligned, meaning that a common motif contained in the particle images is brought into register. A variety of software packages are available for processing of the data, most widely-used are SPIDER (Frank et al., 1996), EMAN (Tang et al., 2007), IMAGIC (van Heel et al., 1996), FREALIGN (Grigorieff, 2007), XMIPP (Sorzano et al., 2004) and in the near future SPARX (Hohn et al., 2007). The result of the alignment is the information of

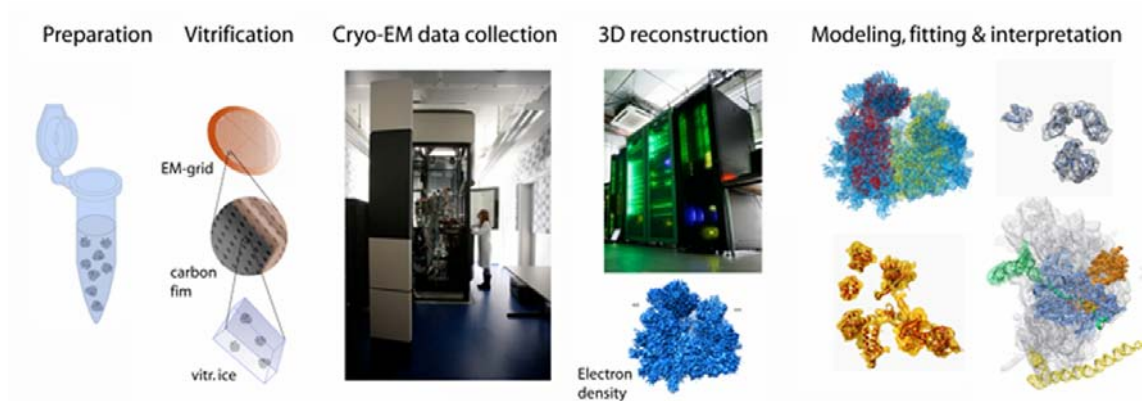


Figure 5.: Workflow in cryo-EM. | The way from sample preparation to 3D reconstruction and final interpretation.

the three Euler angles and the x,y-shifts of each particle in the dataset. In the next step this angular information is used for the backprojection of the particle images to get a 3D reconstruction of the observed molecule. To improve the resolution of the reconstruction a refinement is needed, which is an iterative process with coupled rounds of alignment and backprojection (Fig. 6). If a reference reconstruction is available, first choice are reference-based alignment techniques like projection matching (Penczek et al., 1994). For *ab initio* structure determination, reference-free alignment methods have to be used, such as random conical tilt (Radermacher et al., 1987) or common line methods. A refinement round with SPIDER using projection matching, comprises the following

important steps: filtering and masking of the reference volume, generating pre-aligned stack files of the particle images, CTF (contrast transfer function) distortion of only the generated reference projections, alignment based on calculated CCFs between the reference projections and the experimental projections, and finally a backprojection of the experimental images using the angle and shift informations of the last alignment round (Fig. 6).

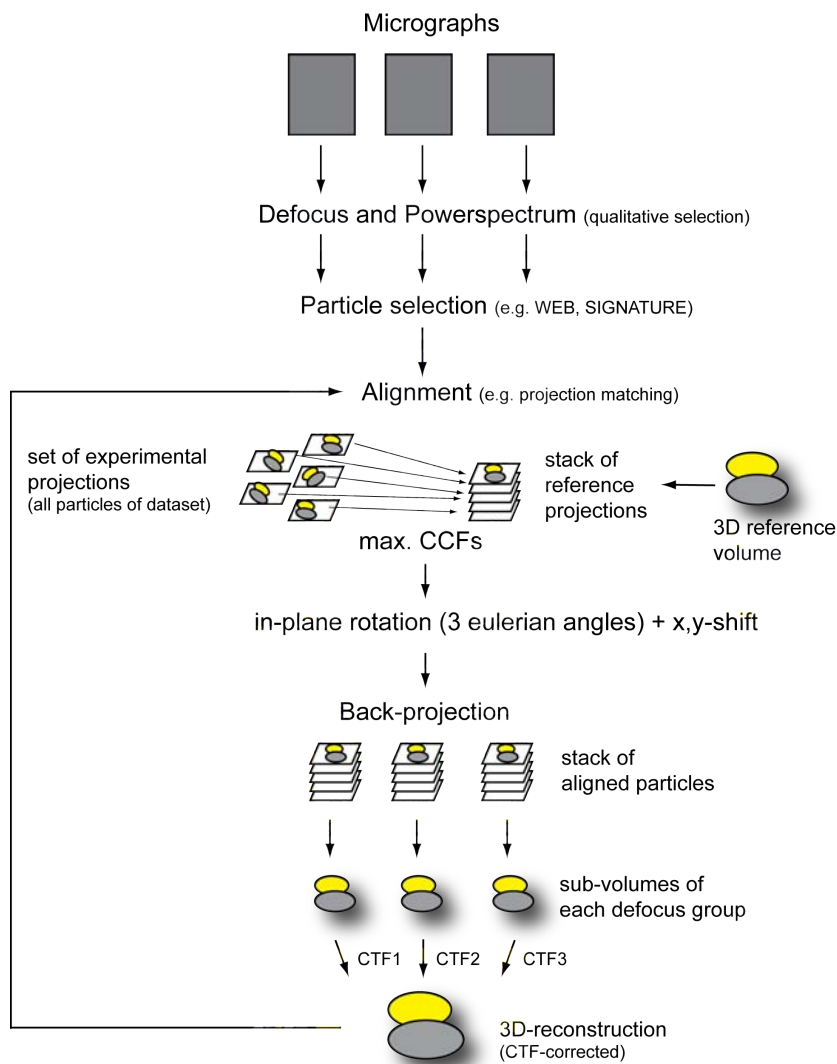


Figure 6.: Reference based refinement with SPIDER. | Single particle analysis using the method of projection matching based on cross-correlation function (CCF) for the refinement of cryo-EM datasets. Flow-chart of processing and reference-based alignment using defocus groups.

3.2. Limiting aspects in cryo-EM

Heterogeneity of datasets

An important assumption in single-particle analysis is that all experimental 2D-projections represent randomly orientated projections derived from the same 3D-structure (Fu et al., 2007), which means that the sample is highly homogeneous in terms of conformation and composition. Cryo-EM reconstructions of heterogeneous datasets with particles that originate from the same molecule in different conformations result in a fragmented or even invisible density for the flexible part of the complex, caused by a loss of density information due to “conformational averaging” (Penczek et al., 2006). However, the reason of the problem in ribosomal dataset is that single particles like the ribosome have on the one hand in most of the cases a much bigger size than the bound ligand and on the other hand the ligand has a small or even no effect on the conformation of the ribosome, which could be used for classification. Therefore, the alignment is dominated by the large projected potential of the ribosome, leading to an averaging effect for bound ligands that have itself conformations independent of the ribosome (Spahn & Penczek, 2009). In principle there are two ways of sorting cryo-EM datasets into sub-datasets (also termed groups or “classes”) according to their similarities: supervised and unsupervised sorting. Supervised sorting is based on prior biochemical or structural knowledge about the sample, therefore an existing 3D reference is used to find particle projections inside the dataset that show high similarity to the offered template and can thus classify the dataset. No additional knowledge is needed for unsupervised sorting methods, because they use only the intrinsic information provided by the dataset and allow a classification without a pre-existing template, whereby bias arising from an external reference is minimized or even avoided (Spahn & Penczek, 2009). Most of the unsupervised sorting methods are based on multivariate statistical analysis at 2D level, such as correspondence analysis (CA), principal component analysis (PCA) or K-means clustering. The sorting method ‘focused classification’ (Penczek et al., 2006) uses first the bootstrap 3D variance analysis to estimate the voxel-by-voxel variance of the dataset to locate regions of high variance, which is then used to place a 3D spherical mask that defines the region for the focused sorting. The classification is focused exclusively on regions with localized high 3D variance, whereby the data are classified into homogeneous datasets on 2D projection level within regions outlined by the respective 2D masks (Penczek et al., 2006). The resulting classified volumes were used as a template for an unsupervised sorting by multireference 3D alignment of the complete dataset (Spahn & Penczek, 2009; Schuette

et al., 2009; Penczek et al., 2006).

Resolution

There is no physical based resolution criterion in cryo-EM, like it exists in X-ray crystallography. The resolution is measured by dividing the dataset into two random half-sets and the independently resulting reconstructions are compared along shells in 3D Fourier space (called Fourier shell correlation, FSC). The most commonly used criterion is the 0.5 FSC cutoff value where the resolution is measured at a CCC (cross-correlation coefficient) threshold value of 0.5, which is equivalent to a S/N ratio of only 1, normally found in unprocessed raw data (Frank, 2002). During the last years some cryo-EM reconstructions achieved near-atomic resolutions, with particles of high symmetry leading the way, for instance GroEL (≥ 4 Å) having a 14-fold symmetry (Ludtke et al., 2008), high symmetric viruses (~ 4 Å) (Chen et al., 2009; Zhang et al., 2008) and unsymmetric particles like the ribosome (~ 6 Å). Clearly, the accuracy of docking stands and falls with the resolution of the underlying cryo-EM reconstruction and thus the provided structural information that is effectively resolved in the map and that can be used for interpretation. Resolution is in general a limiting parameter in cryo-EM that can be partially overcome by the use of hybrid methods, meaning an interpretation by docking of X-ray structures into the cryo-EM map (Rossmann et al., 2005). The fitting can be done either manually by rigid-body docking or with the help of software packages, which can be based on comparative modeling and flexible fitting (Topf et al., 2008) or that use molecular dynamics (MD) simulations with force fields to fit the atomic structure into the density, such as the program MDFF (Trabuco et al., 2008, 2009).

4. Aims of the study

The molecular mechanism of the ribosomal anti-association activity of the small protein eIF6 is not yet understood. One of the aims of this PhD thesis was thus to determine a reconstruction of a 60S-eIF6 complex by means of cryo-EM analysis. The structure of this complex would allow a detailed understanding of eIF6's binding site and most likely reveal informations to understand its anti-association activity and how the release of eIF6 is accomplished for its recycling.

The second project of this thesis was focused on the question if α -helical structure can fold inside the ribosomal tunnel. Up to now, this long-standing question has been addressed exclusively with biochemical and biophysical methods, indicating that secondary structure elements can indeed form inside the tunnel. In this part of the work we aimed to analyze a well characterized α -helical element as part of the nascent chain inside the ribosomal tunnel, using cryo-EM and single particle analysis, to provide structural based evidence to the problem. The co-translational formation of secondary structure in the very first environment of a 'new-born' protein would extend the view of the ribosomal tunnel towards a chaperone-like function that could have important implications for the recognition of signal-sequences and for chaperone assisted folding events beyond the ribosomal tunnel.

The aim of the third part of this work was to characterize the co-translational acting chaperone triad of yeast, consisting of RAC and Ssb, with the help of different structural techniques. Structural data of eukaryotic ribosome-associated chaperones are still missing, which would enable us to understand the function and the interplay of this Hsp70 based chaperone system. The results could be compared to the well characterized but more simpler system of the bacterial trigger factor that is currently used as a basis for models of co-translational acting factors at the ribosomal tunnel exit and could possibly help to extend the understanding of ribosome-associated factors in eukaryotes.

Part II.

Results and Discussion

5. Structure of the 60S-eIF6 complex

5.1. Specific aim

Most regulation takes place at the first stage of translation during the phase of initiation (Sonenberg & Hinnebusch, 2009). Allocation of free 60S ribosomal subunits into the translation cycle is a prerequisite for initiation that needs to be regulated. The conserved and essential protein eIF6 is known to act as a ribosomal anti-association factor and prevents unregulated association of 40S and 60S subunits to inactive 80S particles.

So far, the molecular basis of the diverse eIF6 activities *in vivo*, involving its interaction with the 60S subunit and the resulting ribosomal anti-association activity are only poorly understood (Miluzio et al., 2009). The aim of this study was to gain a better understanding of the molecular basis that underlie its anti-association activity. For this reason, a homogeneous 60S-eIF6 complex from *S. cerevisiae* was studied using cryo-EM and single-particle analysis.

5.2. Sample preparation and reconstitution

The two components of the 60S-eIF6 complex were separately purified (Michael Blau). The full length gene *Tif6* that encodes the protein eIF6 from *S. cerevisiae* was cloned into a pCRT7/NT-TOPO vector. eIF6 was heterologous overexpressed in *E. coli* BL21(DE3) cells and purified via a N-terminal His₆-tag. After induction with IPTG, the cells were grown overnight at room temperature (RT). Cells were harvested by centrifugation, resuspended in lysis buffer and subsequently lysed. The lysate was cleaned by centrifugation and loaded onto a His-Talon column for purification. Eluted fractions were pooled and finally purified using gel filtration. Purified eIF6 was checked for activity with an anti-association activity assay, as described previously (Si & Maitra, 1999; Groft et al., 2000). Yeast 80S ribosomes were incubated with ten fold excess of eIF6 at 30°C for 5 minutes in dissociation buffer, containing 250 mM KCl and 1 mM Mg(OAc)₂. The reaction was then diluted to around 5 mM Mg(OAc)₂ and loaded onto a 5-30 % sucrose gradient. The 60S peak was fractionated and large ribosomal subunits were pelleted by ultra-centrifugation in a next step. Pellets were resuspended in buffer, containing 100 mM KCl and 2.5 mM Mg(OAc)₂. Samples for cryo-EM were prepared using the pelleted 60S subunits, which were mixed with around five fold excess of eIF6 to finally reconstitute the 60S-eIF6 complex in low salt buffer A, containing 100 mM KCl and 2.5 mM Mg(OAc)₂ (for details see Material and Methods).

5.3. Cryo-EM analysis

A dataset of the 60S-eIF6 complex was collected under low dose conditions on a nitrogen cooled Tecnai F30 field emission gun electron microscope. Initially, the dataset yielded to 107,000 particles after particle selection with the programs WEB and SIGNATURE (Chen & Grigorieff, 2007). The SPIDER software package (Frank et al., 1996) was used to further process the data. The 60S-eIF6 dataset was used for the final CTF-corrected 3D-reconstruction with a determined resolution of 11.8 Å, according to 0.5 FSC criterion (8.5 Å, 3σ criterion) (Fig. 7b). The cryo-EM reconstruction of the 60S-eIF6 complex from *S. cerevisiae* reveals an additional and characteristic five-fold density for eIF6 in the intersubunit space of the 60S ribosomal subunit (Fig. 7a). The pseudosymmetric star-like pentain structure (Groft et al., 2000) of eIF6 is resolved by the cryo-EM map (Fig. 7c). Thus the map allows to locate and interpret the binding site of eIF6 on the 60S (Fig. 7d). The ribosomal protein rpL23 (RpL23p in *S. cerevisiae*, L14p in

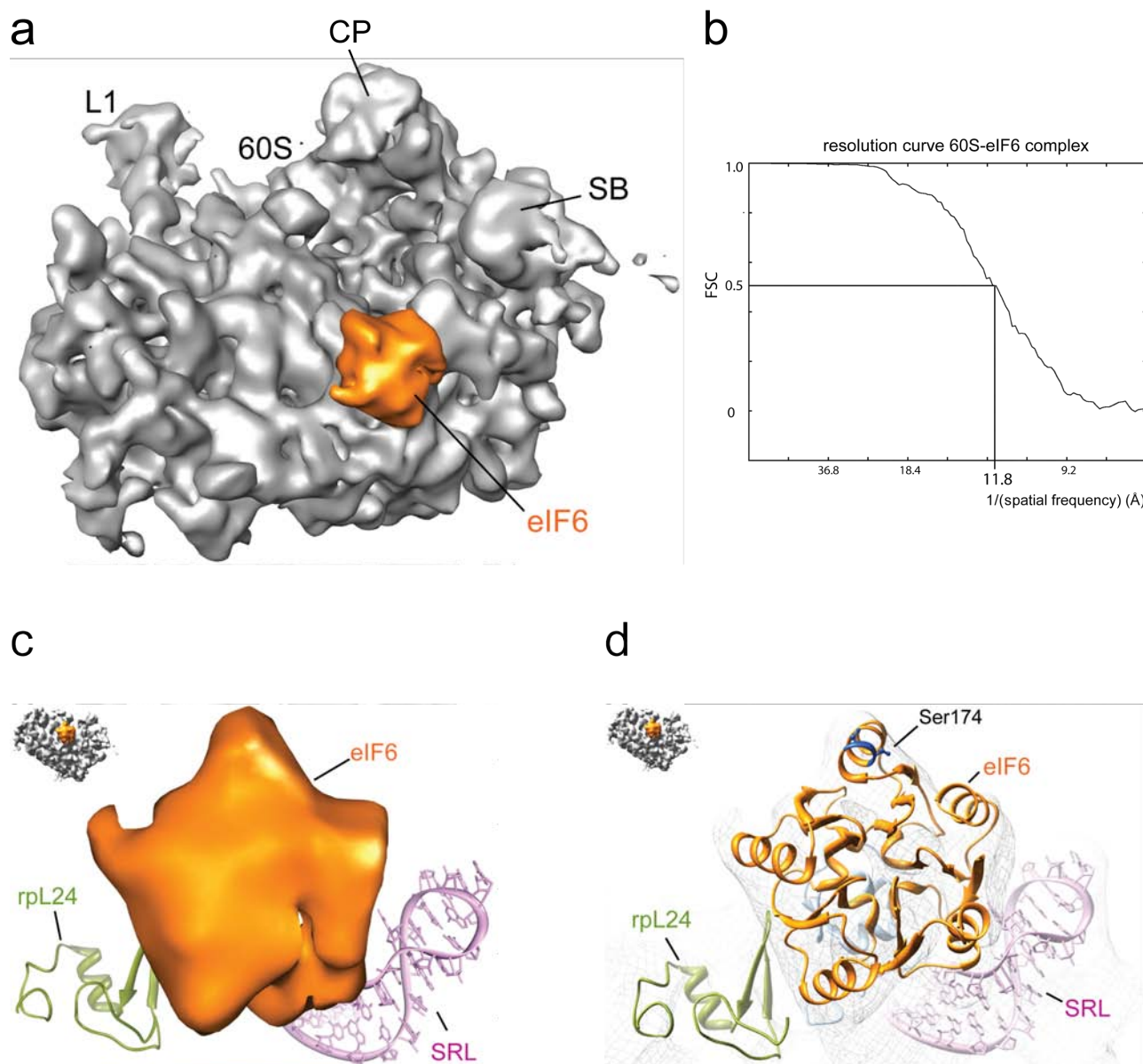


Figure 7.: Cryo-EM reconstruction and docking of eIF6. | (a) Localization of eIF6 (orange) in the cryo-EM reconstruction of the 60S-eIF6 complex. The map is shown in the classical crown view. (b) Resolution curve with 0.5 FSC cutoff marked. (c) Isolated eIF6 density. (d) Fitted eIF6 structure docked into the EM-density (mesh). (60S (gray); eIF6 (orange))

E. coli) can be identified as the main interaction partner of eIF6, which is located at the intersubunit surface of the 60S. This binding site appears to be conserved between eukaryotes and archaea, since it is in agreement with a similar binding site that has recently been suggested for the archaeal aIF6 on the basis of chemical cross-linking and RNA protection experiments (Benelli et al., 2009). The crystal structure of eIF6 from *S. cerevisiae* (PDB entry 1G62, Groft et al. (2000) was taken as basis for flexible fitting into the assigned EM density for eIF6, using the software Flex-EM (Topf et al., 2006). The eIF6 binding interface with the 60S is in good agreement with previously published

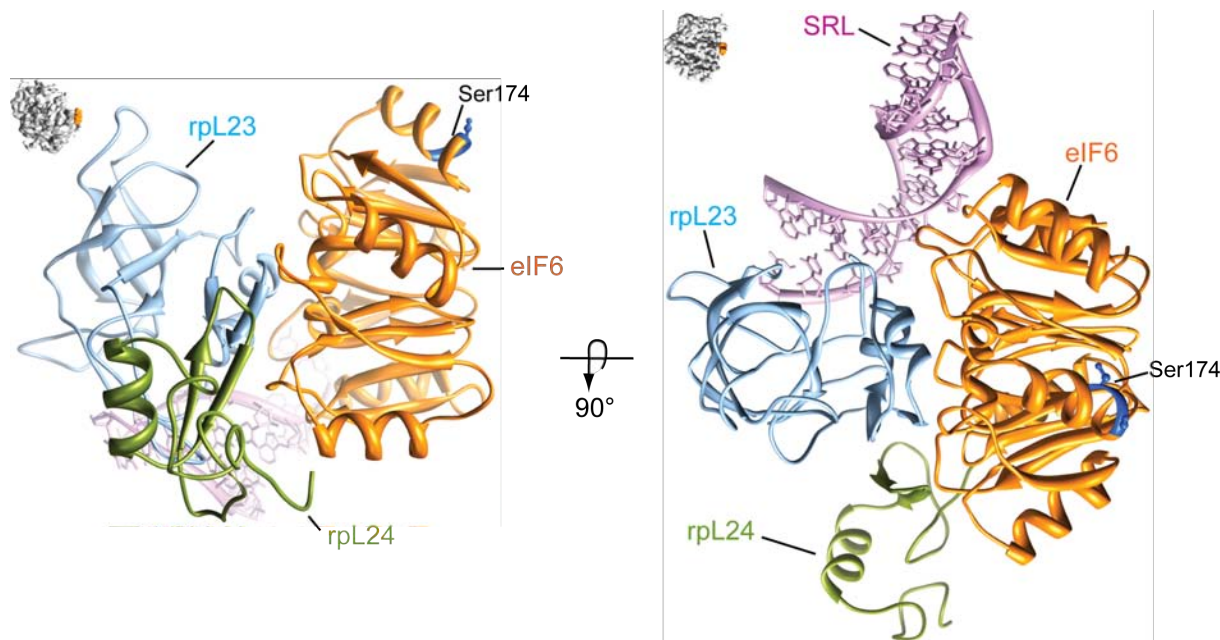


Figure 8.: eIF6 binding site. | Side views, showing the eIF6 binding site on the 60S subunit. Thumbnails show the respective orientation. Note the phosphorylation site Ser174 and the main binding partner rpL23.

genetic data. The region of the TIF6 suppressor mutations that rescue *sdo1Δ* cells were found on the same site as the assigned eIF6 binding region (Menne et al., 2007). To fit the density, the C-terminal part of rpL23 was adjusted leading to a small inward movement of the helical C-terminus of rpL23 relative to the conformation observed in the 80S ribosome. The hydrophobic C-terminal interaction surface of rpL23 is highly conserved and interacts with the helical binding region of eIF6, both of them show a high degree of conservation. In addition, the neighboring ribosomal protein rpL24 (RpL24p in *S. cerevisiae*, L24e in *H. marismortui*) and the highly conserved sarcin-ricin loop (SRL) contribute in the interaction with eIF6 (Fig. 8).

5.4. Mechanism of eIF6-mediated inhibition of ribosomal subunit joining

The anti-association activity of eIF6 is preventing that the 40S subunit binds prematurely to the 60S ribosomal subunit. How can this essential function be accomplished, by the binding of eIF6 to the 60S ribosomal subunit?

When the 40S subunit in its 80S-bound conformation is superimposed with the eIF6-60S complex, it is evident that both binding partners share a common binding region with the 60S subunit and can therefore not bind together (Fig. 9). A large part of the

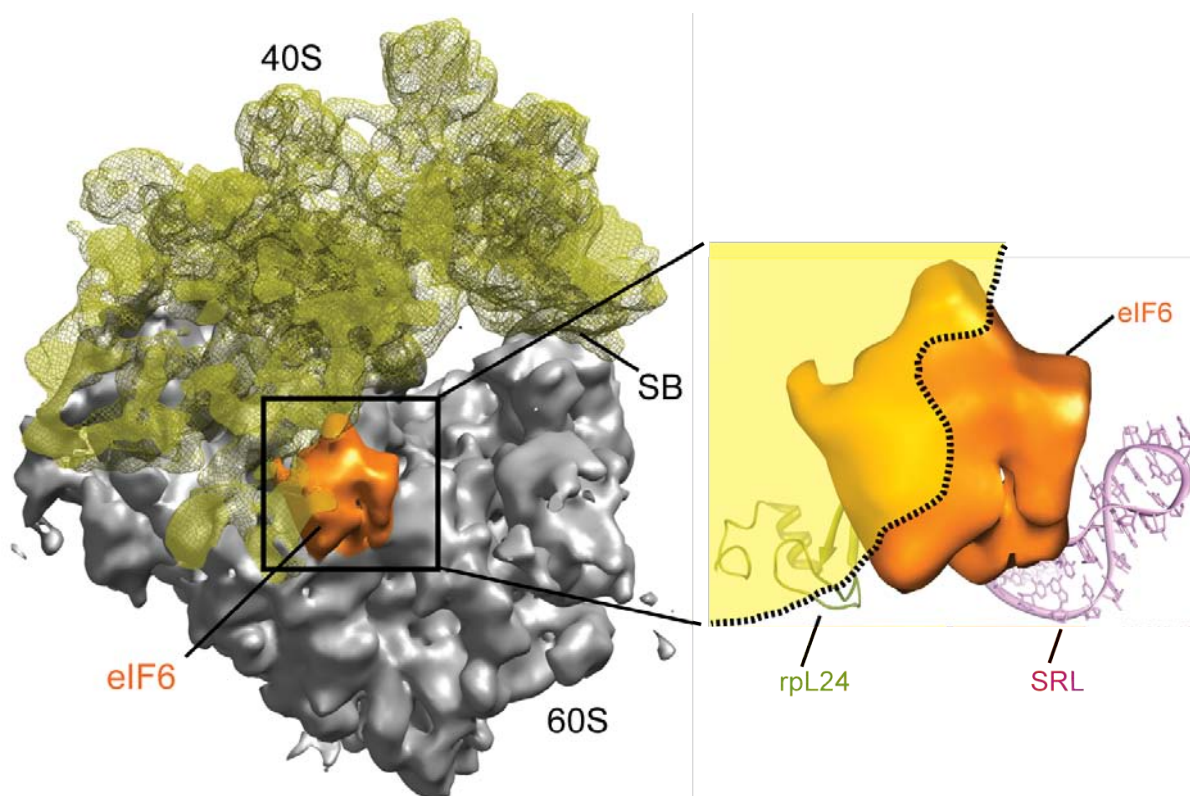


Figure 9.: Binding of eIF6 prevents 40S association. | Cryo-EM map of the 60S-eIF6 complex superimposed with the 40S subunit in the 60S-bound conformation. Close-up view of the interfering region with the 40S, which is indicated as yellow shadow mark. (60S (gray); eIF6 (orange))

eIF6 density would sterically clash with the rRNA of the 40S subunit, explaining the mutually exclusive binding by simple steric hindrance (Fig. 9). The position of eIF6 at the 60S subunit surface coincides exactly with the dynamic intersubunit bridges B6, formed by the C-terminal region of the ribosomal protein rpL23 (Spahn et al., 2001). Therefore, when eIF6 is bound to the 60S subunit the bridge B6 and the nearby located

bridge B5a, both formed by rpL23, are directly affected. In addition, the surrounding

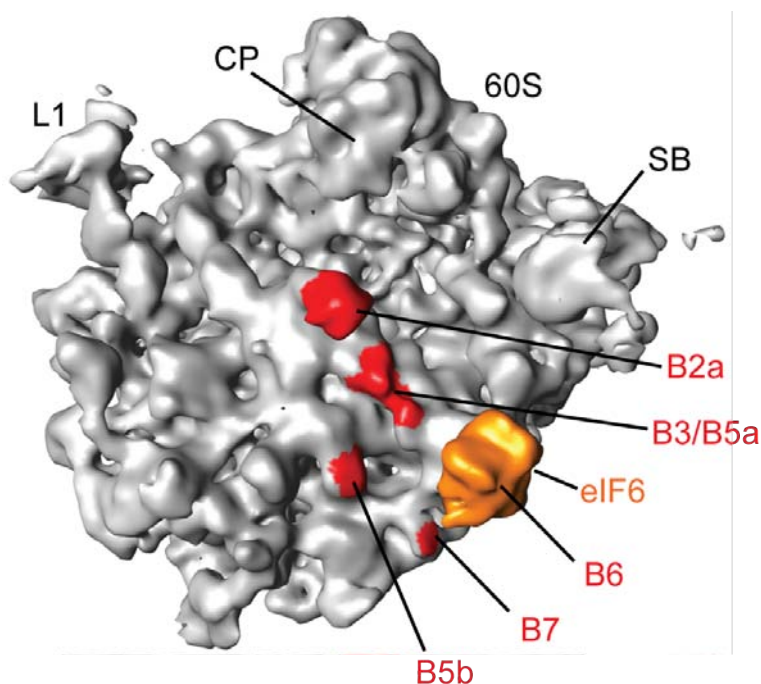


Figure 10.: Intersubunit bridges in the vicinity of eIF6. | The binding position of eIF6 on the 60S coincides directly with bridge B6. (intersubunit bridges in red)

intersubunit contacts B7, B3 and B5b can no longer be formed due to sterical hindrance, resulting in the observed highly efficient prevention of subunit joining (Fig. 10). The conserved phosphorylation sites of yeast eIF6, formed by the two residues Ser174 and Ser175 (Basu et al., 2003), are located at the accessible surface of the bound eIF6, which is not involved in the interaction with the 60S subunit (Fig. 7a and d). Also the C-terminal nuclear localization sequence, which was not visualized in the crystal structure, would be located at the accessible outer surface of eIF6.

5.5. Release of eIF6 by the yeast GTPase Efl1, implications from a model

The elongation-factor like GTPase Efl1 (Efl1p) from yeast, that is crucial for the release of eIF6, is highly homologous to the translation elongation factor eEF2 (Senger et al., 2001). Therefore, it is safe to assume that they share a very similar binding site (Graindorge et al., 2005), which is known for eEF2 (Spahn et al., 2004) to be the canonical factor binding site. Since the interaction for eEF2 with the 80S ribosome is known

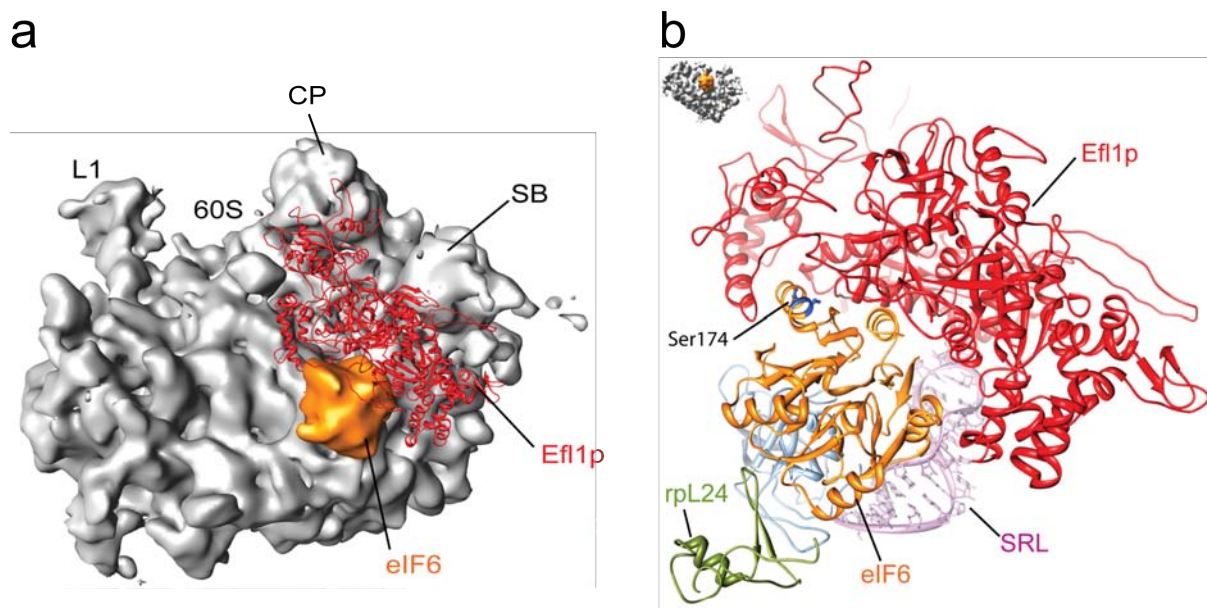


Figure 11.: Release of eIF6 by Efl1 can be explained by a model of 60S-bound Efl1. | (a) Putative binding of modeled eEF2-like GTPase Efl1 on the factor binding site. (b) Homology model of Efl1 in its 60S-bound conformation in the vicinity to eIF6. (Efl1 in red)

from cryo-EM (Spahn et al., 2004), we calculated a comparative model of Efl1 on the basis of eEF2 in its ribosome-bound conformation. The model of Efl1 was generated, using the HHpred server (Söding et al., 2005) for sequence alignment. A comparative model of Efl1 was calculated based on the ribosome-bound eEF2. Parts of the Efl1 sequence which could not be aligned to eEF2, were separately modeled using HHpred. A final model for the 60S subunit-bound Efl1 was calculated using the software package MODELLER (Sali et al., 1995; Eswar et al., 2007) for model calculation, and MDFF (Trabuco et al., 2008) for stereochemical adjustments. Strikingly, in this position Efl1p could bind concomitantly with eIF6 and would perfectly embrace eIF6 to facilitate an interaction with its GTPase domain (Fig. 11a). The release of eIF6 can in this model be explained by direct interaction of Efl1 with eIF6. A small conformational change of Efl1 in this position would be sufficient to trigger GTP-dependent release of eIF6 from the 60S subunit (Fig. 11b).

5.6. Conclusions

Our structure provides the basis for a molecular understanding of eIF6's conserved activity as a ribosomal anti-association factor. Based on our structural data, we propose a model where the anti-association activity of eIF6 with the mature 60S subunit can be explained by direct sterical hindrance of the dynamic intersubunit bridge B6 and the surrounding bridge environment mainly influencing the bridges B5a and B7. Due to the intermediate resolution of the cryo-EM map, the accuracy for docking of the eIF6 structure into the assigned density is limited. Conformational changes, which might occur as a result of the eIF6 interaction with the 60S subunit could not be detected at this resolution level. Therefore, the reconstruction alone does not allow an unambiguous assignment of the eIF6 orientation, in terms of binding side and in-plane rotation. In a previous study, the binding position of archaeal aIF6 with the 50S subunit was shown biochemically (Benelli et al., 2009). Our cryo-EM map shows the same binding side for eIF6 as it was identified for archaeal aIF6. Therefore, the binding site of eIF6 with rpL23 (L14 in archaea) is indeed conserved. In the same study, three RNA residues of helix 69 (H69) located on the 50S intersubunit surface were found as potential binding partner for archaeal aIF6, by RNA protection experiments. This result is not in agreement with our structural data, because the binding position of eIF6 found in our cryo-EM map would not allow for an interaction of eIF6 with these too distant RNA residues.

Outlook

An improved resolution at secondary structure level would allow a docking of eIF6 with higher accuracy (Rossmann et al., 2005). Certainly, the experimental setup has to be changed to overcome the orientation problem that is most likely the main reason for the limited resolution of the 60S-eIF6 reconstruction. Variation of buffer conditions (salt, pH) and glow discharging, or the use of carbon free grids to avoid the influence of the charged carbon support layer, which is often influencing the orientation of particles in some cases (Frank, 2006), are some possible starting points to come to an improved dataset with a more homogeneous distribution of the particle orientations.

The recycling of eIF6 is not conserved amongst eukaryotes. In yeast, the GTPase Efl1 acts in concert with the protein Sdo1 to release eIF6 from the 60S subunit. A cryo-EM structure of a 60S-eIF6-Efl1 complex would be an approach to proof our assumption of the binding position of Efl1 and its mechanism to release eIF6. Also the role of Sdo1 in the release of eIF6 has to be established in future studies to come to a better

understanding of the functions of Efl1 and Sdo1 in the release process. It is known that eIF6 participates in several pathways, for instance in the recruiting of the RISC complex and in ribosome biogenesis (Miluzio et al., 2009). Therefore, an interesting target would be the structural analysis of a 60S eIF6-RISC (TRBP, Dicer, Ago2) complex, which was characterized in a previous biochemical study (Chendrimada et al., 2007). It remains to be seen to what extent eIF6's ribosomal binding mode is also functionally involved in its additional activities in higher eukaryotes. Additional studies are needed to uncover the relationship between the other various functional activities of eIF6 *in vivo* (Miluzio et al., 2009) and its essential anti-association activity.

6. Folding inside the ribosomal tunnel

6.1. Specific aim

We addressed the question if α -helix formation within the ribosomal tunnel is feasible and if so, where it can occur? In principle would the dimension of the tunnel allow accommodation of secondary structure elements like α -helices, which can be estimated from ribosomal X-ray structures (Voss et al., 2006) (see also Fig. 2 in the Introduction). A number of different biochemical studies, including FRET measurements (Woolhead et al., 2004) and pegylation experiments (Lu & Deutsch, 2005b), point towards the same direction and gave indirect indications that secondary structure formation can already occur inside the ribosomal tunnel. However, the question if secondary structure can form so early in the shielded and non-cytosolic environment of the ribosomal tunnel is still debated and a solid structural evidence for this problem is missing. We used cryo-EM and single particle reconstruction to tackle this problem in eukaryotic ribosomes. At the moment there is no structural access to visualize nascent chains inside the ribosomal tunnel via crystallography, because 70S ribosome nascent chain complexes (RNCs) could not be crystallized so far. Furthermore, no X-ray structure of a eukaryotic 80S ribosome nor of a 60S subunit have been solved. This means that cryo-EM is currently the only tool that can provide direct structural insights into eukaryotic ribosomal complexes, like 80S RNCs, with adequate resolution. In addition, our group succeeded already to visualize different nascent polypeptide chains of stalling and non-stalling sequences inside the ribosomal tunnel with cryo-EM (Seidelt et al., 2009; Becker et al., 2009).

6.2. Sample preparation

A wheat germ *in vitro* translation system was utilized to prepare stalled 80S RNCs with dipeptidyl-aminopeptidase B (DPAP-B) nascent chain in the tunnel (Halic et al., 2004). DNA templates were truncated and the stop codon was removed, to trap the translating ribosomes at the last codon. The stalled ribosomal complexes were purified (Shashi Bhushan) via His affinity purification as described previously (Beckmann et al., 1997) (for details see 8.2.5 in Materials and Methods).

6.3. Cryo-EM analysis

For this study, two structures of ribosomal complexes bearing nascent chains (RNCs) with different regions of high α -helical propensity were determined. The datasets were

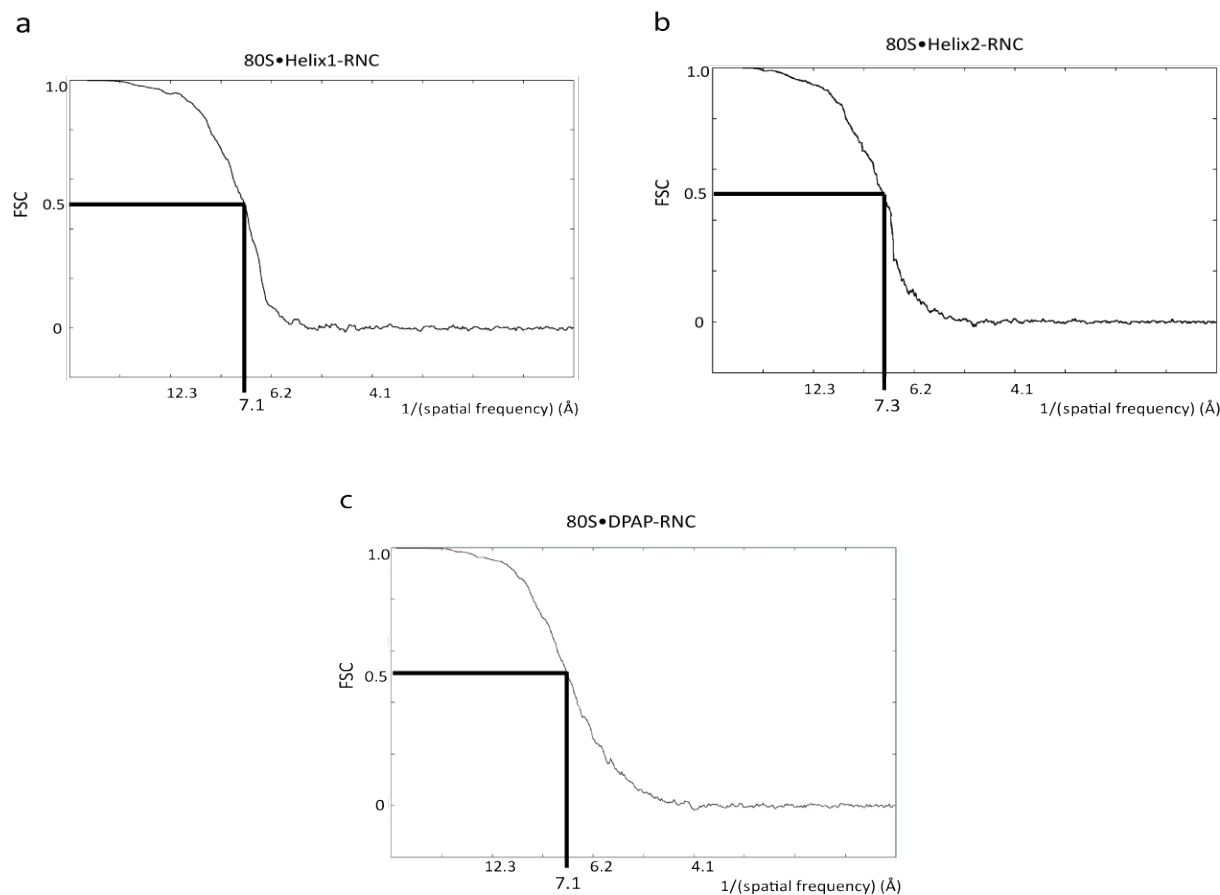


Figure 12.: Resolution curves of the cryo-EM reconstructions (a-c). | Respective resolution is marked at 0.5 FSC cutoff.

recorded under low-dose conditions on a Tecnai F30 field emission gun electron micro-

scope and scanned on a Heidelberg drum scanner, resulting in a pixel size of 1.24 Å on object scale. Datasets were further processed with the SPIDER software package (Frank et al., 1996). After automated particle picking with SIGANTURE (Chen & Grigorieff, 2007) followed by visual inspection 200,000 particles for 80S Helix1-RNC, 230,000 particles for 80S Helix2-RNC and 250,000 for 80S DPAP-RNC were selected. We sorted the data into programmed (with P-site tRNA) and un-programmed/empty ribosome (without P-site tRNA) sub-datasets using existing reference reconstructions of programmed and un-programmed wheat germ 80S ribosomes. Final CTF-corrected reconstructions had a resolution of 7.1 Å and 7.3 Å for the Helix1 and Helix2 datasets, respectively, and 7.1 Å for the control DPAP dataset, based on the 0.5 FSC cutoff value (Fig. 12a-c).

6.4. Secondary structure marker in the tunnel

In this study, modified DPAP-B constructs were generated and parts of the sequence were replaced with a short peptide that has a strong propensity to form a monomeric α -helix in solution (Marqusee & Baldwin, 1987; Arai et al., 2001) (Fig. 13b). The peptide contains five EAAAK repeats and forms a standard $[i + 4 \rightarrow i]$ α -helix, in which every backbone N-H group donates a hydrogen bond to the backbone C=O group of the amino acid four residues earlier (Fig. 13b). Each repeat of this helix is stabilized by a Glu⁻-Lys⁺ salt bridge, leading to >80 % helicity in aqueous solvent as determined by circular dichroism (CD) studies (Marqusee & Baldwin, 1987; Arai et al., 2001). When translation reaches the 3' end of the truncated mRNA, 115 amino acids have been translated and Asp-tRNA is located at the P site of the ribosome. The position of the helix sequence was varied to answer the question where in the tunnel α -helix formation is allowed. In the Helix1 construct, the helix forming sequence is positioned at amino acids 72-96, whereas in Helix2, it is located at amino acids 83-108, i.e. -19 and -7 from the Asp of the P-tRNA, respectively (Fig. 13a). Since the ribosomal tunnel is known to protect 30-40 amino acids (Hardesty & Kramer, 2001), both helix forming sequences should still be enclosed within the exit tunnel. Since the EAAAK repeats have been structurally characterized in the antifreeze proteins of cold-water fish, such as the winter flounder, it was possible to build a homology model for the helical part of the nascent chain based on the known crystal structure of the antifreeze protein HPLC6 isoform (Sicheri & Yang, 1995) (Fig. 13b and Fig. 15e).

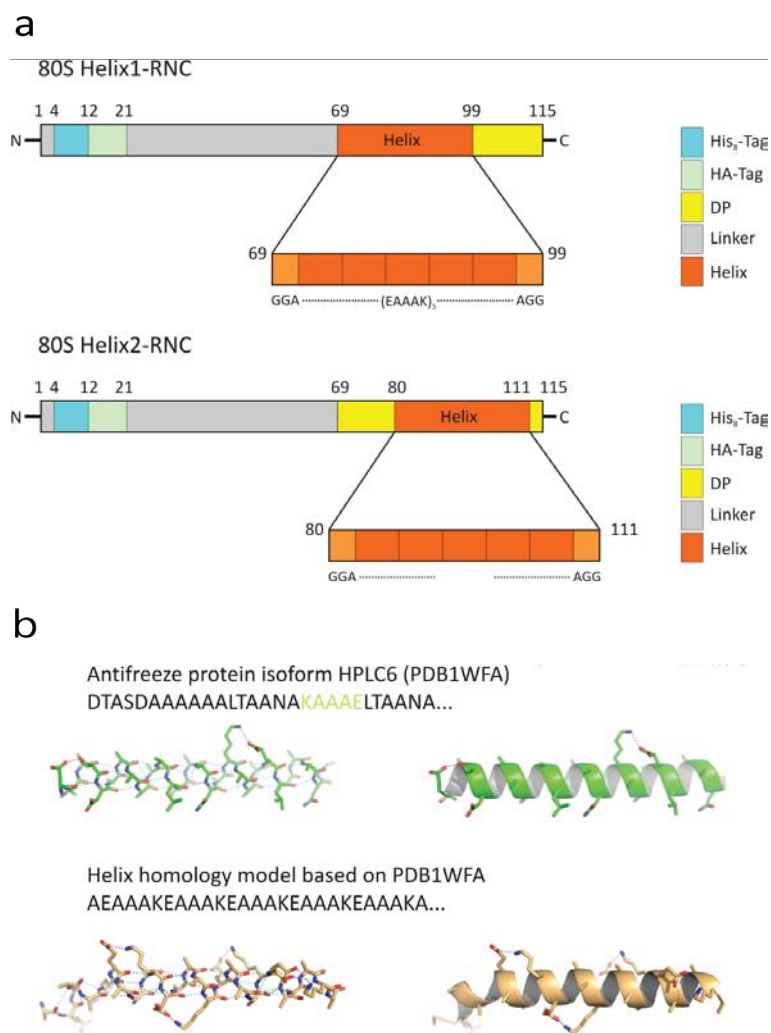


Figure 13.: Design of the helix constructs. | (a) An α -helix segment was inserted at two different positions into the DPAP-B sequence. (b) Crystal structure of the HPLC6 antifreeze protein was taken as basis for the homology model of the $(EAAAK)_5$ helix (salt-bridges indicated with dashed lines).

6.5. α -helical nascent chains can fold in distinct tunnel region

In all reconstructions, strong density for a single peptidyl-tRNA within the intersubunit space is observed (Fig. 14a, c, e). Most striking, however, is the presence of additional density within the exit tunnel of the 80S Helix-RNCs that can be attributed to the nascent chain (Fig. 14a-d), whereas in comparison the tunnel of the control 80S DPAP-

RNC contains little additional density for the corresponding DPAP-B nascent chain (Fig. 14e, f). In the tunnel of the 80S Helix-RNCs, the strongest region of density is observed

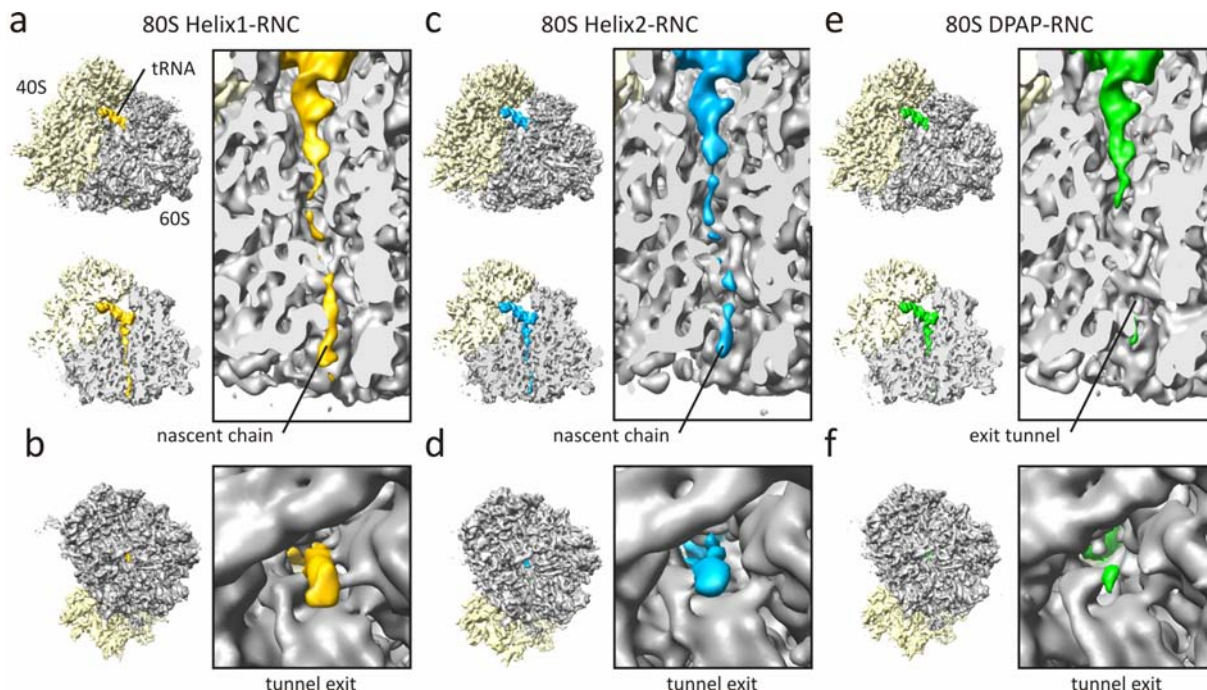


Figure 14.: Cryo-EM reconstructions of three 80S RNCs. | Maps of the 80S Helix1-RNC (a,b), 80S Helix2-RNC (c,d), and the control 80S DPAP-RNC (e,f). Each top left inset show the respective overall orientation, cross-section and tunnel view below. Right-hand panels show the cross-section and tunnel view.

for the N-terminal region of the nascent chain near the tunnel exit (Fig. 14a-d).

The densities for the P-tRNA and associated nascent chains of the reconstructions of the 80S Helix-RNCs and 80S DPAP-RNC were isolated (Fig. 15a-c). A molecular model for the P-tRNA was fit to the isolated density of the 80S Helix1-RNC (Fig. 15d) to locate the terminal CCA-end of the tRNA, which thus identifies the C-terminus of the nascent chain. All three reconstructions have some density corresponding to the nascent chain directly adjacent to the peptidyl transferase center (PTC) (Fig. 15). In the 80S Helix1-RNC, the strong density for the N-terminal region of the nascent chain is consistent with an α -helical conformation in this region and coincides perfectly with the expected location in the tunnel (Fig. 15d, e). The density can account for four of the five EAAAK repeats, correlating to 20 amino acids, or six turns of the α -helix (3.3 amino acids per turn) (Fig. 15e). At lower thresholds, additional density extends into the solvent from the N-terminal part of the helix, most likely indicating flexibility in this region. We do not think the α -helix unwinds upon exiting the tunnel, as suggested by

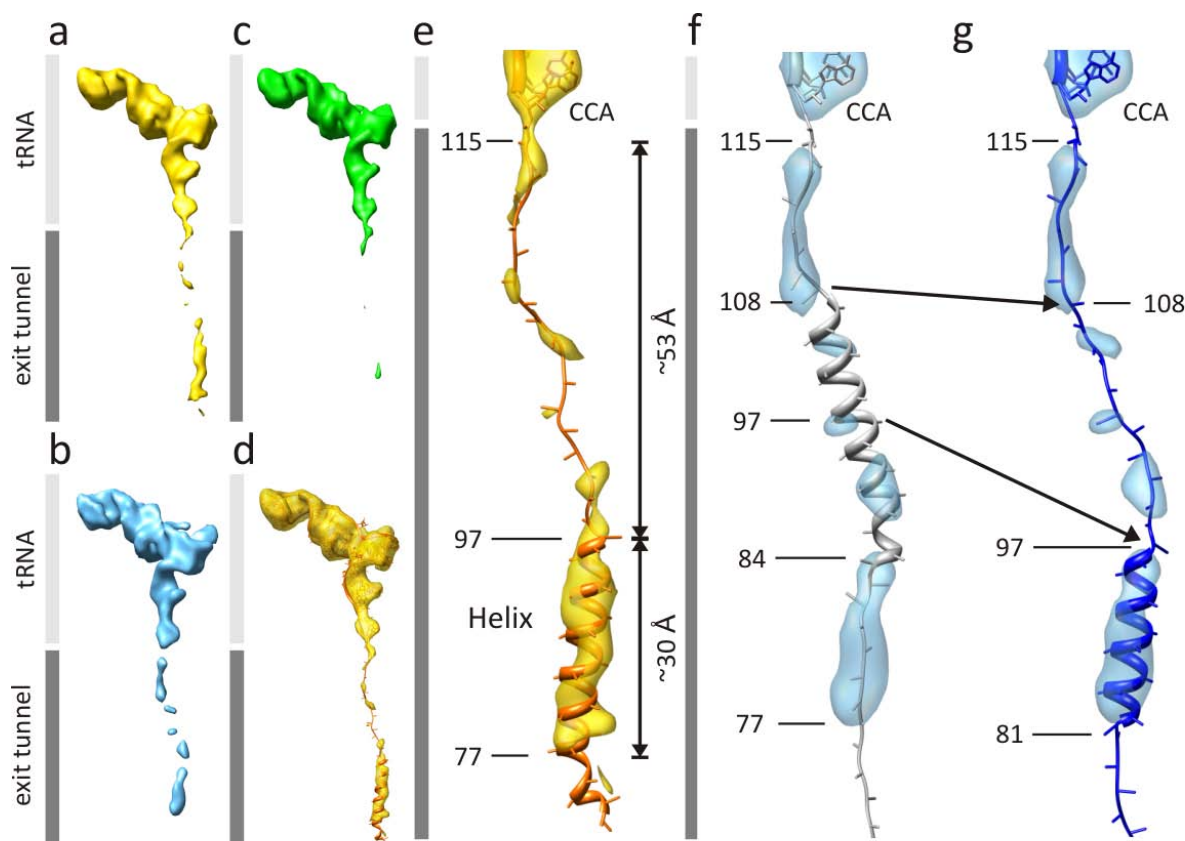


Figure 15.: Comparison of the tRNA-nascent chains. | Isolated density for the P-site tRNA and nascent chain from the (a) 80S Helix1-RNC (gold), (b) 80S Helix2-RNC (blue) and (c) 80S DPAP-RNC (green). (d) transparent density of (a) with fitted ribbon model for tRNA and nascent chain. (e) Zoom of (d) with amino acid numbering. (f,g) Zoom of (b) with alternative models for the Helix2 nascent chain. (CCA - terminal CCA-end)

FRET studies with a transmembrane helix (Woolhead et al., 2004), since the EAAAK repeats and antifreeze peptides have been shown by CD and NMR to be stable in solution (Marqusee & Baldwin, 1987; Arai et al., 2001; Liepinsh et al., 2002). With this fitting, the proximal portion of the helix (Gly97) is located ~ 53 Å from the Asp115 amino acid at the P site, and it is thus only possible to span this distance using an extended conformation (3.0 - 3.4 Å/aa) for the 18 interceding amino acids of the nascent chain (Fig. 15e). The properties of the observed density for these regions are also consistent with an extended conformation for these amino acids, whereas the fragmentation suggests that the nascent chain does not adopt a distinct conformation in some sections of the tunnel.

Similar to the 80S Helix1-RNC the strongest density for the nascent chain in the 80S Helix2-RNC is observed in the lower region of the exit tunnel (Fig. 15f). However, if

all five repeats of the EAAAK sequence had adopted a helical conformation, we would have expected strong density to also be present in the middle of the tunnel. Therefore, it is likely that the proximal portion of the region with helical propensity (residues 97-108) is unable to adopt an α -helical conformation, but instead acquires an extended conformation. In this case a model of the distal portion of the remaining helical stretch (residues 77-97) fits nicely into the strongest region of nascent chain density as an α -helix (Fig. 15g).

6.6. Contacts of the nascent chain with the ribosomal tunnel

In order to dissect the contacts between the nascent chain and ribosomal components of the exit tunnel, a molecular model of the wheat germ ribosomal tunnel (Fig. 16a,b) was generated and then fit to both the 80S Helix-RNC maps (Fig. 17). In the upper region

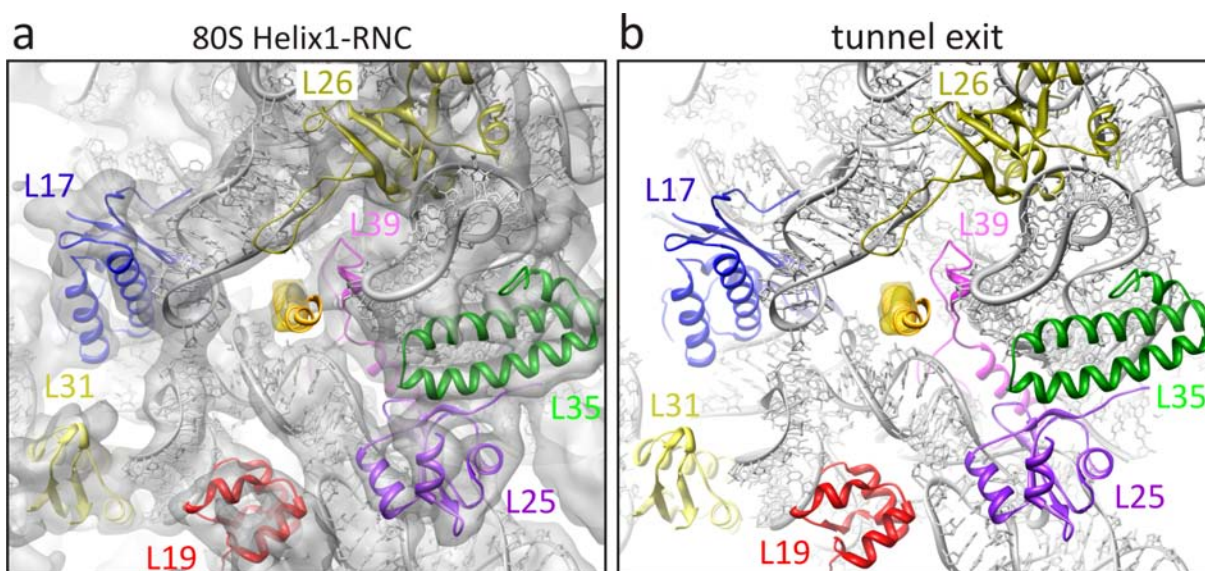


Figure 16.: Model of the exit tunnel fitted in 80S Helix1-RNC map. | (a) Exit tunnel view with cryo-EM density (gray) and rRNA- and protein models. (b) as in (a), but without map density.

of the tunnel of the 80S Helix1-RNC, three strong connections are observed between the nascent chain and the tunnel wall (Fig. 17a). Adjacent to the PTC, the nascent chain appears to form a contact in the vicinity of 28S rRNA nucleotide A2062 (*E. coli* numbering used throughout). This contact does not appear to be present in the 80S

Helix2-RNC (Fig. 17e). From the available ribosome crystal structures, A2062 is known to be flexible, adopting a position flat against the tunnel wall as in the *H. marismortui* apo-50S structure (Ban et al., 2000), or protruding into the tunnel lumen when P-site tRNA mimics are bound (Schmeing et al., 2005). Clearly, the latter position fits better to the density of the 80S Helix1-RNC map, suggesting the nascent chain stabilizes a distinct conformation of A2062 (Fig. 17a). In *E. coli*, mutations at A2062 relieve the translational arrest resulting from ErmC stalling (Vazquez-Laslop et al., 2008). Deeper in the tunnel, the nascent chain establishes contact with A751 in both 80S Helix-RNC maps (Fig. 17a, e). Insertions at A751 have been reported to eliminate tryptophan-induction associated with TnaC-mediated translational stalling (Cruz-Vera et al., 2005). The extensions of ribosomal protein rpL4 form two contacts with the 80S Helix1-RNC nascent chain, one near the constriction (Fig. 17a) and a second to the proximal end of the helix (Fig. 17b), whereas in 80S Helix2-RNC the proximal contact is absent (Fig. 17f) and the rpL4 contact at the constriction is significantly weaker (Fig. 17e). Between these two points, negligible density for either nascent chain is observable, indicating that it does not adopt a single distinct conformation (Fig. 17a, e and g). Despite this, additional density is observed contacting the tip of the β -hairpin of rpL17 (Fig. 17a). In *E. coli*, mutations within this region of L22 (the homologue to rpL17) can relieve TnaC- and SecM-mediated stalling (Nakatogawa & Ito, 2002; Cruz-Vera et al., 2005). The fact that the contacts observed here for non-stalling sequences are similar in location to those predicted for some of the known stalling leader peptides, hints that these regions of the tunnel represent functional hotspots for tunnel-nascent chain interaction. In both 80S Helix-RNC maps, the density for the α -helix is sandwiched between ribosomal protein rpL39 and the loop region of helix 50 (H50) of the 28S rRNA (Fig. 17b, d and f, h). rpL39 appears to make two strong contacts with the helix, one proximal and the other more distal (N-terminal), whereas the H50 contact is different between the two structures (Fig. 17b, f).

6.7. Conclusions

Photo-crosslinking studies have identified sequential contacts of a compacted transmembrane containing nascent chain, first to rpL4, then rpL17 and finally to rpL39 (Woolhead et al., 2004) – ribosomal proteins that are visualized to contact the nascent chain in both the 80S Helix-RNCs (Fig. 18). In these studies it was concluded that the transmembrane helix maintains a helical conformation during its passage throughout the entire

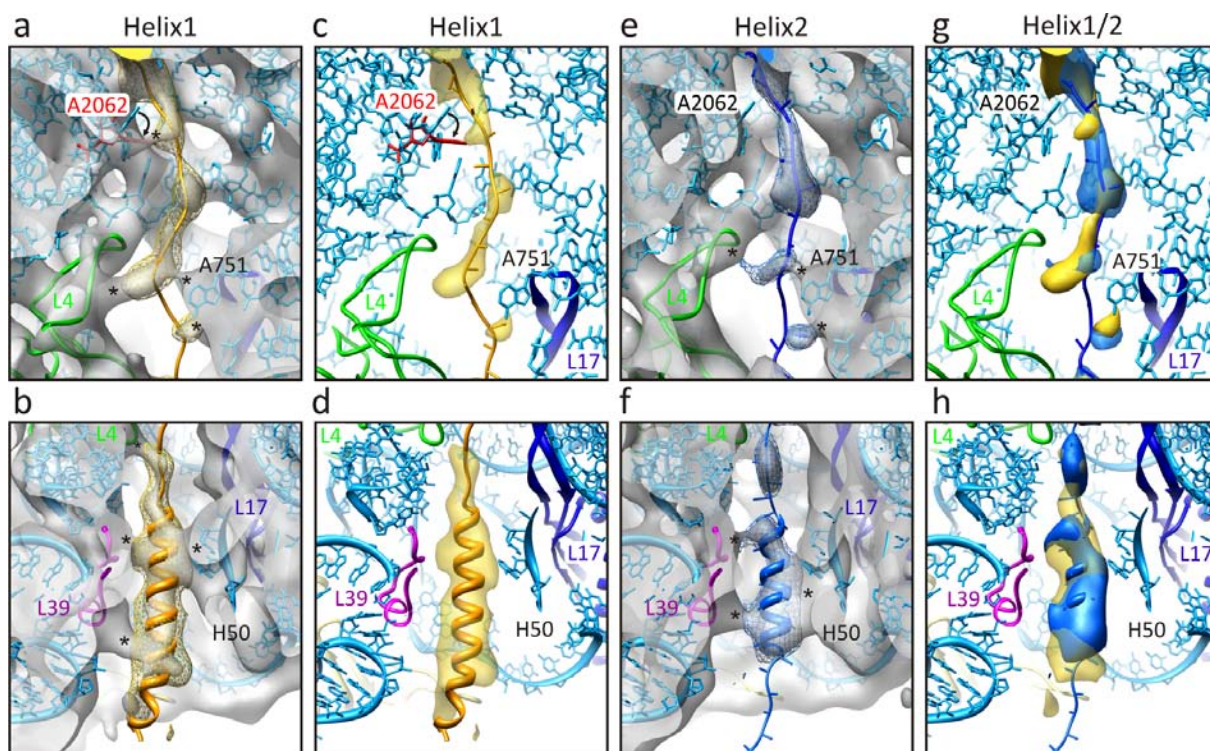


Figure 17.: Helix-nascent chain interactions. | Cross-section of the upper (top panels) and lower (bottom panels) tunnel regions of the (a-d) 80S Helix1-RNC (gold), (e,f) 80S Helix2-RNC (blue) and (g,h) comparison of both. (cryo-EM maps (gray); isolated density for the nascent chain shown at a lower threshold (gold and blue mesh); A2062 (*E. coli* numbering) is shown in two conformations (a,c), PDB 1S722 (blue) and PDB 1VQN23 (red); contacts between nascent chain and ribosomal tunnel components indicated with asterisks (*))

ribosomal tunnel. Although we observe no helix formation in the middle of the tunnel, i.e. directly following the constriction (Fig. 18). The observed discrepancy can be related to the use of a hydrophobic transmembrane helix (Woolhead et al., 2004), rather than the hydrophilic helix used here. In any case, the ability to form a helix near to the tunnel exit site, but not in the middle region of the tunnel, is consistent with the zones of secondary structure formation identified by Lu and Deutsch (Lu & Deutsch, 2005b).

Given that α -helix formation within the exit tunnel is indeed possible in distinct regions, this raises the question as to what the functional significance of this finding is? First, it is tempting to speculate that allowing, or even promoting (Lu & Deutsch, 2005b), α -helix formation when β -sheet formation is not yet possible has an impact on protein folding. This would imply that folding might occur using a hierarchy of secondary structure elements, with α -helix formation occurring first wherever possible. Such a

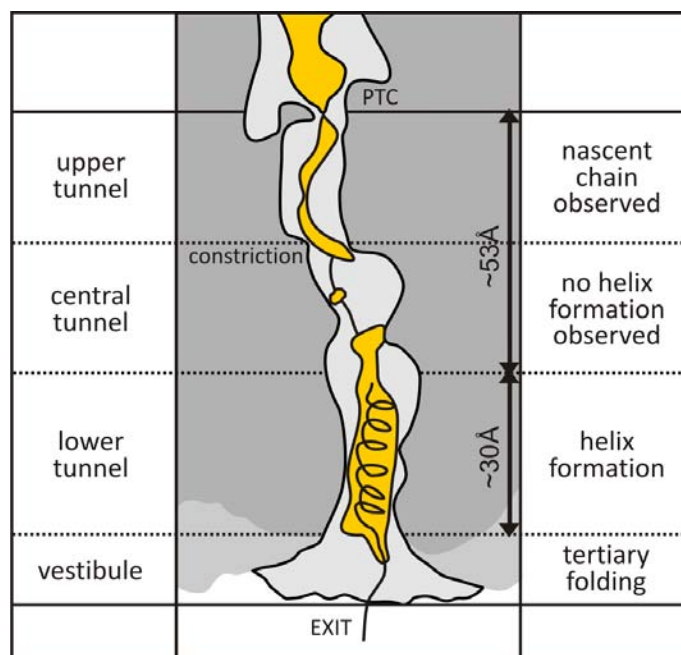


Figure 18.: Helix and tertiary structure formation is only observed in the lower tunnel region. | Schematic representation of a cross-section of the 80S Helix1-RNC complex.

scenario would considerably reduce the complexity of the theoretical conformational space that is necessary to be sampled before the correct fold is adopted. Additionally, it would also change the appearance of nascent peptides as substrates for co-translationally acting chaperones, e.g. bacterial TF or Hsp70s in eukaryotes (Fig. 19b). Indeed, tertiary structure formation, such as α - and β -hairpins, has already been observed to occur near the tunnel exit (>80 Å from tunnel start) where the tunnel widens significantly to form a vestibule (Kosolapov & Deutsch, 2009) (Fig. 18). Second, α -helix formation in the tunnel may be important for proteins containing alpha-helical domains destined for membrane insertion. Co-translational targeting by SRP, for example, may be promoted since α -helicity of the signal sequence is important for its recognition by SRP (Adams et al., 2002) (Fig. 19b). Indeed, compaction of transmembrane domains in the ribosomal tunnel has been reported (Woolhead et al., 2004) and, a compacted conformation for the signal anchor sequence has been observed by cryo-EM to bind in the vestibule at the end of the ribosomal tunnel on *Escherichia coli* ribosomes (Halic et al., 2006a). Third, restricting α -helix formation to only certain regions of the tunnel may reduce the modes of interaction of the nascent peptide with the tunnel wall. Compared to an extended chain, a nascent chain forming an α -helix throughout the entire tunnel could

potentially establish twice as many interactions. This might result in unfavorably stable interactions. On the other hand, helix formation in permitting regions may help to scan for distinct interaction patterns facilitating regulatory events. While these hypotheses

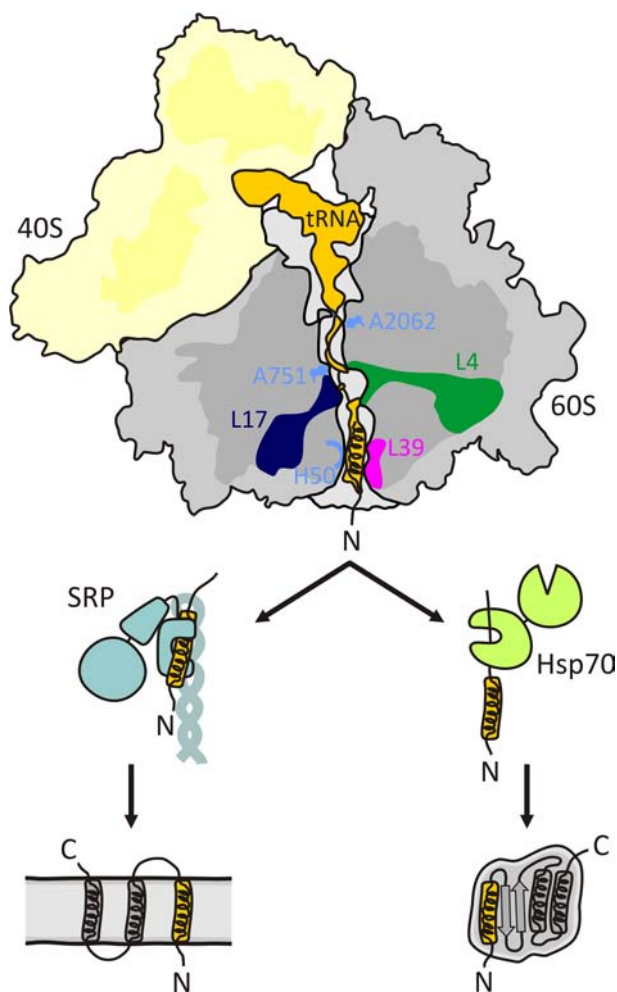


Figure 19.: Implications of helix formation within the ribosomal exit tunnel. | Schematic representation of a cross-section of the 80S Helix1-RNC complex. The helix of the nascent chain forms interactions with helix 50 (H50, blue) of the 28S rRNA and rpL39 (magenta). Helix formation in the ribosomal tunnel may assist in membrane insertion, as shown for signal recognition particle (SRP) dependent pathway, and/or promote correct or more efficient folding of cytoplasmic proteins, with or without aid of chaperones, such as Hsp70s.

need to be examined, the universal conservation of the dimensions of the ribosomal tunnel is consistent with its significance in providing nascent proteins with a very defined first environment.

Outlook

In this study we observed α -helix formation in a defined region of the ribosomal tunnel, of a hydrophilic segment with high helical propensity. Prospective work can now focus on the question to what extent natural transmembrane helices can fold in the tunnel. Of particular interest would be well characterized constructs like the transmembrane α -helices, which were studied by Hessa *et al.* in the context of co-translational protein translocation (Hessa *et al.*, 2005, 2007). The interpretation of the maps is at the current resolution limit of cryo-EM maps, because it is based on a differentiation between the extended part and the α -helical part of the nascent chain. To resolve the complete nascent chain by cryo-EM is already impressive, but the interpretation stays and falls with the appearance of the resolved density for the nascent chain, which is not only determined by the quality of the data (S/N ratio and power spectra). An even bigger influencing parameter are the contacts of the nascent chain with the tunnel wall, resulting in stable or flexible regions for the nascent chain, whereby the latter ones show a loss of density information (see also in 3.2 Introduction). Thus, it is nearly impossible to distinguish if an absent or fragmented density in a particular region is the result of flexibility, or of the inability of the nascent chain to form secondary structure. Interesting and helpful would be in this case, to validate the findings based on cryo-EM data with proven biochemical methods, such as crosslinks, FRET experiments, or pegylation assays, used in Deutsch's studies (Lu *et al.*, 2007; Lu & Deutsch, 2005b,a). In the long run, crystallization of 70S RNCs would open the possibility to directly address these questions at an atomic resolution level. To observe as a next step potential β -sheet formation in the ribosomal tunnel, cryo-EM has to touch atomic resolutions below 4 Å.

7. Folding beyond the ribosomal tunnel

7.1. Specific aim

Most of the current knowledge about chaperone-assisted folding of nascent polypeptide chains at the ribosome comes from the well studied bacterial trigger factor (TF). There are less and exclusively biochemical data of co-translationally acting chaperones in the complex eukaryotic system available. The aim of this study was to get structural insights into the ribosome-associated chaperone system and the arrangement of the co-translational folding machinery at the eukaryotic ribosomal exit tunnel. For this reason, different structural methods were combined. Small angle X-ray scattering (SAXS) was used to get a first low resolution model of RAC in solution. Then cryo-EM in combination with single-particle reconstruction was used to analyze the interaction of RAC with the eukaryotic 80S ribosome.

7.2. Purification of RAC

First, high yields of RAC were purified. In collaboration with the group of Sabine Rospert in Freiburg a large-scale purification protocol was established. RAC is a het-

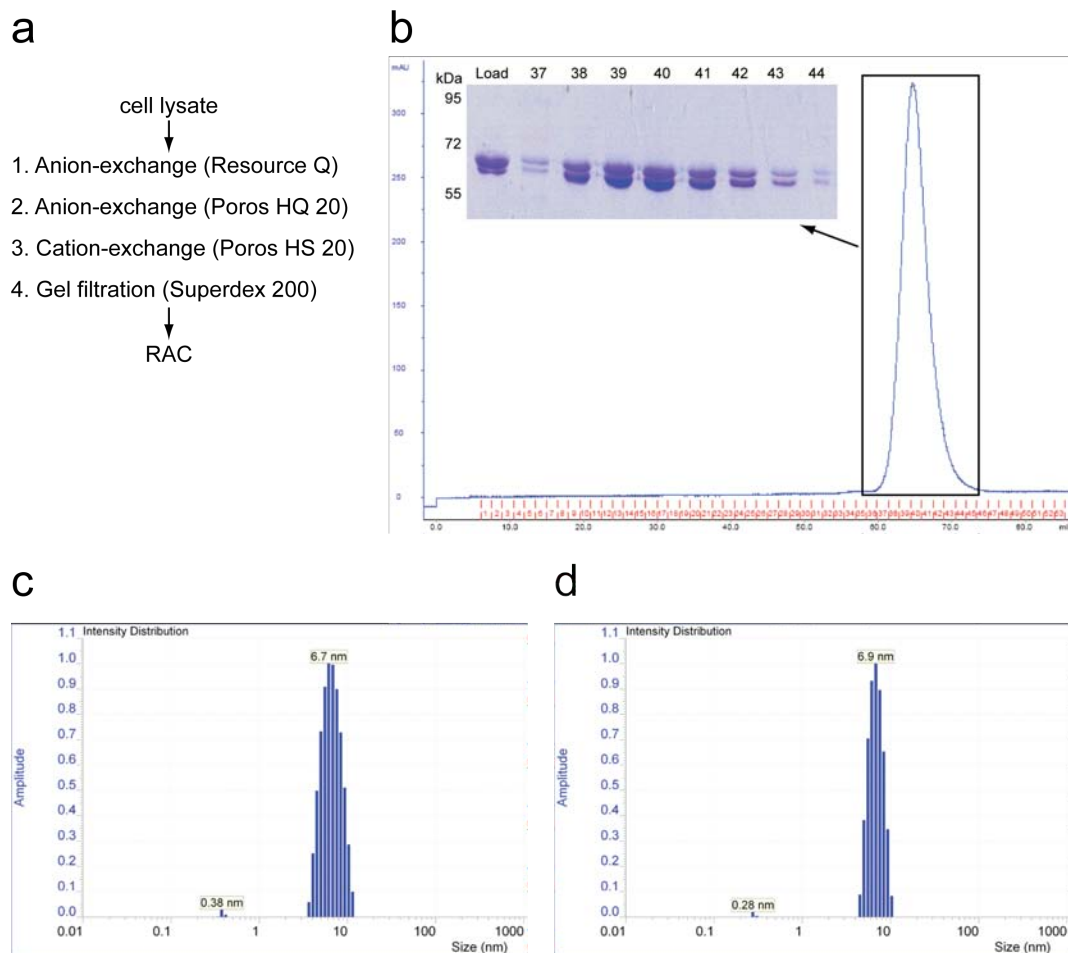


Figure 20.: RAC purification and dynamic light scattering (DLS). | (a) Four step purification protocol of the RAC purification, starting with an anion-exchange column Resource Q, followed by a second anion-exchange column (HQ 20) and a cation-exchange column (HS 20). (b) The final gel filtration run (Superdex 200), leading to a purified RAC sample. (c) DLS spectra of RAC with a concentration of 3.4 mg/ml in 100 mM and (d) 200 mM NaCl. The calculated hydrodynamic radius is indicated in nm. (adapted from Steffen Fliehm)

erologous complex that consists of the two stably interacting proteins, the Hsp70 Ssz and the J-protein Zuo. Both subunits of the complex differ in their isoelectric point (pI), which results in a negative and positive net charge for Ssz (pI = 4.8) and Zuo (pI = 8,8) at neutral pH, respectively. The RAC complex was purified using a combination of

ion-exchange columns in four chromatography steps (Fig. 20a). First a pre-cleaning step by an anion-exchange column (Resource Q) was conducted. A second anion-exchange column (POROS HQ 20) was followed by a cation-exchange column (POROS HS 20), leading to a homogeneous peak with almost pure fractions with little amount of impurities. The pooled fractions were concentrated and loaded onto a gel filtration column (Superdex 200) for final purification, resulting in a highly purified sample (Fig. 20b) without impurities. The purification protocol of RAC had to be adapted to purify the deletion mutant RAC Δ Zuo110 (complex of the first 110 aa of Zuo and Ssz; data not shown). A three step protocol was used to purify RAC Δ Zuo110 using the N-terminal His₆ tag of the truncated subunit Zuo1-110. For the first step, an anion-exchange column (Resource Q) was used followed by a His Trap HP column (Ni-NTA). As in the RAC protocol, gel filtration chromatography (Superdex 200) was used for the final purification step. The two complexes, RAC and RAC Δ Zuo110, could be purified to a high degree on a large scale. An average purification resulted in 0.8 - 1 mg of purified RAC complex per 10 g of *E. coli* cells.

7.2.1. DLS measurements and SAXS model

Based on the purification of RAC and RAC Δ Zuo110, DLS (dynamic light scattering) measurements were utilized to analyze the dispersity of the samples. A prerequisite for SAXS measurements is a pure and monodisperse sample with non-interacting particles of the same size. For optimal use in SAXS measurements monodisperse properties should be maintained within a concentration range of 1 to 5 mg/ml. From the measured DLS curves the hydrodynamic radius of the scattering particles in the sample and the RSD value, as a measure for the peak distribution, was calculated. An increase of the hydrodynamic radius of around 1 nm with increasing concentrations of RAC (1 and 3 mg/ml) was observed, indicating that the molecules of the sample tend to form higher order aggregates (data not shown). The salt concentration was increased to reduce potential intermolecular interactions between RAC molecules in the sample, to lower the formation of aggregates. The best result could be achieved when the NaCl concentration was increased from 100 mM to 200 mM, resulting in a more defined peak with constant hydrodynamic radius, coupled with a shift towards a smaller RSD value (30 % to 18 %) (Fig. 20c, d), indicating that less aggregates were formed and more monodisperse particles of RAC were present. The same effect in the DLS measurements was observed for RAC Δ Zuo110, thus the SAXS measurements were utilized in 200 mM NaCl.

SAXS is a structural method that can provide low resolution information about the

shape of a complex in solution. The SAXS measurements were accomplished at the DESY in Hamburg using a concentration of 2.2 mg/ml and 3.4 mg/ml for RAC and the RAC Δ Zuo110 mutant, respectively. The calculated model reveals an elongated complex

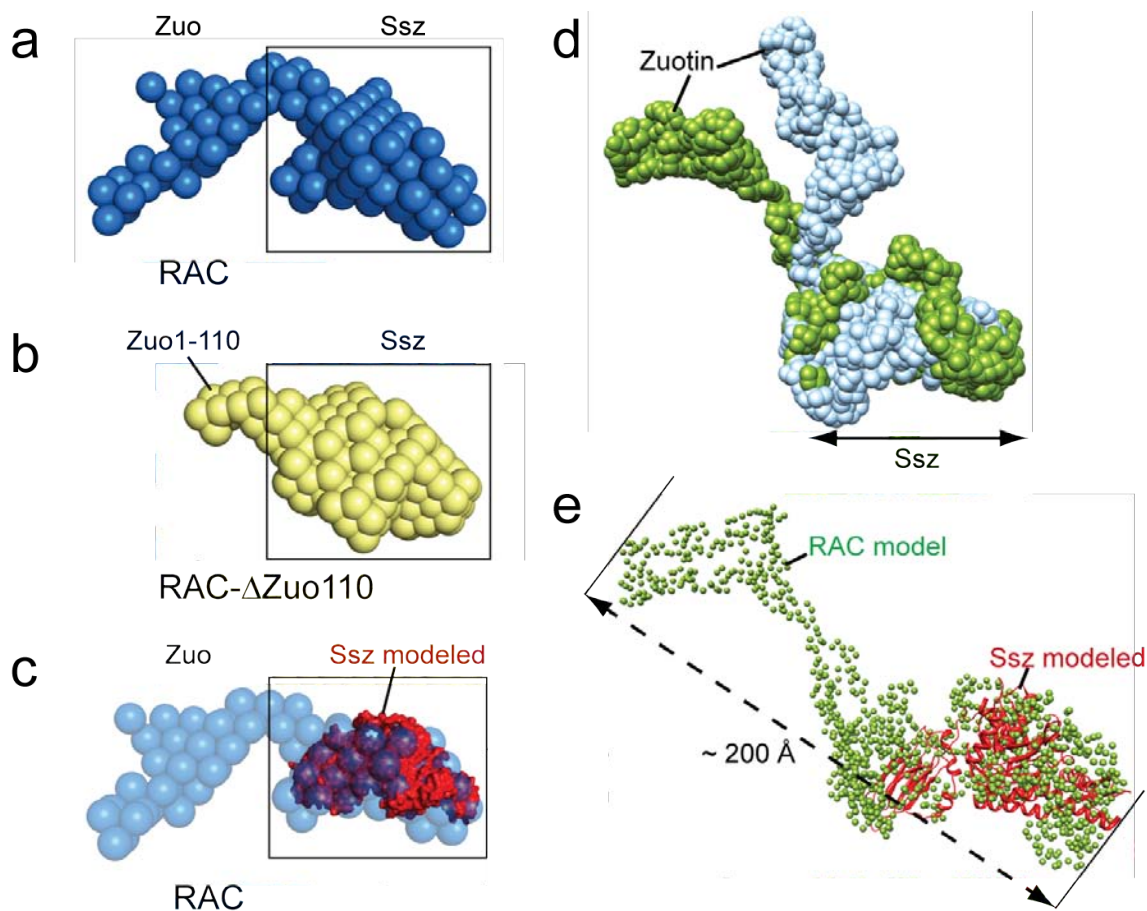


Figure 21.: SAXS model of RAC. | Initial models of (a) wild-type RAC and (b) RAC Δ Zuo110. (c) Ssz homology model fitted into the RAC model of (a). The gray box indicates the assigned position of Ssz. (d) Two refined RAC models were superimposed in their Ssz part, showing large conformational differences in the assigned Zuotin part. (e) RAC has an overall length of around 200 Å (fitted Ssz homology model in red). (adapted from Christoph Leidig)

for RAC, whereby the main length is provided by the Zuotin part (Fig. 21a). By comparison of the two models of wild-type RAC (Fig. 21a) and RAC Δ Zuo110 (Fig. 21b), the Zuotin part of RAC could be assigned in the SAXS model of RAC (Fig. 21c). A homology model of Ssz based on the X-ray structure of bovine Hsc70 (PDB 1YUW) was fitted into the assigned Ssz part of the RAC SAXS model, which also validates the assignment of the Ssz and the Zuotin part (Fig. 21c). The fact that the experimental scattering curve can be interpreted by several models, results in a Zuotin

part of RAC that shows flexibility and which can adopt different conformations (Fig. 21d). In contrast, the Ssz part appears to have a lower degree of flexibility (Fig. 21d). Due to the limited resolution of the SAXS structures the location of some interesting elements, like the charged region as a putative ribosomal binding site and the J-domain, can not be predicted. The low resolution SAXS model of RAC provided a first structural information of the complex in solution. However, to investigate the ribosome interaction of RAC, cryo-EM analysis of reconstituted 80S RAC complexes was realized.

7.3. Reconstitution experiments

A prerequisite for structural analysis with cryo-EM is a defined and homogeneous sample. Therefore, the complex of interest has to be reconstituted *in vitro*. Binding assays were utilized to find optimal conditions to reconstitute the 80S RAC and the 80S RAC-Ssb1 RNC complex. Using this assay the binding of ribosome-associated factors was characterized indirectly by co-pelleting the factor with ribosomes through a sucrose cushion. The binding was studied under low and high salt conditions, meaning in this case 100 mM and 500 mM KOAc, respectively. Yeast 80S ribosomes were isolated from a Δ RAC Δ NAC Δ Ssb knock out strain Δ zuo1 Δ ssz1 Δ edg1 Δ edg2 Δ ssb1 Δ ssb2 (80S $\Delta\Delta\Delta$, IDA123456A - Rospert group) as described in Materials and Methods. A self-made *in vitro* translation system (Walter et al., 1981) was utilized to purify yeast 80S RNCs via His tag purification (for details see 8.2.5 in Materials and Methods). RNC complexes with nascent chains based on the sequence of Dipeptidyl aminopeptidase from yeast (DPAP) were purified as previously described (Beckmann et al., 1997). Truncated mRNA without a stop codon was used to stall the translation reaction at the last codon, leading to artificially stalled 80S RNCs with P-site tRNA bound to the nascent polypeptide chain. Wheat germ RNCs were purified by using a commercial or a self-made *in vitro* translation system. Mammalian RAC and Ssb1 were used as purified components (Rospert group) for the reconstitution experiments. RAC was purified with the described large-scale purification protocol.

First, the binding of mRAC to 80S DPAP-RNCs from wheat germ (wg80S) was analyzed. From previous studies it is known that some heterologous complexes with wheat germ 80S ribosomes (wg80S) turned out to be a stable combination and thus perfect for cryo-EM. Successful examples are the structures of wheat germ 80S RNCs with mammalian SRP (Halic et al., 2004) and with the mammalian Sec61 complex (Becker et al., 2009), where artificially stable complexes with the wheat germ ribosome

could be formed. A stoichiometric binding of mRAC to wheat germ 80S RNCs was detected in the SDS gel of the reconstitution experiment indicated by two bands of mRAC (MPP11 and Hsp70L1) in the pellet fraction, having the same range of intensity as the ribosomal bands (Fig. 22). The experiment showed also a comparable binding of mRAC to 80S DPAP90-RNCs and to 80S DPAP120-RNCs (Fig. 22). The data indicate

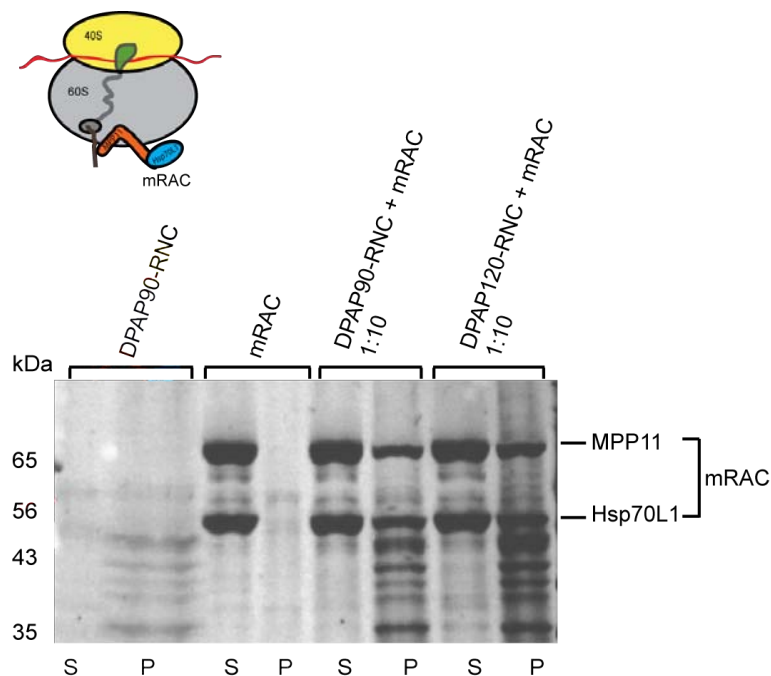


Figure 22.: Reconstitution of a wheat germ 80S DPAP-RNC mRAC complex (80S RNC mRAC complex) using 100 mM KOAc. (P - pellet; S - supernatant)

the formation of a high affinity 80S RNC mRAC complex under low salt conditions of 100 mM KOAc without a clear discrimination of the length of the nascent chain.

Most of the biochemical informations about eukaryotic ribosome-associated chaperones comes from the well studied chaperone triad of yeast. RAC binds independently of the presence of nascent chains to un-programmed yeast 80S ribosomes (y80S) (Fig. 23a) under low salt conditions of 100 mM KOAc, which is consistent with previous biochemical data (Raue et al., 2007). The amount of 80S-bound RAC remained constant over the tested molar range of 20 to 100 times molar excess of RAC over 80S ribosomes (Fig. 23a). The binding of RAC to yeast 80S ribosomes can be saturated, indicating a specific interaction with the ribosome (Fig. 23a). It is apparent that RAC binds substoichiometrically to 80S ribosomes which is true for low salt conditions (Fig. 23a), whereas the binding was drastically reduced and nearly not detectable under high salt conditions of 500 mM KOAc in reconstitution assays (data not shown). This is in agreement with

recent data, showing that the interaction of RAC is salt sensitive and that $\sim 50\%$ of bound RAC is already released at 340 mM KOAc (Peisker et al., 2008). The 80S-RAC interaction is highly destabilized with increasing salt concentrations showing that the binding is most likely mediated by electrostatic interactions. The binding of RAC to 80S DPAP90-RNCs is also substoichiometric (Fig. 23b), which is in agreement with the fact that RAC does not interact with the nascent chain and shows therefore a similar binding as observed for the un-programmed 80S-RAC interaction (Fig. 23a). Consistent with previously published *in vivo* data (Raue et al., 2007), Ssb1 can bind alone to 80S RNCs even when RAC is not present (Fig. 23b). Since Ssb1 is known to be the only active Hsp70 of the chaperone triad showing ATPase activity, AMPPNP (non-hydrolyzable ATP analog) and ADP was added to the reaction. No difference in the binding of RAC and Ssb1 to 80S RNCs could be detected when AMPPNP or ADP was added (Fig. 23b) and the interaction was still substoichiometric and remained on a similar level as it was observed for the 80S-RAC interaction (Fig. 23a). Thus, the Ssb1 binding to RNCs was

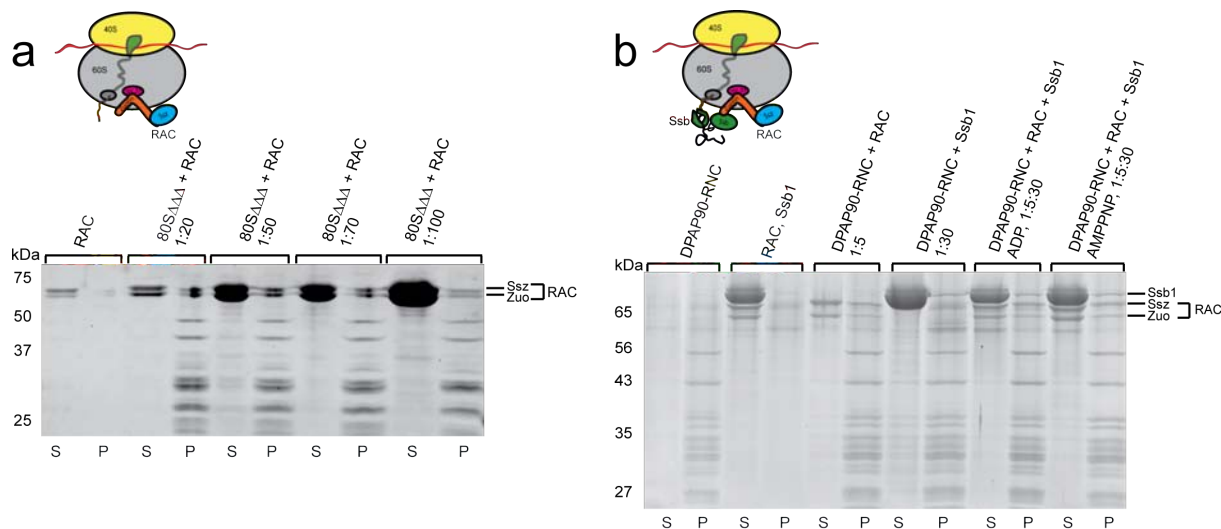


Figure 23.: Reconstitution of yeast 80S RAC complexes. | (a) RAC binding to un-programmed 80S ribosomes can be saturated. (b) Reconstitution of the 80S DPAP-RNC RAC and - RAC-Ssb1 complex from yeast. (low salt conditions - 100 mM KOAc; P - pellet; S - supernatant)

not influenced by the nucleotide state in this assay. It has been shown that the RNC-Ssb1 interaction is not affected by ATP, which normally destabilizes the Hsp70-substrate interaction, suggesting a direct association of Ssb1 with the ribosome independent of the nascent chain (Pfund et al., 1998). Compared to the substoichiometric binding of RAC to yeast 80S the interaction of mRAC with 80S RNCs appeared to be stoichiometric in

the reconstitution experiments, most likely due to the higher affinity of the mRAC binding. Both, the yeast and the wheat germ RNC-RAC samples could be characterized as good cryo-EM samples and structures of the reconstituted complexes were determined.

7.3.1. 80S ribosomes with rpL25-Ssb1 fusion (80S-Ssb1)

The aim of this approach was to stabilize the transiently acting Ssb1-RAC ensemble at the ribosome by a permanent presence of one of the binding partners. For that reason, the Hsp70 chaperone Ssb1 was fused via a flexible peptide linker to the ribosomal protein rpL25 (Fig. 24c). The increased local concentration of Ssb1 at the ribosomal exit tunnel

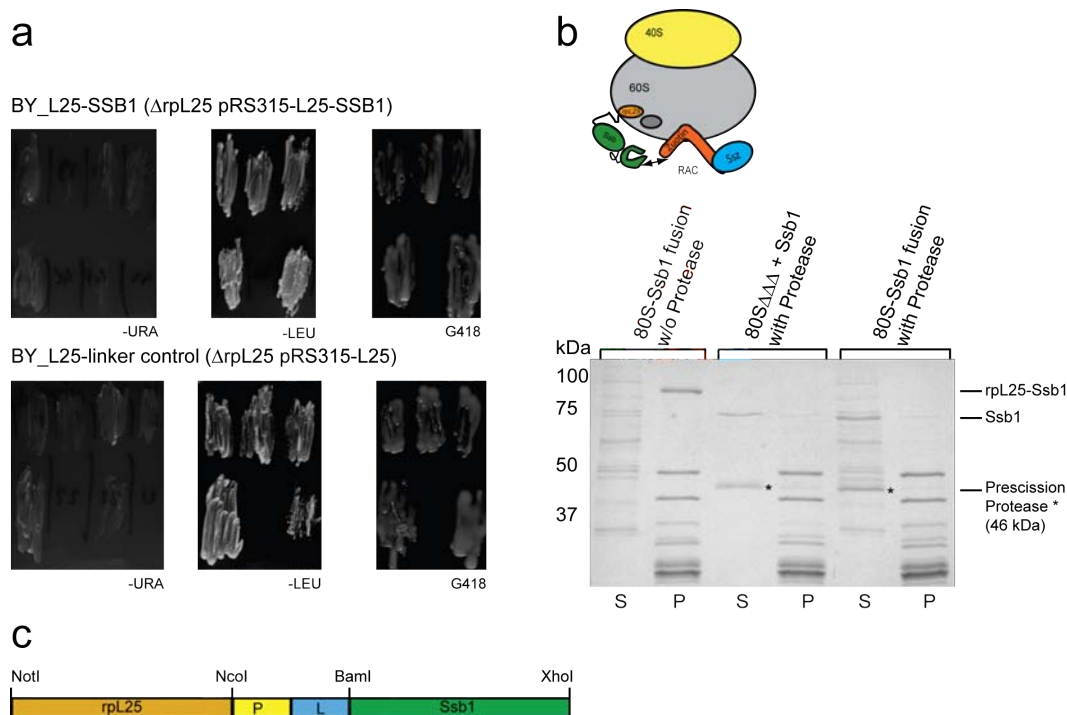


Figure 24.: Generation of modified 80S ribosomes with rpL25-Ssb1 fusion. | (a) The haploid yeast strain BY_L25-SSB1 (Δ rpL25 pRS315-L25-SSB1) was generated and tested under selective growth conditions. (b) Ssb1 can be cleaved from yeast 80S-Ssb1 ribosomes under high salt conditions. (c) Design of the rpL25-Ssb1 fusion construct. (P - pellet and S - supernatant; G418 = 420 μ g/ml G418; L - 15 aa flexible peptide linker; P - Precision protease cleavage site; 80S $\Delta\Delta\Delta$ - 80S ribosomes of the Δ RAC Δ NAC Δ Ssb1 knock out strain IDA123456A)

could potentially increase the binding of Ssb1 to the nascent chain, to the ribosome itself and to its J-protein binding partners Zuotin. It is known from previous studies that rpL25 can be modified at its C-terminus and fused with GFP, which was used

as a reporter construct to study 60S nuclear export (Hurt et al., 1999; Dalley et al., 2008). Yeast cells were genetically modified to generate 80S ribosomes with a fusion of Ssb1 to the C-terminus of the ribosomal exit tunnel protein rpL25. Based on a diploid yeast strain with only one copy of RPL25 (BY4743, RPL25::kanMX4/rpl25), the haploid fusion strain BY_L25-SSB1 (Δ rpl25 pRS315-L25-SSB1) was generated by sporulation, tetrad dissection and selective growth conditions (for details see Materials and Methods). The yeast strain BY_L25-SSB1 was verified under three conditions of selective growth. The cells did not grow on URA deficient media, showing that the BY_L25-SSB1 cells replaced their pRS316-L25(CEN, URA3) plasmid during FOA selective growth (Fig. 24a). But the cells grew on LEU deficient plates and on plates with the eukaryotic antibiotic kanamycin (G418) (Fig. 24a), meaning that the cells have a pRS315-L25-SSB1(CEN, LEU2) plasmid and a kanamycin resistance cassette. The modified yeast 80S ribosomes with fused Ssb1 (80S-Ssb1) were isolated from the yeast strain BY_L25-SSB1 (see Materials and Methods) and analyzed by SDS-PAGE. The isolated ribosomes showed a shift of the rpL25 band to a molecular weight of around 80 kDa, which is the expected molecular weight of the rpL25-Ssb1 fusion protein with around 82 kDa (Fig. 24b). The rpL25-Ssb1 fusion was also verified by western blot analysis against rpL25 (data not shown). Furthermore, the fusion with rpL25 could be cleaved specifically by adding Precission protease and Ssb1 remained in the supernatant fraction under high salt conditions of 500 mM KOAc, showing that the inserted protease cleavage site can be used for the selective cleavage of the fused Ssb1 (Fig. 24b). The rpl25-Ssb1 fusion has shown that the cells are viable and the generated haploid strain BY_L25 (Δ rpl25 pRS316-L25) can be used as a platform for a fusion of other exit tunnel ligands, like Zuo1 or Ssz to rpL25. The modified 80S-Ssb1 ribosomes of the strain BY_L25-SSB1 were analyzed by cryo-EM.

7.4. Cryo-EM analysis

Structures of 80S RAC complexes from different organisms were reconstructed by means of cryo-EM and single particle analysis to get structural insights into the interaction of RAC with the 80S ribosome. The datasets were either recorded on a Tecnai F30 cryo-microscope at 300 kV or on a Tecnai Spirit G12 cryo-microscope at 120 kV under low-dose conditions. All densities were isolated using binary masks and the datasets were processed with the SPIDER software package (Frank et al., 1996). After automated particle

picking with SIGNATURE (Chen & Grigorieff, 2007) followed by visual inspection with WEB (Frank et al., 1996) 59,000 particles were selected for the wg80S RNC mRAC dataset. The dataset was sorted for the presence of P-site tRNA (P-tRNA) and the final CTF-corrected reconstructions had a resolution of around 15 Å (for details see 9.3.1 in Materials and Methods). The map of the wg80S RNC mRAC complex shows the typical appearance of a programmed wheat germ 80S ribosome with a clear density for the P-tRNA in the intersubunit space (Fig. 25a). However, the cryo-EM reconstruction

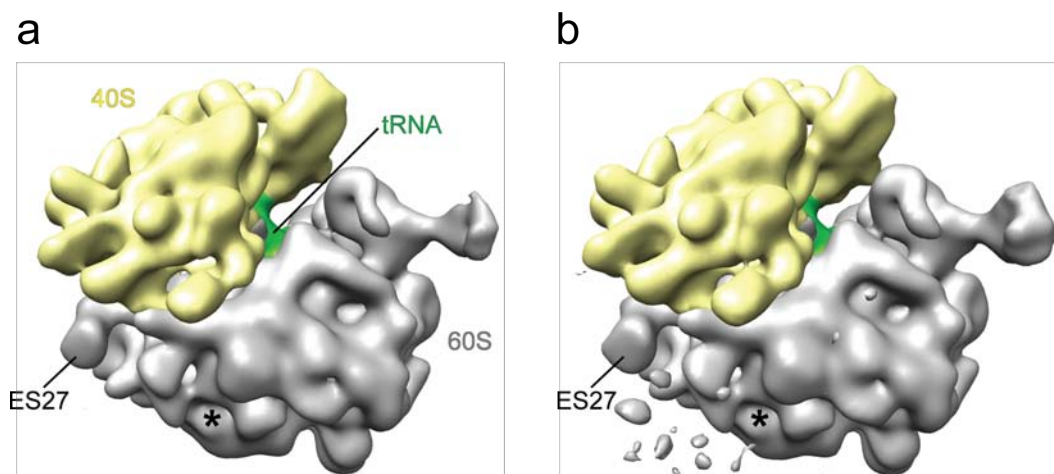


Figure 25.: Cryo-EM map of wg80S RNC mRAC complex. | The map was filtered at 18 Å and is shown at (a) high contour level and (b) at low contour level. (ES27 - part of the rRNA expansion segment 27; position of the exit tunnel is indicated by asterisks (*))

shows no clear additional density for the ligand mRAC in the exit tunnel region (Fig. 25a). At low contour level fragmented density for mRAC appears near the exit tunnel, which could not be interpreted further (Fig. 25b). The fragmented appearance of the density indicates a flexible binding of mRAC to the 80S ribosome, leading to a loss of density information.

Eukaryotic ribosome-associated chaperones are best characterized for *S. cerevisiae*. For that reason the 80S DPAP120-RNC RAC-Ssb1 complex from yeast (80S RNC RAC-Ssb1 complex) was reconstructed. In yeast 80S ribosomes the characteristic and dynamic rRNA expansion segment ES27 forms a 150 Å long rRNA helix that is stabilized in two distinct conformations (Beckmann et al., 2001). In its L1 conformation (ES27-L1) the rRNA arm of ES27 is directed towards the ribosomal protein rpL1 and ES27 does not interfere with the exit site (Fig. 26a). In the ES27-exit conformation the RNA arm is rotated 90° counter clockwise and positioned over the exit site (Fig. 26b).

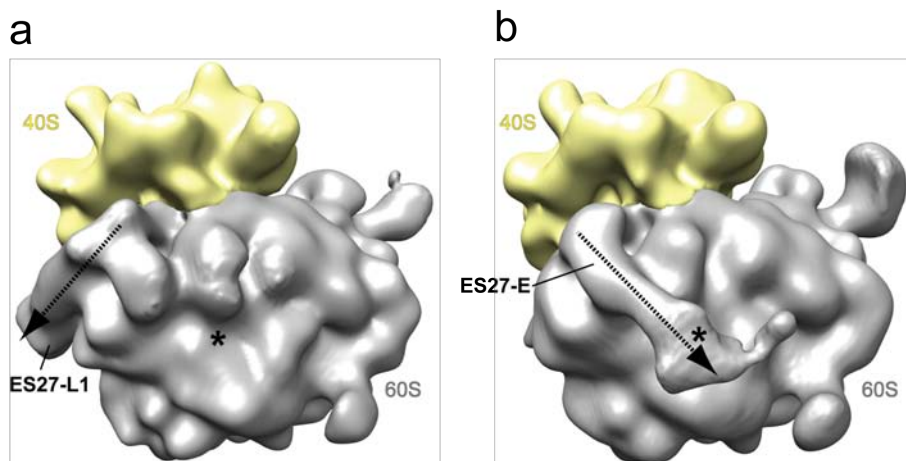


Figure 26.: ES27 conformations in yeast. | Maps of 80S RNCs with ES27 in its L1 conformation (a) and in its exit conformation (b). The tip of ES27 is indicated by an arrowhead. (ES27-L1 and ES27-E - L1- and exit conformation of ES27, respectively; tunnel position indicated by asterisk (*))

Thus, in its exit conformation ES27 interferes with ligands that bind in the exit tunnel region, such as RAC or Sec61. Around 50,000 particles of the 80S RNC RAC-Ssb1 dataset were selected and it was sorted in two steps. First the data were classified for ES27 conformations, resulting in 34,000 particles with ribosomes having the ES27-L1 conformation and 16,000 particles remained for the ES27-exit conformation. The sub-dataset with ES27-L1 conformation was further sorted for the presence of RAC density, resulting in 18,000 particles with additional RAC density and 16,000 particles without a ligand density, respectively. The classified reconstruction of the 80S RNC RAC-Ssb1 dataset shows a programmed yeast 80S ribosome with density for ES27 in its L1 position (Fig. 27a). Strikingly, the reconstruction revealed a clear additional density near the exit tunnel (Fig. 27a). This extra density can be assigned to the 80S-bound RAC. The density is directly connected to the known interaction partner of RAC, the ribosomal protein rpL31 (C1) (Peisker *et al.*, 2008). Peisker *et al.* showed that RAC is anchored to the ribosome via a second binding partner, which they expected to be RNA. Consistent with these findings a second binding site (C2) is resolved in the map (Fig. 27b) that can be assigned to helix H59 of the 28S rRNA (Fig. 28). It is clear that the observed density can only comprise the direct 80S-bound part of RAC (Fig. 28). First, the density is significantly smaller than the low resolution SAXS model of RAC and only a part of the SAXS model fits into the density (Fig. 29). Second, the density is not large enough to comprise the molecular mass of RAC with 110 kDa. Third, a density for Ssz is not resolved in the map, which is in agreement with the SAXS model of RAC showing a

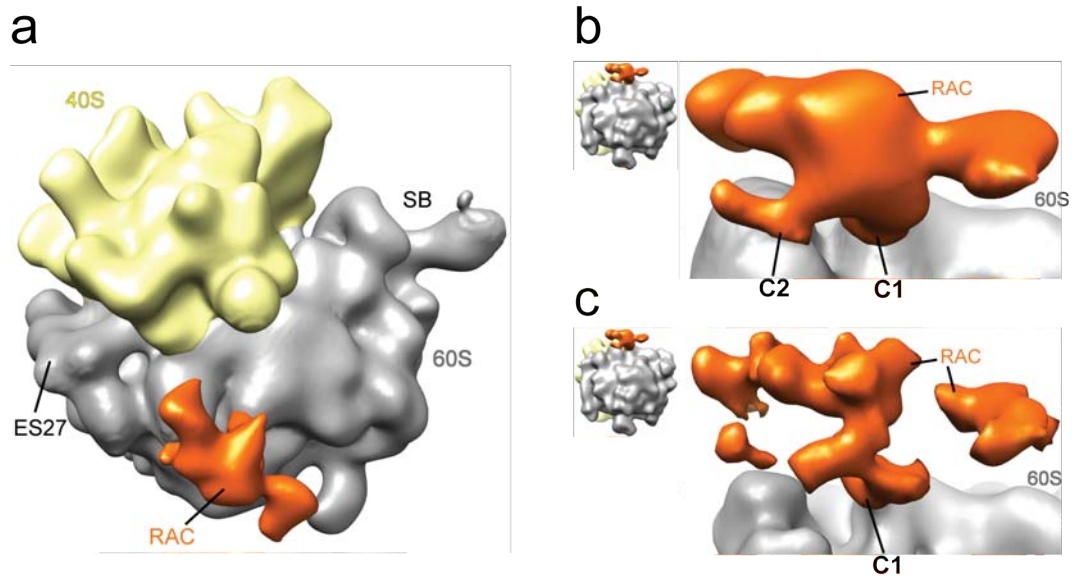


Figure 27.: Cryo-EM reconstruction of the 80S RNC RAC-Ssb1 complex. | (a) Side view of the map with extra density for RAC at the exit tunnel region. Close-up view of the RAC density, filtered (b) at 29 Å and (c) at 16.5 Å using a low-pass gauss filter. (ES27 - L1 conformation of ES27; C1/C2 - two binding sites of RAC with the 60S)

broad spectra of conformations in the Zuotin part (Fig. 29) by which RAC is anchored to the ribosome (Gautschi et al., 2001).

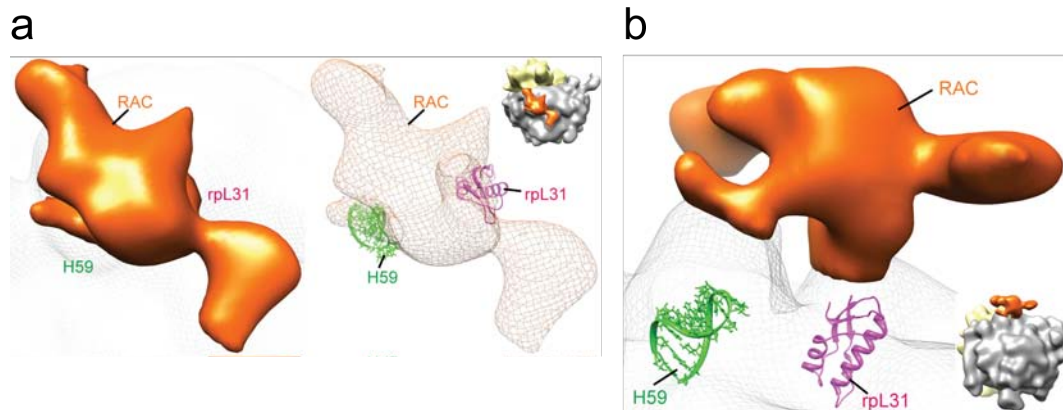


Figure 28.: RAC binding site at the 80S ribosome. | RAC binds to rpL31 and to the rRNA helix H59. (a) Top view of the isolated RAC density and density shown as mesh. (b) Side view, showing the interaction partners. Thumbnails show the overall orientation. (RAC - orange; 60S - gray mesh; rpL31 - magenta; H59 - green)

Therefore, the resolved density can be assigned to be part of Zuotin that is bound

to the ribosome via the binding partners rpL31 (C1) and the RNA helix H59 (C2). However, the main binding site of RAC seems to be formed by the contact C1 (rpL31). The connection to the second binding partner helix H59 (C2) is lost when the map is filtered at higher spatial frequency, meaning that details up to 16.5 Å are still resolved in the map (Fig. 27c). In addition, the entire RAC density appears more fragmented at 16.5 Å (Fig. 27c) when more high frequency information is present, compared to the low resolution map having only details up to 29 Å present (Fig. 27b).

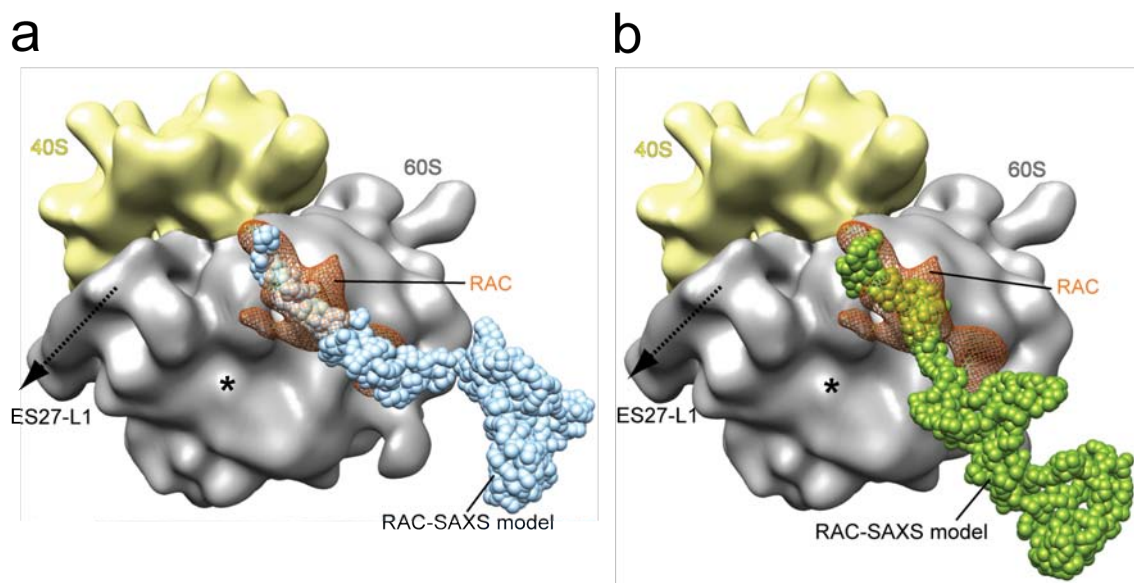


Figure 29.: Two SAXS models of RAC fitted into the cryo-EM map. | (a) and (b) The 80S RNC RAC-Ssb1 complex with SAXS models docked into the RAC density. The SAXS models are the same as in Fig. 21c. RAC density is shown as orange mesh. (60S - gray, 40S - yellow, RAC models - blue and green)

The tendency of the RAC density to fragment at higher resolution indicates a flexible interaction of RAC with the 80S ribosome. Consistent with the assumption that a flexible interaction is the reason for a loss of density information, no extra density for the second ligand Ssb1 is resolved in the map of the 80S RNC RAC-Ssb1 complex. The Hsp70 chaperone Ssb1 is thus not stabilized upon ribosome binding leading to a loss of density information for the flexibly bound Ssb1.

The 80S-Ssb1 RAC dataset was determined on a Tecnai Spirit G12 cryo-microscope. After automated particle picking and visual inspection around 14,000 particles were selected for the 80S-Ssb1 RAC dataset. The data were classified for the two distinct ES27 conformations. After sorting around 3,100 particles remained for the ES27-exit conformation and 10,700 particles were sorted out with ES27-L1 conformation. The

previously described 80S ribosomes with the rpL25-Ssb1 fusion (80S-Ssb1; see also 7.3.1) were used to reconstitute the 80S-Ssb1 RAC complex. The structure of the 80S-Ssb1

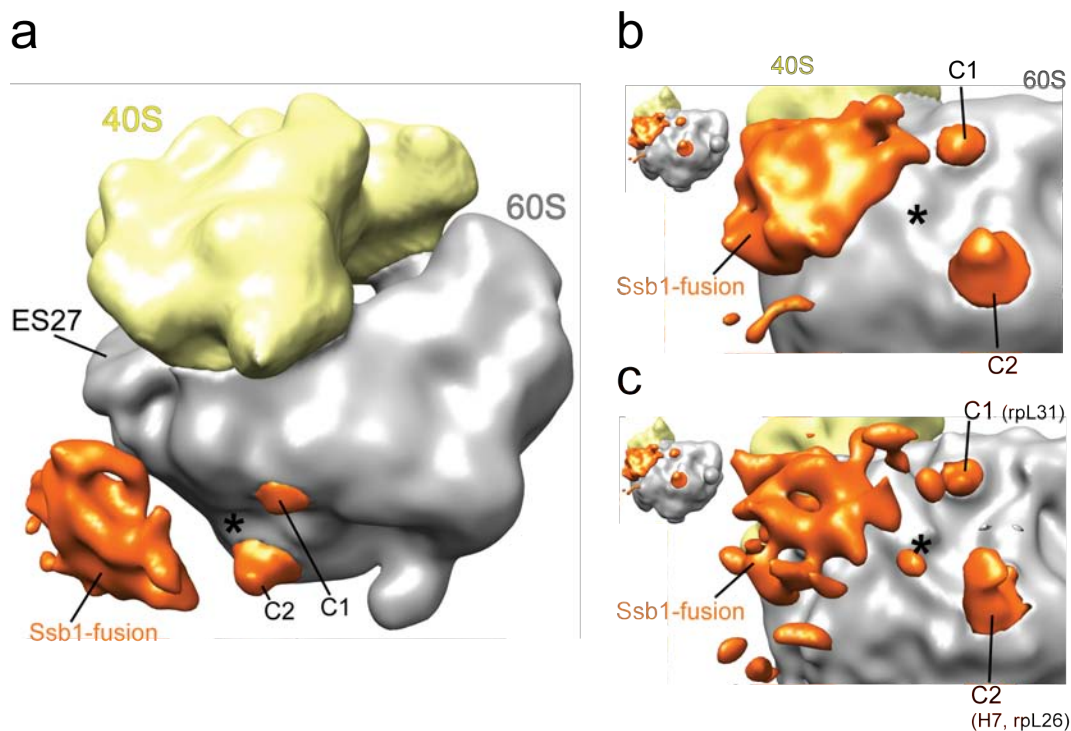


Figure 30.: Cryo-EM reconstruction of the 80S-Ssb1 RAC complex. | (a) Side view of the map with additional densities at the exit region. Close-up view of the exit site of the same map, filtered at 22 Å (b), and filtered at 19.5 Å (c) using a low-pass gauss filter. Thumbnails show the overall orientation. (ES27 - L1 conformation of ES27; C1/C2 - additional contacts, with nearest ribosomal component in brackets; position of the exit tunnel is indicated by asterisks (*))

RAC complex with a resolution of around 20 Å revealed a yeast 80S ribosome with an additional density at the exit site (Fig. 30a). After sorting of the dataset against the two distinct conformations of ES27, the resulting map shows a clear density of ES27 in its L1 conformation (Fig. 30a). Therefore, it can be excluded that the additional density is part of ES27 and the extra density can be identified as the fused Ssb1 (Fig. 30a). Furthermore, the position of the observed extra density is near the expected region of rpL25 to which Ssb1 was linked. The density of the fused Ssb1 appears more fragmented when the map is filtered at a spatial frequency that corresponds to 22 Å in real space (Fig. 30b), compared to the result when the map is filtered at 19.5 Å (Fig. 30c). Even though the linked Ssb1 is permanent present at the ribosomal exit tunnel it is not stabilized in a defined conformation, indicating a flexible interaction of Ssb1

with the ribosome. In addition, two extra densities are resolved in the map, marked as contacts C1 and C2 (Fig. 30b). The extra density contact C1 is located in the vicinity of rpL31. It is tempting to speculate that C1 is part of RAC, since the position of C1 is in good agreement with the RAC crosslink to rpL31 (Peisker et al., 2008). The second contact C2 is of unknown origin and it is positioned near the rRNA helix H7 (H7) and the ribosomal protein rpL26. Due to the intermediate resolution of the map only a preliminary interpretation of the additional densities can be done and no further information for RAC is resolved in the reconstruction.

7.5. Conclusions

In this study, the established purification protocol for RAC and the mutant RAC Δ Zuo110 was used to generate a pure and well defined sample suitable for SAXS analysis. The low resolution SAXS model of RAC revealed an elongated complex with conformational flexibility in its Zuotin part. The cryo-EM reconstruction of the 80S RNC RAC-Ssb1 complex showed that RAC binds indeed via a mixed RNA-protein interaction to the yeast 80S ribosome involving the two binding partners rpL31 and the rRNA helix H59 of the ribosomal exit tunnel. This result is in agreement with previously published data, where a crosslink to rpL31 and the involvement of RNA has been described (Peisker et al., 2008). In the same study it has been shown that the 80S binding of RAC is highly salt sensitive (Peisker et al., 2008). Therefore, the binding site of RAC which is formed by rpL31 and H59 is most likely mediated by electrostatic interactions. RAC does not physically interact with nascent chains but it prefers to bind to translating ribosomes (Raue et al., 2007) most likely due to the increased presence of the co-chaperone partner Ssb. In the reconstitution experiments a substoichiometric binding of RAC to yeast 80S and to RNCs was found (Fig. 22a and 23), which is typical for a low affinity interaction. Depending on the degree of flexibility the flexible part becomes fragmented or even invisible in a cryo-EM reconstruction as a result of “conformational averaging” (Penczek et al., 2006), due to a loss of information (see also 3.2 in Introduction). Besides flexibility the observed low affinity binding of RAC and Ssb1 to the ribosome will result in a substoichiometric occupancy. Below a certain threshold of occupancy (around 30 %), the affected ligand density appears also as fragmented density or it is invisible as a result of loss of information (Penczek et al., 2006). In the case of the interaction of RAC and Ssb with the ribosome both, flexibility and low occupancy contribute to a loss of density information but most likely the influence of flexibility is higher. Consistent

with this assumption, the binding assay of the heterologous wg80S RNC mRAC complex showed a stoichiometric binding of mRAC to the RNCs (Fig. 22b), however, the cryo-EM map of the complex revealed only fragmented densities at low contour levels at the exit site. A distinct additional density for the fused Ssb1 could be observed in the map of the 80S-Ssb1 RAC complex, but the density appeared fragmented when more high frequency information corresponding to high resolution details were present as a result of filtering (Fig. 30c). This result also indicates a flexible interaction of Ssb1 to the yeast ribosome and to RAC. A high degree of flexibility in the ribosome binding of the RAC-Ssb1 ensemble is also confirmed by the fact that no solid extra density of RAC is resolved in the 80S-Ssb1 RAC structure. It is known that the binding of Ssb to un-programmed ribosomes is salt sensitive but stabilized through the presence of the nascent chain (Pfund et al., 1998). It has been shown that Ssb prefers to bind to RNCs with PGK (Phosphoglycerate kinase) as nascent chain (Raue et al., 2007). But also the reconstruction of a 80S PGK-RNC RAC-Ssb1 complex (data not shown) showed not an interpretable density for one of the ligands, indicating that the binding of RAC and Ssb1 was not significantly stabilized by the presence of a cytosolic nascent chain. This finding is supported by data that show that Ssb seems to be an unusual and fungal-specific Hsp70 with unspecific substrate spectra, showing no peptide binding activity to typical Hsp70 substrates *in vitro* (Pfund et al., 2001). Taken together, RAC is an elongated and flexible complex that interacts transiently and with low affinity with the 80S ribosome and with its co-chaperone partner Ssb.

A dynamic interplay: RAC and Ssb form a functional folding unit at the exit tunnel

The key question is, how the eukaryotic chaperone system at the exit tunnel is spatially and temporally organized, and how is it regulated? Four players act together in yeast, namely RAC, Ssb, the 80S ribosome and the nascent chain. The elongated shape of RAC in combination with its flexibly bound Zuotin part would allow a large operation radius for the complex around the ribosomal exit tunnel, indicated by an arrow in Fig. 31a and b. The working horse of the chaperone system is Ssb, which is mainly modulated by the presence of RAC and the nascent chain. Compared to the more simple situation in prokaryotes the eukaryotic system is even more complicated, due to the presence of the dynamic rRNA expansion segment ES27 in eukaryotic ribosomes, which sterically interferes with the ribosomal exit site (Fig. 26b). In this context it is

highly interesting to ask, if ES27's conformational states can act as a coordinator for ligands of the exit site in yeast, either indirectly by a pure sterical regulation or directly by an interaction with ligands, like RAC, Ssb or NAC (Fig. 26b)? These questions might only be clarified by a combination of different methods and better resolution, including a crystal structure of RAC, that is needed for a molecular interpretation of the cryo-EM data. As demonstrated in this work, the ribosome-associated chaperone system of

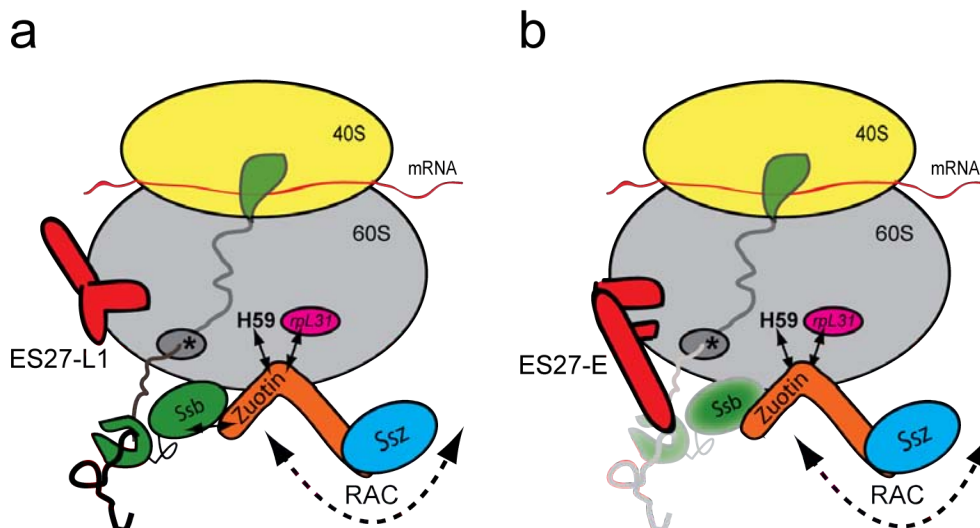


Figure 31.: A functional folding unit at the tunnel exit. | The dynamic interplay of RAC and Ssb at the exit tunnel might be regulated by ES27 conformations. (a) Model of the ribosome-associated chaperone triad in yeast with ES27 in its L1- and (b) in its exit conformation (ES27-E). (H59 - helix 59; tunnel indicated by asterisk(*))

yeast acts in a dynamic interplay, whereby the folding is realized for a broad spectra of nascent chains by a cooperative action of Ssb and RAC that form a functional folding unit (Fig. 31), which might be regulated by ES27's conformational states and via the competitive binding site rpl31, that is shared with the other nascent chain binder NAC (unpublished data of B. Beatrix).

The only structural informations about the function of ribosome-associated chaperones arise from 50S crystal structures with the bound TF binding domain (Schlünzen et al., 2005; Ferbitz et al., 2004). The current model of Ban and coworkers (Kramer et al., 2009) for the bacterial system, also called 'concerted model' (Giglione et al., 2009), proposes a concerted action of TF and PDF (peptide deformylase) at the tunnel exit, based on the concomitant positioning of the factors, which was concluded from co-crystal structures (Ferbitz et al., 2004; Bingel-Erlenmeyer et al., 2008). In this model the

emerging nascent chain interacts first with TF, which is supposed to form a hydrophobic 'cradle' (Ferbitz et al., 2004) that serves as a shielded folding environment beneath the exit tunnel and that passively routes the chain for first co-translational modifications to PDF and afterwards to MAP (methionine aminopeptidase). In contrast to the 'concerted model' (Giglione et al., 2009) proposed for the prokaryotic RPBs, our data suggest a more dynamic view rather than a hierarchical sequence of the actions at the eukaryotic exit tunnel, which was also discussed by other publications (Yonath, 2006; Kaiser et al., 2006; Giglione et al., 2009). The concerted mechanism of the bacterial system is based on static ribosomal X-ray structures without a nascent chain, where only a small and most stable part of the dynamic ligand is present (Ferbitz et al., 2004; Bingel-Erlenmeyer et al., 2008), whereas cryo-EM reconstructions are based on native complexes.

Outlook

The main challenge for future work is to deal with the intrinsic flexibility of the system. Basically there are two approaches, either by biochemical methods or by the use of sophisticated sorting methods that handle the problem on data processing level. An unsupervised classification method called 'focused classification' (see also 3.2 of the Introduction) uses 3D variance analysis as basis for the sorting of heterogeneous datasets (Penczek et al., 2006). With this unsupervised classification method it might be possible to sort out different conformations of 80S-bound RAC and Ssb1 based on a high quality dataset with good contrast. The rpL25 fusion approach can be extended to generate modified 80S ribosomes fused with Zuotin that should result in a permanent presence of RAC at the ribosomal exit site and which might have the potential to open the door to visualize the complete RAC-Ssb triad at the ribosome by cryo-EM. As demonstrated in this study, a comprehensive view of this flexible system can only be reached if different methods will be combined. It can be tried to record SAXS data of a 80S RAC complex. Recently published SAXS methods can provide low resolution models of flexible complexes and even transiently present species in solution (Blobel et al., 2009). SAXS is also not limited by the size of the observed ensemble, which has already been demonstrated for ribosomal SAXS models (Svergun et al., 1997). Biochemical methods can be used to analyze the exact binding environment of RAC at the 80S ribosome for instance by crosslinking experiments coupled with sophisticated mass spectrometry, aiming to identify the involved residues or by site directed mutagenesis, which requires profound structural informations of the binding interface.

Part III.

Materials and Methods

8. Biochemical experiments

8.1. Molecular cloning

8.1.1. Polymerase chain reaction (PCR)

Primers were designed by the programs and the Oligo Properties Calculator (<http://www.basic.northwestern.edu/biotools/oligocalc.html>) and ordered at Metabion (Munich).

PCR was used to amplify DNA from a template, either for cloning or as template for *in vitro* transcription reaction. 100 μ l reactions, comprising 10 μ M of forward and reverse primer, 5-80 ng template DNA, 2 U DNA polymerase, 10 μ l 10x reaction buffer with dNTPs and 2-3 mM MgCl₂ or the kit Phusion Flash High-Fidelity Master Mix[®] (Finnzymes) was used as 20 μ l reaction, where only 10 μ l of the 2x Master Mix, primers and template DNA was added, according to the manufacturer's protocol. In some cases, 100 μ l reaction based on the kit EasyStart PCR Mix-in-a-Tube[®] (Molecular Bioproducts) were used. Reactions were conducted using appropriate cycling programs. Samples were analyzed subsequently by agarose gel electrophoresis.

8.1.2. *In vitro* transcription

Capped mRNA as template for *in vitro* translation reactions, used in the RNC purification, was generated by *in vitro* transcription reaction. The reaction was based on a kit (mMessage mMachine[®] kit, Ambion) and used according to the manufacturer's protocol, to get high yields of capped mRNA, which is needed for an efficient *in vitro* translation reaction. In a typical 20 μ l reaction 1 μ g template DNA was used, the reaction was incubated overnight at 37°C and precipitated by adding 30 μ l LiCl solution and ddH₂O (part of kit) per 20 μ l reaction. After incubation for 2 h at -20°C, reactions were centrifuged, washed with 70 % ethanol, the dried pellets were resuspended in nuclease free water and the concentration was determined by measuring the absorption at 260 nm.

name	composition
100K-BA buffer	20 mM Tris/HCl pH 7.0, 100 mM sucrose, 100 mM KOAc, 7.5 mM Mg(OAc) ₂ , 2 mM DTT, 1 % PIP (complete protease inhibitor pill (Roche)), 10 µg/ml cycloheximide
1 M sucrose cushion	50 mM Tris/HCl pH 7.0, 25 mM Mg(OAc) ₂ , 5 mM β-mercaptoethanol, 1 M sucrose, 10 µg/ml cycloheximide, 0.1 % Nikkol, 0.1 % PIP, 100 mM (low salt) or 500 mM (high salt) KOAc
750 mM sucrose cushion	20 mM Tris/HCl pH 7.0, 750 mM sucrose, 100 mM KOAc, 7.5 mM Mg(OAc) ₂ , 2 mM DTT, 1 % PIP, 10 µg/ml cycloheximide
250 buffer	50 mM Tris/HCl pH 7.0, 250 mM KOAc, 25 mM Mg(OAc) ₂ , 5 mM β-mercaptoethanol, 250 mM sucrose, 10 µg/ml cycloheximide, 0.1 % Nikkol, 0.1 % PIP, 10 units/ml anti-RNAsin (Ambion) <i>250/100 buffer</i> (250 buffer with 100 mM Imidazole); <i>250/tRNA buffer</i> (250 buffer with 10 µg/ml tRNA)
500 buffer	50 mM Tris/HCl pH 7.0, 500 mM KOAc, 25 mM Mg(OAc) ₂ , 5 mM β-mercaptoethanol, 250 mM sucrose, 10 mg/ml cycloheximide, 0.1 % Nikkol, 0.1 % PIP
grid buffer	20 mM Tris/HCl pH 7.0, 50 mM KOAc, 2.5 mM Mg(OAc) ₂ , 1 mM DTT, 125 mM sucrose, 100 µg/ml cycloheximide, 0.05 % Nikkol, 0.5 % PIP
12,5 x E-Mix (energy providing)	12.5 mM ATP, 6.25 mM GTP, 250 mM creatine phosphate, 1.25 mg/ml creatine phosphate kinase, 1.25 mg/ml tRNA
25 x CB (compensation buffer)	332.5 mM HEPES, 2.9 M KOAc, 45.8 mM Mg(OAc) ₂ , 32.5 mM DTT
YPD/Sorbitol	1 M sorbitol in YPD (20 g peptone + 10 g yeast extract + 20 g glucose in 1 L)
buffer PD	100 mM TRIS pH 8,0, 10 mM DTT
YTE-lysis buffer	20 mM Hepes pH 7.5, 100 mM KOAc, 7.5 mM Mg(OAc) ₂ , 1 mM DTT, 0.5 mM PMSF
1.5 or 2 M 80S-sucrose cushion	20 mM Hepes pH 7.4, 7.5 mM Mg(OAc) ₂ , 500 mM KOAc, 1.5 or 2 M sucrose, 1mM DTT, 1mM PMSF, 0.1 % PIP
80S-lysis buffer	20 mM Hepes pH 7.4, 7.5 mM Mg(OAc) ₂ , 100 mM KOAc, 1mM DTT, 1 mM PMSF
buffer A	20 mM Hepes pH 7.0, 100 mM KCl, 2,5 mM Mg(OAc) ₂ , 1 mM DTT
RAC-lysis buffer	40 mM Hepes/KOH pH 7.4, 240 mM KOAc, 0.014 % (v/v) β-mercaptoethanol, 1 mM PMSF, 0.5-1 % PIP
ion exchange buffer1 and 2	buffer1: 40 mM Hepes/KOH pH 7.4 buffer2: 40 mM Hepes/KOH pH 7.4, 2000 mM KOAc
gel filtratton buffer	40 mM Hepes/KOH pH 7.4, 100 mM NaCl

Table 3.: Overview of buffers.

8.1.3. Gel electrophoresis

SDS-PAGE Denaturing discontinuous SDS-PAGE (SDS polyacrylamide gel electrophoresis) was used to separate proteins according to their molecular weights, using standard protocols (Laemmli, 1970). Samples were denatured at 94°C for 4 min, containing 1x sample buffer, and loaded on 12 or 15 % polyacrylamide gels. Electrophoresis was performed at constant voltage of 120-200 V in standard running buffer (25 mM Tris, 192 mM glycine, 0.1 % SDS).

Agarose gel electrophoresis Agarose gel electrophoresis was used to separate DNA and RNA according to their size. Gels were made with 1-2 % agarose in TAE buffer and run for circa 20-40 min at 50 V constant voltage. DNA and RNA molecules were stained with SYBR Green I and II (Molecular Probes), respectively and visualized at a wavelength of 300 nm. DNA markers (Biorad and NEB) were used as molecular weight standards.

8.1.4. Genetic experiments

Yeast cloning was done using kits and standard methods. The cloned constructs were checked by a commercial sequencing service (Eurofins MWG Operon).

Cloning The PCR amplified DNA and the plasmid was digested by restriction digest. A typical 200 µl digestion reaction was composed of 3 µg DNA template, 30 U restriction enzyme, an appropriate 10x buffer and nuclease free H₂O and incubated for 2 h at 37°C. The digestion reaction was purified via a PCR purification kit (QIAquick® PCR purification kit, Quiagen) and the purified digestion products were ligated. For a normal 20 µl kit based ligation reaction (Fermentas), a five fold molar excess of the insert over the plasmid was used, 2 µl 10x ligation buffer, 2 µl 50 % PEG, 5 U T4 ligase and ddH₂O were used. The ligation approach was used for transformation of chemical competent *E. coli* cells (DH5α or TOP-10F kit cells, Invitrogen). The cells were gently thawed on ice, 1/2 of the ligation reaction was added to 50 µl cells, then the reaction was incubated for 10 min on ice and immediately transferred to 42°C water bath for heat shock. Around 1 ml of LB or SOC media (Fermentas kit) was added and the cells recovered while incubating for 30 min at 37°C (Eppendorf Thermomixer). The cell pellet (30 s at 3000 rpm, Eppendorf table top centrifuge) was resuspended in 100 µl LB media and plated onto a selection agar plate for overnight growth at 37°C. Around 10 ml LB media with

primer	5'-3' sequence
L25_fw	CGC GGATCC CATGGGTCACCTATTTAATATGTACGGGTGTTTACATGG
L25_rv	CGC GGATCC GTT GCT GAT GAA AAT AAC CCT GTG TTT TCG C
rpL25-NotI_fw	GATCGGCGGCCGCCATGGGTCACTTATTTAATATGTAC
rpL25-NcoI-L-BamHI_rv	CCTTGGAACACCTTCAGCCATGGATCCGGACCCTCCGCCACCGGGCCCCCTGGAAC AGAACTTCCAGCCATGGAATGTAACCGATTCTGTTAGCAATGTCC
Ssb1-BamHI_fw	GGTGGCGGAGGGTCCGGATCCATGGCTGAAGGTGTTTTCCAAGG
Ssb1-XhoI_rv	CTAGCCTCGAGCTATTAACGAGAAGACATGGCCTTG

Table 4.: Sequences of primers.

antibiotics was inoculated with a single colony and incubated at 37°C overnight. Plasmid were extracted from the overnight cultures using a kit (QIAprep® Spin Miniprep kit, Quiagen) and the purified plasmids were analyzed by restriction digest combined with agarose gel electrophoresis.

Yeast strain with RPL25-SSB1 fusion (BY_L25-SSB1) Yeast cells were genetically modified to generate 80S ribosomes with a fusion of Ssb1 to the ribosomal exit tunnel protein rpL25. The ribosomal protein RPL25 was amplified from genomic DNA (primer L25_fw and L25_rv) and cloned into a pRS316(CEN, URA3) plasmid using BamHI restriction sites, which resulted in the vector pRS316-L25. A heterozygous diploid yeast strain with only one copy of RPL25 (BY4743, RPL25::kanMX4/rpl25; Y26277 Euroscarf) was transformed with pRS316-L25 to generate the strain BY_L25 (RPL25::kanMX4/rpl25 pRS316-L25). The strain BY_L25 was sporulated and tetrads were dissected to get haploid cells of BY_L25 (Δ rpl25 pRS316-L25), having the only copy of the essential gene RPL25 on the plasmid pRS316-L25. The tetrads were analyzed under selective conditions (G418 and FOA) and glycerol stocks of positive tetrads were invested and stored at -80°C. RPL25 was amplified with the primer rpL25-NotI_fw and rpL25-NcoI-L-BamHI_rv, and cloned into pRS315(CEN, LEU2) to generate the plasmid pRS315_linker. SSB1 was amplified from an existing vector (pYCPlac33-SSB1(CEN, URA3), Rospert group) using the primers Ssb1-BamHI_fw and Ssb1-XhoI_rv, and inserted into the plasmid pRS315_linker to generate the plasmid pRS315-L25-SSB1. The ribosomal protein rpL25 was fused via its C-terminus to Ssb1. The strain BY_L25 (Δ rpl25 pRS316-L25) was then transformed with the plasmid pRS315-L25-SSB1. The transformed BY_L25 cells were shifted to FOA plates and incubated at 25°C. The rpL25-Ssb1 fusion protein (pRS315-L25-SSB1) complemented for rpL25 and the grown colonies were analyzed under selective conditions (LEU, URA and G418), to get the

strain BY_L25-SSB1 (Δ rpl25 pRS315-L25-SSB1).

8.2. Purification

8.2.1. Western blot (WB)

Western blot was used for the qualitative detection of tagged nascent chains to track the RNC purification or to check the result of an *in vitro* test translation reaction. For HA tag detection, SDS gels were blotted for 45 min at 75 V constant voltage per gel, in blotting buffer on PVDF membranes, using a standard semi-dry blotting apparatus. Membranes were then stained for 1 min in Amido black, digitized, destained and blocked with 2 % BSA in 1x TBS buffer. The primary antibody (HA-probe (F-7) mouse ab, Santa Cruz Biotechnology) was used in a 1:1000 dilution in 2 % BSA (1x TBS) and incubated overnight at 4°C. The membrane was washed three times á 10 min with 1x TBS-T buffer and the second antibody (goat anti-mouse antibody) was used in a 1:2000 dilution in 5 % milk (in 1x TBS; Roth) and incubated for > 1 h at RT. Membranes were washed again three times with TBS-T buffer and signals were detected by ECL reaction (self-made solutions or Chemiluminescent Detection kit, AppliChem) and films (GE Healthcare).

8.2.2. TCA precipitation

TCA precipitation was used prior to western blot analysis or reconstitution experiments, to concentrate proteins out of highly diluted reaction mixtures. To each reaction, 150-200 μ l of 72 % trichloroacetic acid (TCA) and 0,15 % sodium deoxycholate were added and the overall volume was adjusted to 1 ml with ddH₂O. Reactions were incubated overnight at -20°C, centrifuged, the resulting pellet was washed once with 100 % acetone p.a. and finally 10 μ l sample buffer was added to the dried pellet for SDS-PAGE.

8.2.3. SYPRO orange staining

The SDS gels were stained with SYPRO orange for detection of small amounts of proteins (< 100 ng per 0.5 cm lane), used in reconstitution assays. Gels were washed for 1 min in 7.5 % acetic acid and stained in the dark for > 1 h at RT, in a solution of 1:5000 SYPRO orange in 7.5 % acetic acid. The gels were washed for 30 s in 7.5 % acetic

acid and visualized at 480 nm excitation wavelength (580 nm emission filter, 590 V sensitivity) with a Typhoon scanner (Typhoon 9400, Amersham).

8.2.4. Preparation of yeast translation extract (YTE)

A YTE was prepared to utilize an *in vitro* translation, enabling us to purify yeast 80S RNCs. Two well-aerated 10 L bottles were inoculated with an overnight pre-culture to OD_{start} of $< 0.03 OD_{600}$. The cells were harvested after overnight growth at 30°C at $1.5\text{-}2 OD_{600}$. Around 20 L of yeast cells were harvested in several runs (10 min at 5000 rpm, 4°C , SLC-6000 rotor), using 1 L buckets, and washed with cold water. The pooled cells were weighted in 500 ml buckets, washed with cold 1 % KCl, resuspended in buffer PD (around 200 ml buffer PD per 50 g cells) and incubated for 15 min at RT. Cells were centrifuged (10 min, 5000 rpm, GS3 rotor) and resuspended, using 1 ml YPD/sorbitol per 0.3 g cells. To digest the cell wall and generate spheroblasts, 0.625 mg zymolyase (20,000 U/g (20 T), MP Biomedicals) was added per 1 ml volume and the reaction was incubated for 1 h at 30°C . After 5 min on ice, the cells were centrifuged (10 min, 5000 rpm, GS3 rotor) and washed three times with 200 ml of YPD/sorbitol. The cells were resuspended in YPD/sorbitol and incubated for 1 h at 30°C for recovery. The cells were washed with 1M sorbitol and then resuspended in a small volume of YTE-lysis buffer (< 10 ml per 50 g cells). Cells were lysed with manually with around 15 strokes in a tight glas douncer (40 ml douncer, Wheaton USA) and centrifuged (15 min at 15,500 rpm, SS-34 rotor). The supernatant was transferred and ultra-centrifuged to isolated the cytosolic fraction (30 min at 37,000 rpm, 4°C , Ti70 rotor). Only the clear fraction of the supernatant was carefully isolated (YTE) and the concentration was determined at OD_{280} . Finally, PD-10 gel filtration columns were equilibrated three times with 5 ml TE buffer, then 2.5 ml of the YTE was loaded on one column, the column was washed with 0.75 ml TE buffer, 2 ml TE buffer was added and the flow through was collected. Again OD_{280} was determined and the endogenous mRNA of the YTE was digested by S7 nuclease treatment, using normally 10 U S7 nuclease per ml YTE. The YTE was adjusted to 0.8 mM CaCl_2 , S7 nuclease was added, the reaction was incubated for 15 min at RT and stopped by incubation on ice plus adjusted to 2 mM EGTA (pH 8.0). Aliquots were flash frozen in liquid N_2 and stored at -80°C .

component	volume (μl)
12,5 x E-Mix (energy providing)	96
25 x CB (compensation buffer)	48
amino acid mix	48
1 M Tris pH 6.8	48
RNAsin	10
YTE	400
anti-RNAsin (Ambion)	10
ddH ₂ O	ad 1200
mRNA	4.8 μg per 100 μl volume

Table 6.: Reaction mix of a typical 1.2 ml *in vitro* translation reaction used for RNC purification.

8.2.5. Purification of 80S RNCs

Cell free *in vitro* translation reaction (IVT) based on a self-made YTE, was used to program yeast 80S ribosomes by the use of specific truncated mRNA without a stop codon, as previously described (Beckmann et al., 1997). A typical *in vitro* translation reaction for RNC purification was composed as shown in table 6.

The IVT mix was incubated in 100 μl PCR tubes at 17-20°C for 75 min, then pooled and stopped by adding 4 μl of 10 mg/ml cycloheximid per 100 μl reaction volume. 80S ribosomes were pelleted by centrifugation (45 min at 100,000 rpm, 4°C, TLA 120.2 rotor), loading 200 μl IVT mix onto 800 μl 1 M sucrose cushion (6 tubes) and each pellet was resuspended in 500 μl 250 buffer by incubation for 45 min on ice. Two columns (BioRad) were loaded each with 1 ml resin material (TALON metal affinity resin, Clontech), equilibrated with 5 ml 250/tRNA buffer to minimize unspecific binding. Around 1.5 ml of the resuspended 80S were loaded on one column and the reaction was agitated for 5 min at RT. Next, the flow through was collected, the columns were washed each with 1.5 ml 250 buffer, followed by an intensive washing procedure (12 ml 250 buffer and high salt wash with 3.5 ml 500 buffer per column). The bound RNCs were eluted by addition of 1,5 ml 250/100 buffer, whereby the columns were agitated for 5 min at RT. The flow through was collected, again 2.25 ml of 250/100 buffer was added, the complete collected flow through was centrifuged to isolate the 80S RNCs (around 3 ml eluate loaded onto 500 μl 1 M sucrose cushion; 45 min at 100,000 rpm, 4°C, TLA 100.4 rotor) and the supernatant was immediately removed. The pellets were resuspended in

a small volume of grid buffer by incubation for 45 min on ice. Concentration of the pooled RNCs was determined at OD₂₆₀ and small aliquots were flash frozen in liquid N₂ and stored at -80°C. The average yield of a 1.2 ml yeast IVT reaction was between 1.5 to more than 2 OD₂₆₀. An aliquot was taken at each step of the purification and a negative control was run without mRNA, the samples were analyzed by SDS-PAGE and western blot.

The purification of wheat germ 80S RNCs followed exactly the same protocol, except for some minor variations: the reaction mix had a different composition (1.2 ml reaction: 600 µl wheat germ extract (Ambion kit or self-made wheat germ extract), 60 µl aa mix, 1M KOAc pH 7.0, 4µg/ml mRNA, with ddH₂O ad 1200 µl volume) and the incubation was conducted at 26°C for 45 min.

80S DPAP RNCs A forward T7 standard primer and a specific reverse primer were used to generate DPAP constructs of different length (DPAP90 and 120) and PGK constructs. The RNC purification followed the protocol, described before.

80S Helix RNCs The helix1 construct was chemically synthesized by Eurofins (Martinsried, Germany). DNA template for transcription was prepared using T7 standard and reverse (5'-ATCGTAGACAGATTTAACAAC-3') primers by PCR. The helix2 construct was generated by PCR using a standard T7 primer with a modified reverse (5'-ATCGTACTCGAGACCACCAGCTTTAG-3') primer, with helix1 construct as the template. Uncapped transcripts were then synthesized from the PCR fragments using T7 RNA polymerase. 80S Helix-RNCs were generated using a self-made wheat germ *in vitro* translation system programmed with truncated mRNA encoding the helix1 and 2 regions. RNCs were purified as described before.

8.2.6. Isolation of 80S ribosomes

Eukaryotic 80S ribosomes were purified from different yeast strains, applying basically the following protocol. The modified 80S-Ssb1 ribosomes were isolated the following way from the RPL25-Ssb1 fusion strain. Around 2 L of YPD were inoculated and grown until 1.4 OD₆₀₀. The cells were harvested (10 min at 5000 rpm, 4°C, GS3 rotor, washed with cold water and 1 % KCl. The pellet was resuspended in buffer PD and incubated for 15 min at RT. After centrifugation (10 min at 5000 rpm, 4°C, GS3 rotor), the cells were resuspended in 80S-lysis buffer and lysed with a three french press runs using a pressure of 18 kPsi. The lysate was centrifuged (15 min at 15,500 rpm, 4°C, SS-34 rotor)

and the supernatant was ultra-centrifuged (38 min at 37,000 rpm, 4°C, Ti70 rotor). The resulting supernatant was subsequently layered onto a 80S-sucrose cushion, composed of a 3 ml 2M 80S-sucrose cushion layered with 3 ml 1.5 M 80S-sucrose cushion, and ultra-centrifuged (20 h at 50,600 rpm, 4°C, Ti70 rotor). The ribosome pellets were resuspended in nuclease free H₂O, the concentration was determined at OD₂₆₀, 20 µl aliquots were flash frozen in liquid N₂ and stored at -80°C. The quality of the ribosome preparation was analyzed by SDS-PAGE and the fusion was additionally confirmed by western blot, using a poly-clonal anti-Ssb antibody serum (Rospert group).

8.2.7. Purification of RAC and SAXS analysis

RAC purification The protein complex RAC (Zuo and Ssz) was over-expressed in *E. coli* Rosetta 2 (DE3) cells (Chl), using two separate plasmids for each subunit of the complex (protocol from the Rospert group). Around 50µl of electro-competent *E. coli* cells were transformed by electroporation with a 2.5 kV pulse (0.2 cm Gene Pulser cuvette, BioRad, USA), using the two plasmids pETcoco2-Zuo1(Amp) and pET28N-Ssz1(Kan), encoding for Zuotin and Ssz, respectively (plasmids were a kind gift of the Rospert group in Freiburg). Immediately 1 ml of cold LB media was added and the cells were incubated for 30 to 45 min at 37°C, for recovery. The cells were harvested in a tabletop centrifuge at 4000 rpm and resuspended in 100 µl fresh LB media. Cells were plated for selective growth on LB plates, containing in the case of RAC over-expression the three antibiotics kanamycin (Kan), ampicillin (Amp) and chloramphenicol (Chl), and incubated overnight at 37°C.

RAC was co-purified in a four step protocol without a tag, using basically a previously described protocol with minor changes (Conz et al., 2007). After selective growth on LB plates, *E. coli* cells from the LB plate were used to inoculate 10 ml overnight cultures. These pre-cultures were then used to inoculate 1L expression cultures with OD(start)₆₀₀ of around 0.05. The cells grew at 37°C and the expression was induced at an OD₆₀₀ of 0.5 - 0.7 by adding IPTG (Roth) to a final concentration of 0.5 - 1 mM to the cultures. Then the cells grew further at 26°C and were harvested after 4 hours of growth by centrifugation runs (4000 rpm, 10 min, SLC-6000 rotor, Sorvall). The cells were resuspended once in LB media and the cell pellets were flash frozen in liquid nitrogen and stored at -80°C. The RAC *E. coli* cell pellets were thawed and resuspended in 1 ml RAC-lysis buffer per 1 g cell pellet, on ice. Lysozyme (Sigma-Aldrich), using 1 mg/ml final concentration, was added and the cells were incubated for 30 min. The cells were lysed using at least three fresh press runs (18 kpsi, Microfluidics, USA) or by

sonification (9 cycles each 20 s (35 - 40 %) with a cooling step after each cycle of 20 - 30 s, HD200, Bandelin, Germany). The lysate was treated with 1 μ l nuclease (benzonase, Sigma-Aldrich) and the cells were incubated for 10 min at RT and 20 min on ice. The lysate was cleared by two centrifugation steps (1.: 18.000 rpm, 15 min, SS-34 rotor; 2.: 18.000 rpm, 5 min, SS-34 rotor). The remaining supernatant was filtered (0.45 μ m filter, Millex-HA, Millipore) and the cleaned lysate was loaded onto a 6 ml Resource Q anion-exchange column (GE Healthcare) using an ÄKTA purifier system (ÄKTA, Sweden). Samples were eluted with an 0 - 40 % linear salt gradient (0 - 800 mM KOAc, using ion exchange buffer1 and 2). After analysis of the peak fraction by SDS-PAGE, the fractions were pooled and diluted with ion exchange buffer1 to a final concentration of 200 mM KOAc, to decrease the salt concentration for the next step. The pooled RAC containing fractions were loaded onto a second anion-exchange column (POROS HQ 20) and RAC was eluted by a 10 - 80 % linear KOAc gradient (200 - 1600 mM KOAc, using ion exchange buffer1 and 2). After analysis of the peak fraction by SDS-PAGE, the RAC fractions were pooled and adjusted to around 100 mM KOAc with ion exchange buffer1. The diluted RAC fraction was loaded onto a cation-exchange column (POROS HS 20), and RAC was eluted with a 0 - 60 % linear KOAc gradient (0 - 1200 mM KOAc, using ion exchange buffer1 and 2). Peak fractions were analyzed, pooled and concentrated to a RAC concentration of about 3-5 mg/ml using centrifuge filter devices with a molecular weight cut-off of 10 kDa (Amicon Ultra-4, Millipore; 1500 rpm in a 4444 rotor, Hettich centrifuge). The protein concentration was measured at λ_{280} and the concentrated eluate was loaded onto a Superdex 200 10/300 GL gel filtration column (GE Healthcare), using the gel filtration buffer. Finally, the peak fraction was analyzed by SDS-PAGE and the protein was stored at -80°C.

SAXS analysis SAXS datasets for RAC and the deletion mutant were collected at the DESY in Hamburg (Bio-SAXS beamline, EMBL) with the help of Gregor Witte (Hopfner group). The raw data, including the one-dimensional scattering curves, were initially processed with the software packages PRIMUS and GNOM (Konarev et al., 2003; Semenyuk & Svergun, 1991). The program PRIMUS was used for data reduction. Then data regularization was done with the program GNOM. The first *ab initio* structure calculation was done the software DAMMIN (Svergun, 1999; Volkov & Svergun, 2003), which calculates a model by densely packed dummy atoms (beads). Afterwards the program GASBOR (Svergun, 2001) was used to calculate detailed models, where each residue is represented by a dummy residue that results in a chain compatible model.

component	amount per reaction
yeast 80S RNCs	1-1.5 pmol
RAC	10 x excess over 80S
Ssb1	10 x excess over 80S
100K-BA buffer	ad 25 μ l volume

Table 8.: Example of a typical 25 μ l reconstitution reaction.

Each dummy residue aims to be positioned approximately at the C α atom of the protein structure.

8.3. Reconstitution experiments

Reconstitution experiments (also called binding or pelleting assay) were used to analyze co-pelleting of ribosome-binding factors with 80S ribosomes. The basic experimental setup was in case of the RAC binding assays as follows: first, the components were added stepwise to a low (e.g. 100K-BA buffer) or high salt buffer (same as 100K-BA buffer but with 300-500 mM KOAc) and incubated for 10 min at RT and 10 min on ice, then the 25 μ l reconstitution reaction was loaded onto 600 μ l of a 750 mM sucrose cushion and centrifuged (135 min at 40,000 rpm, 4°C, SW-55 Ti rotor), to pellet the ribosomes. After centrifugation, the tubes (Beckman Coulter) were immediately flash frozen in liquid N₂ and cut into two parts with a scalpel. All reactions were TCA precipitated and analyzed by SDS-PAGE followed by SYPRO orange staining.

80S RNC RAC complexes The 80S DPAP-RNC RAC-Ssb1 complex was reconstituted in a 25 μ l reaction, using 1.4 pmol 80S DPAP120 RNCs, 10 pmol RAC, 10 pmol Ssb1 and 100K-BA buffer, containing 1 mM AMPPNP. The wg80S mRAC complex was reconstituted with 3 pmol DPAP90-RNCs, 30 pmol mRAC and 100 K-BA buffer, including 1 mM AMPPNP. To reconstitute the 80S rpL25-Ssb1 RAC complex, 2 pmol of 80S rpL25-Ssb1 ribosomes were incubated with 20 pmol of RAC and 100K-BA buffer.

60S-eIF6 complex The sample for cryo-EM analysis was prepared by incubation (10 min at RT) of \sim 2 pmol gradient-purified 60S subunits with \sim 10 pmol of purified eIF6. The 60S-eIF6 complex was reconstituted in buffer A containing 100 mM KCl. The reconstituted samples were immediately applied to the grid and flash frozen in liquid ethane using a computer controlled automated vitrobot system (FEI).

9. Cryo electron microscopy

9.1. Negative stain electron microscopy

Negative stain EM was used to pre-analyze the samples before the grids were prepared for cryo-EM. The grid surfaces were cleaned with a plasma cleaner (Harrick Plasma, USA) at 0.22 Torr for 45 s. 3.5 μl of the sample were applied to a freshly cleaned grid and incubated for 45 s and the grid was then washed with five drops of water. After the washing step, the grid was stained with three drops of uranyl acetate (Ted Pella, Inc., USA) for 15 s and dried by carefully sliding blotting paper along the tweezers holding it. The grid was then allowed to dry on blotting paper for 5 min. Analysis of negative stain grids was done on a Spirit microscope (FEI Tecnai G12 Spirit 120 kV cryo-microscope) or on a Morgagni microscope (100 kV FEI Morgagni electron microscope) in Munich.

9.2. Data collection

3,5 μl of the reconstituted samples were applied to carbon coated holey grids as described (Grassucci et al., 2007). Datasets were collected on a FEI Tecnai F30 field emission gun cryo-microscope at 300 kV in Berlin (F30 microscope, Ultrastruktur Netzwerk) or on a FEI Tecnai G2 Spirit 120 kV cryo-microscope (Spirit microscope, Munich) under low dose conditions with $\sim 20 \text{ e}^-/\text{\AA}^2$ in a defocus range between 1.0 μm and 4.5 μm . The micrographs were developed and digitized on a Heidelberg drum scanner resulting in a pixel size of 1.24 $\text{\AA}/\text{pixel}$ on object scale.

9.3. Data processing

High resolution datasets of the Tecnai F30 microscope were pre-processed using the following main SPIDER (Frank et al., 1996) scripts in that order: 1. `p_ctffind.rib` (`byteswap.sh`, `p_readmrc.py`, `ctffind.sh`) uses CTFFIND (Mindell & Grigorieff, 2003) for CTF determination, 2. visual inspection of power spectra was done in WEB and the

micsuse file was cleaned for micrographs with bad quality power spectra, 3. the script `sig_decimate.rib` generated two times decimated micrographs converted to mrc format, which were used for half-automated SIGNATURE screening with the script `sig_pick.rib`, 4. screened micrographs were loaded in SIGNATURE (Chen & Grigorieff, 2007) and coordinates were saved for each particle of the micrograph, 5. these coordinates were used by the script `p_window.rib` (noise file, `p_convert_inline.rib`), to cut out single particles, 6. particles were filtered and decimated (`p_dcsfft.rib`) for visual selection of bad particles with WEB (Frank et al., 1996), 7. the script `p_copygood.rib` removed the bad particles from the overall dataset and renumbered the leftover particles, by moving them into good folders (good, goodparts and goodpartscoord folder), 9. the script `p_makedefgrpfile.rib` generates a defocusgroup file (`defgroup.rib`) out of the defocus file (`defocusfile.rib`), whereby the micrographs were grouped manually according to their defocus value.

Initial alignment Three fold decimated particles were initially aligned by the use of the script `p_alidef.rib`, using cross-correlation based projection matching technique (AP MQ command), whereby 83 reference projections of a template 3D volume were used, corresponding to an angular accuracy of 15° . The resulting `apmq` files contained for each particle the alignment information, comprising the best matching projection, an un-normalized CCC value, as well as the in-plane rotation angle and x,y-shifts in pixels. The rotation and shifts parameters were applied to generate a 3D reconstruction with the scripts `p_maketrans.rib`, `p_spinnem.rib` (`p_angles.rib`) and finally `bp3f_n.rib` (`ref_rotate.rib`; `trans-`, `angles` and `select` files and good folders as input) by backprojection of the particles. The resolution of each defocus group was calculated by comparing the backprojected volumes of the two random halfsets of each defocus group, the sub-volumes of each defocus group were CTF corrected and summarized to a final volume.

Refinement Large dataset were refined on a high performance Intel/Opteron computer cluster with several hundred processors. Refinement of the datasets was realized by iterative rounds of alignment and backprojection, whereby the masked and filtered output volume was used as input for the next refinement round, aiming to improve the resolution of the output 3D reconstruction. The `trans` files contained shifts and rotation parameters, which were applied to the original undecimated particles for backprojection to avoid a loss of information, if interpolation would be used. Filter parameter and alignment algorithms were varied, the angular increments and restrictions were succes-

sively decreased, resulting in a more accurate sampling of the projection space due to the increased number of compared reference projections. Supervised sorting was used to classify the datasets, e.g. in case of P-tRNA sorting was an un-programmed 80S volume used as reference.

Low resolution datasets were collected on a Tecnai Spirit cryo-microscope at 120 kV in Munich (Biozentrum). The work flow for Spirit datasets was the same as previously described for the processing of the Tecnai F30 data, but with the following variations: 1. inversion of the particle contrast was done with the script (`cp_to_negative.rib`), necessary for SIGNATURE, 2. no visual particle inspection was done, badly windowed particle were automatically removed by the script `p_edgepartscreen.rib`.

Interpretation and modeling Cryo-EM densities were isolated using binary masks. Initial docking of atomic structures and models into EM densities was done with the program Coot (Emsley et al., 2004). The generated models were in some cases refined and fitted with MDFF (Trabuco et al., 2008). The programs Chimera (Pettersen et al., 2004) and PyMol (<http://www.pymol.org>) were used to prepare figures. In the 80S RNC-Helix study, homology models for ribosomal proteins were built using MODELLER (Eswar et al., 2007), after protein alignment with T-Coffee (Notredame et al., 2000). Models were then adjusted manually with Coot and minimized with VMD (Humphrey et al., 1996).

9.3.1. Sorting of the datasets

All datasets were processed according to the workflow described before, using a supervised sorting strategy.

60S-eIF6 complex The dataset of the 60S-eIF6 complex was classified into two sub-datasets, with 31,000 particles in the 80S sub-dataset and 76,000 particles containing the 60S-eIF6 complex. Densities for the 60S subunit and eIF6 were isolated using binary masks.

80S Helix-RNCs Removal of empty ribosomal particles resulted in 120,000, 190,000 and 150,000 programmed particles for the 80S Helix1-RNC, 80S Helix2-RNC and 80S DPAP-RNC datasets, respectively. Densities for the 40S subunit, the 60S subunit and the P-site tRNA were isolated using binary masks. The homology model for the

(EAAAK)₅ helix was built on the basis of the HPLC6 sequence using HHPred server and fitted into to the assigned EM density.

80S RAC datasets The dataset of the wg80S RNC mRAC complex, with all together 59,000 particles, was sorted for the presence of P-tRNA, resulting in 47,000 particles for programmed and 12,000 particles for un-programmed 'empty' 80S ribosomes, respectively. The dataset of 80S DPAP-RNC RAC-Ssb1 dataset with 50,000 particles was sorted first for ES27 density, resulting in 34,000 particles for the ES27 in L1 conformation and 16,000 particles and its exit conformation, respectively. The ES27-L1 sub-dataset was further classified for the presence of RAC density, revealing that around 18,000 particles with present showing additional RAC density and 16,000 particles did not show extra ligand density, respectively. The Spirit dataset of the 80S rpL25-Ssb1 RAC complex with overall around 14,000 particles was sorted for the presence of the two distinct ES27 conformations, resulting in 3,100 and 10,700 particles for the ES27 in exit and L1 conformation, respectively.

Part IV.

Appendix

Index

- 80S-Ssb1 - 80S ribosomes with N-terminal fusion of Ssb1 to rpL25, 52
- aa - amino acid(s), 8
- CCC- Cross-correlation coefficient, 21
- CCD - charge-coupled device, 18
- CCF - cross-correlation function, 19
- cryo-EM - cryo-electron microscopy, 6
- CTF - contrast transfer function, 19
- DLS - dynamic light scattering, 46
- DPAP - Dipeptidyl aminopeptidase of yeast, 49
- DPAP-B - dipeptidyl-aminopeptidase B from yeast, 34
- Efl1 - elongation factor-like 1 (Efl1p in yeast), 10
- eIF6 - eukaryotic translation initiation factor 6, 9
- EM - electron microscopy, 75
- ES27 - eukaryotic expansion segment 27 of the 28S rRNA, 54
- FSC - Fourier shell correlation, 21
- IVT - *in vitro* translation reaction, 70
- kDa - kilo Dalton, 17
- KOAc - potassium acetate, 65
- mRAC - mammalian ribosome associated complex (MPP11 and Hsp70L1), 15
- mRNA - messenger RNA, 8
- MW - molecular weight, 8
- NAC - nascent polypeptide-associated complex, 14
- nascent chain - nascent polypeptide chain of the translating ribosome, 45
- NBD - nucleotide binding domain, 14
- NEFs - nucleotide exchange factors, 15
- PCR - Polymerase chain reaction, 64
- PDF - peptidyl deformylase, 61
- PIP - complete protease inhibitor pill (Roche), 65
- PTC - peptidyl transferase center, 8
- RAC - ribosome associated complex, 15
- RACK1 - Receptor for activated protein kinase C, 10
- RAC Δ Zuo110 - complex of the first 110 aa of Zuo and Ssz, 47
- RPBs - ribosome-associated protein biogenesis factors, 15

- rpL23 - eukaryotic ribosomal protein L23 of large subunit (L14 in *E. coli* and RpL23p in *S. cerevisiae* nomenclature), 25
- rpL24 - eukaryotic ribosomal protein L24 of large subunit (RpL24p in *S. cerevisiae* nomenclature; no bacterial homolog), 27
- rRNA - ribosomal RNA, 10
- RT - room temperature, 25
- S - Svedberg constant, unit, 8
- S. cerevisiae* - *Saccharomyces cerevisiae* (species of budding yeast; baker's yeast), 15
- SAXS - small angle X-ray scattering, 45
- SBD - substrate binding domain, 14
- SBDS - Shwachman-Bodian-Diamond syndrome, 10
- SDS-PAGE - sodium dodecyl sulfate polyacrylamide gel electrophoresis, 66
- SNR - signal-to-noise ratio, 17
- SRL - sarcin-ricin loop, 27
- SRP - signal recognition particle, 15
- Ssb - Ssb1p and Ssb2p in *S. cerevisiae*, 14
- TEM - transmission electron microscope, 18
- TF - Trigger factor, 13
- WB - Western Blot, 68
- wg80S/wgRNC - 80S ribosomes or RNCs from wheat germ (*Triticum aestivum*), 49
- y80S/yRNCs - 80S ribosomes or RNCs from yeast, 50
- YTE - yeast translation extract, 69

Bibliography

- Adams, H., Scotti, P. A., De Cock, H., Luirink, J. & Tommassen, J. (2002). *European journal of biochemistry / FEBS* 269, 5564–5571.
- Arai, R., Ueda, H., Kitayama, A., Kamiya, N. & Nagamune, T. (2001). *Protein engineering* 14, 529–532.
- Ban, N., Nissen, P., Hansen, J., Moore, P. B. & Steitz, T. A. (2000). *Science* 289, 905–920.
- Barral, J. M., Broadley, S. A., Schaffar, G. & Hartl, F. U. (2004). *Seminars in cell & developmental biology* 15, 17–29.
- Basu, U., Si, K., Deng, H. & Maitra, U. (2003). *Molecular and cellular biology* 23, 6187–6199.
- Beatrix, B., Sakai, H. & Wiedmann, M. (2000). *J Biol Chem* 275, 37838–37845.
- Beckmann, R., Bubeck, D., Grassucci, R., Penczek, P., Verschoor, A., Blobel, G. & Frank, J. (1997). *Science (New York, N.Y.)* 278, 2123–2126.
- Beckmann, R., Spahn, C. M., Eswar, N., Helmers, J., Penczek, P. A., Sali, A., Frank, J. & Blobel, G. (2001). *Cell* 107, 361–372.
- Benelli, D., Marzi, S., Mancone, C., Alonzi, T., la Teana, A. & Londei, P. (2009). *Nucleic acids research* 37, 256–267.
- Berk, V., Zhang, W., Pai, R. D., Cate, J. H. & Cate, J. H. (2006). *Proceedings of the National Academy of Sciences of the United States of America* 103, 15830–15834.
- Bingel-Erlenmeyer, R., Kohler, R., Kramer, G., Sandikci, A., Antolić, S., Maier, T., Schaffitzel, C., Wiedmann, B., Bukau, B. & Ban, N. (2008). *Nature* 452, 108–111.
- Blaha, G., Stanley, R. E. & Steitz, T. A. (2009). *Science (New York, N.Y.)* 325, 966–970.

- Blobel, J., Bernadó, P., Svergun, D. I., Tauler, R. & Pons, M. (2009). *Journal of the American Chemical Society* 131, 4378–4386.
- Ceci, M., Gaviraghi, C., Gorrini, C., Sala, L. A., Offenhäuser, N., Marchisio, P. C. & Biffo, S. (2003). *Nature* 426, 579–584.
- Chen, J. Z. & Grigorieff, N. (2007). *Journal of structural biology* 157, 168–173.
- Chen, J. Z., Settembre, E. C., Aoki, S. T., Zhang, X., Bellamy, A. R., Dormitzer, P. R., Harrison, S. C. & Grigorieff, N. (2009). *Proceedings of the National Academy of Sciences of the United States of America* 106, 10644–10648.
- Chendrimada, T. P., Finn, K. J., Ji, X., Baillat, D., Gregory, R. I., Liebhaber, S. A., Pasquinelli, A. E. & Shiekhattar, R. (2007). *Nature* 447, 823–828.
- Cohen, E., Bieschke, J., Perciavalle, R. M., Kelly, J. W. & Dillin, A. (2006). *Science (New York, N.Y.)* 313, 1604–1610.
- Conz, C., Otto, H., Peisker, K., Gautschi, M., Wölflé, T., Mayer, M. P. & Rospert, S. (2007). *The Journal of biological chemistry* 282, 33977–33984.
- Cruz-Vera, L. R., Rajagopal, S., Squires, C. & Yanofsky, C. (2005). *Molecular cell* 19, 333–343.
- Dalley, J. A., Selkirk, A. & Pool, M. R. (2008). *Molecular biology of the cell* 19, 2876–2884.
- Deuerling, E., Schulze-Specking, A., Tomoyasu, T., Mogk, A. & Bukau, B. (1999). *Nature* 400, 693–696.
- Dragovic, Z., Broadley, S. A., Shomura, Y., Bracher, A. & Hartl, F. U. (2006). *The EMBO journal* 25, 2519–2528.
- Ellis, R. J. & Hartl, F. U. (1999). *Curr Opin Struct Biol* 9, 102–110.
- Emsley, P., Cowtan & K. (2004). *Acta Crystallographica Section D: Biological Crystallography* 60, 2126–2132.
- Eswar, N., Webb, B., Marti-Renom, M. A., Madhusudhan, M. S., Eramian, D., Shen, M.-Y. Y., Pieper, U. & Sali, A. (2007). *Current protocols in protein science / editorial board, John E. Coligan ... [et al.] Chapter 2.*

- Ferbitz, L., Maier, T., Patzelt, H., Bukau, B., Deuerling, E. & Ban, N. (2004). *Nature* 431, 590–596.
- Frank, J. (2002). *Annual Review of Biophysics and Biomolecular Structure* 31, 303–319.
- Frank, J. (2006). *Three-dimensional electron microscopy of macromolecular assemblies: Visualization of biological molecules in their native state*. Oxford.
- Frank, J., Radermacher, M., Penczek, P., Zhu, J., Li, Y., Ladjadj, M. & Leith, A. (1996). *Journal of Structural Biology* 116, 190–199.
- Frank, J., Zhu, J., Penczek, P., Li, Y., Srivastava, S., Verschoor, A., Radermacher, M., Grassucci, R., Lata, R. K. & Agrawal, R. K. (1995). *Nature* 376, 441–444.
- Frydman, J. (2001). *Annual review of biochemistry* 70, 603–647.
- Fu, J., Gao, H. & Frank, J. (2007). *Journal of structural biology* 157, 226–239.
- Fünfschilling, U. & Rospert, S. (1999). *Molecular biology of the cell* 10, 3289–3299.
- Gandin, V., Miluzio, A., Barbieri, A. M., Beugnet, A., Kiyokawa, H., Marchisio, P. C. & Biffo, S. (2008). *Nature* 455, 684–688.
- Gao, Y.-G. G., Selmer, M., Dunham, C. M., Weixlbaumer, A., Kelley, A. C. & Ramakrishnan, V. (2009). *Science (New York, N.Y.)* 326, 694–699.
- Gautschi, M., Lilie, H., Fünfschilling, U., Mun, A., Ross, S., Lithgow, T., Rücknagel, P. & Rospert, S. (2001). *Proceedings of the National Academy of Sciences of the United States of America* 98, 3762–3767.
- Gautschi, M., Mun, A., Ross, S. & Rospert, S. (2002). *Proceedings of the National Academy of Sciences of the United States of America* 99, 4209–4214.
- Giglione, C., Fieulaine, S. & Meinnel, T. (2009). *Trends in biochemical sciences* 34, 417–426.
- Gong, F. & Yanofsky, C. (2002). *Science (New York, N.Y.)* 297, 1864–1867.
- Graindorge, J. S., Rousselle, J. C., Senger, B., Lenormand, P., Namane, A., Lacroute, F. & Fasiolo, F. (2005). *Journal of molecular biology* 352, 355–369.
- Grassucci, R. A., Taylor, D. J. & Frank, J. (2007). *Nature protocols* 2, 3239–3246.

- Green, R. & Noller, H. F. (1997). *Annual review of biochemistry* 66, 679–716.
- Grigorieff, N. (2007). *Journal of structural biology* 157, 117–125.
- Groft, C. M., Beckmann, R., Sali, A. & Burley, S. K. (2000). *Nature structural biology* 7, 1156–1164.
- Halic, M., Becker, T., Pool, M. R., Spahn, C. M., Grassucci, R. A., Frank, J. & Beckmann, R. (2004). *Nature* 427, 808–814.
- Halic, M., Blau, M., Becker, T., Mielke, T., Pool, M. R., Wild, K., Sinning, I. & Beckmann, R. (2006a). *Nature* 444, 507–511.
- Halic, M., Gartmann, M., Schlenker, O., Mielke, T., Pool, M. R., Sinning, I. & Beckmann, R. (2006b). *Science* 312, 745–747.
- Hardesty, B. & Kramer, G. (2001). *Progress in nucleic acid research and molecular biology* 66, 41–66.
- Harris, M. N., Ozpolat, B., Abdi, F., Gu, S., Legler, A., Mawuenyega, K. G., Tirado-Gomez, M., Lopez-Berestein, G. & Chen, X. (2004). *Blood* 104, 1314–1323.
- Hartl, F. U. & Hayer-Hartl, M. (2002). *Science* 295, 1852–1858.
- Hessa, T., Kim, H., Bihlmaier, K., Lundin, C., Boekel, J., Andersson, H., Nilsson, I., White, S. H. & von Heijne, G. (2005). *Nature* 433, 377–381.
- Hessa, T., Meindl-Beinker, N. M., Bernsel, A., Kim, H., Sato, Y., Lerch-Bader, M., Nilsson, I., White, S. H. & von Heijne, G. (2007). *Nature* 450, 1026–1030.
- Hesterkamp, T., Hauser, S., Lütcke, H. & Bukau, B. (1996). *Proceedings of the National Academy of Sciences of the United States of America* 93, 4437–4441.
- Hohn, M., Tang, G., Goodyear, G., Baldwin, P. R., Huang, Z., Penczek, P. A., Yang, C., Glaeser, R. M., Adams, P. D. & Ludtke, S. J. (2007). *Journal of structural biology* 157, 47–55.
- Horseley, E. W., Jakovljevic, J., Miles, T. D., Harnpicharnchai, P. & Woolford, J. L. (2004). *RNA (New York, N.Y.)* 10, 813–827.
- Horwich, A. L., Fenton, W. A., Chapman, E. & Farr, G. W. (2007). *Annu Rev Cell Dev Biol* 23, 115–145.

- Huang, P., Gautschi, M., Walter, W., Rospert, S. & Craig, E. A. (2005). *Nature structural & molecular biology* 12, 497–504.
- Humphrey, W., Dalke, A. & Schulten, K. (1996). *Journal of molecular graphics* 14.
- Hundley, H., Eisenman, H., Walter, W., Evans, T., Hotokezaka, Y., Wiedmann, M. & Craig, E. (2002). *Proceedings of the National Academy of Sciences of the United States of America* 99, 4203–4208.
- Hurt, E., Hannus, S., Schmelzl, B., Lau, D., Tollervey, D. & Simos, G. (1999). *The Journal of cell biology* 144, 389–401.
- Jiang, J., Prasad, K., Lafer, E. M. & Sousa, R. (2005). *Molecular cell* 20, 513–524.
- Kaiser, C. M., Chang, H. C., Agashe, V. R., Lakshmiathy, S. K., Etchells, S. A., Hayer-Hartl, M., Hartl, F. U. & Barral, J. M. (2006). *Nature* 444, 455–460.
- Konarev, P. V., Volkov, V. V., Sokolova, A. V., Koch, M. H. J. & Svergun, D. I. (2003). *Journal of Applied Crystallography* 36, 1277–1282.
- Korostelev, A., Trakhanov, S., Laurberg, M. & Noller, H. F. (2006). *Cell* 126, 1065–1077.
- Kosolapov, A. & Deutsch, C. (2009). *Nature structural & molecular biology* 16, 405–411.
- Kosolapov, A., Tu, L., Wang, J. & Deutsch, C. (2004). *Neuron* 44, 295–307.
- Kramer, G., Boehringer, D., Ban, N. & Bukau, B. (2009). *Nature structural & molecular biology* 16, 589–597.
- Laemmli, U. K. (1970). *Nature* 227, 680–685.
- Lebreton, A., Saveanu, C., Decourty, L., Rain, J. C., Jacquier, A. & Fromont-Racine, M. (2006). *The Journal of cell biology* 173, 349–360.
- Liepinsh, E., Otting, G., Harding, M. M., Ward, L. G., Mackay, J. P. & Haymet, A. D. (2002). *European journal of biochemistry / FEBS* 269, 1259–1266.
- Liu, Q. & Hendrickson, W. A. (2007). *Cell* 131, 106–120.
- Lu, J. & Deutsch, C. (2005a). *Biochemistry* 44, 8230–8243.
- Lu, J. & Deutsch, C. (2005b). *Nature Structural & Molecular Biology* 12, 1123–1129.

- Lu, J. & Deutsch, C. (2008). *Journal of molecular biology* 384, 73–86.
- Lu, J., Kobertz, W. R. & Deutsch, C. (2007). *Journal of molecular biology* 371, 1378–1391.
- Ludtke, S. J., Baker, M. L., Chen, D.-H., Song, J.-L., Chuang, D. T. & Chiu, W. (2008). *Structure* 16, 441–448.
- Marqusee, S. & Baldwin, R. L. (1987). *Proceedings of the National Academy of Sciences of the United States of America* 84, 8898–8902.
- Martin, J. & Hartl, F. U. (1997). *Proceedings of the National Academy of Sciences of the United States of America* 94, 1107–1112.
- Menne, T. F., Goyenechea, B., Sánchez-Puig, N., Wong, C. C., Tonkin, L. M., Ancliff, P. J., Brost, R. L., Costanzo, M., Boone, C. & Warren, A. J. (2007). *Nature Genetics* 39, 486–495.
- Miluzio, A., Beugnet, A., Volta, V. & Biffo, S. (2009). *EMBO reports* 10, 459–465.
- Mindell, J. A. & Grigorieff, N. (2003). *Journal of structural biology* 142, 334–347.
- Minton, A. P. (2000). *Current opinion in structural biology* 10, 34–39.
- Morgan, D. G., Ménétret, J. F., Radermacher, M., Neuhof, A., Akey, I. V., Rapoport, T. A. & Akey, C. W. (2000). *Journal of molecular biology* 301, 301–321.
- Nakatogawa, H. & Ito, K. (2002). *Cell* 108, 629–636.
- Notredame, C., Higgins, D. G. & Heringa, J. (2000). *Journal of molecular biology* 302, 205–217.
- Otto, H., Conz, C., Maier, P., Wölfe, T., Suzuki, C. K., Jenö, P., Rücknagel, P., Stahl, J. & Rospert, S. (2005). *Proceedings of the National Academy of Sciences of the United States of America* 102, 10064–10069.
- Patzelt, H., Rüdiger, S., Brehmer, D., Kramer, G., Vorderwülbecke, S., Schaffitzel, E., Waitz, A., Hesterkamp, T., Dong, L., Schneider-Mergener, J., Bukau, B. & Deuerling, E. (2001). *Proceedings of the National Academy of Sciences of the United States of America* 98, 14244–14249.

- Peisker, K., Braun, D., Wölfe, T., Hentschel, J., Fünfschilling, U., Fischer, G., Sickmann, A. & Rospert, S. (2008). *Molecular biology of the cell* 19, 5279–5288.
- Penczek, P. A., Frank, J. & Spahn, C. M. (2006). *Journal of structural biology* 154, 184–194.
- Penczek, P. A., Grassucci, R. A. & Frank, J. (1994). *Ultramicroscopy* 53, 251–270.
- Penczek, P. A., Yang, C., Frank, J. & Spahn, C. M. (2006). *Journal of structural biology* 154, 168–183.
- Pettersen, E. F., Goddard, T. D., Huang, C. C., Couch, G. S., Greenblatt, D. M., Meng, E. C. & Ferrin, T. E. (2004). *Journal of computational chemistry* 25, 1605–1612.
- Pfund, C., Huang, P., Lopez-Hoyo, N. & Craig, E. A. (2001). *Molecular biology of the cell* 12, 3773–3782.
- Pfund, C., Lopez-Hoyo, N., Ziegelhoffer, T., Schilke, B. A., Lopez-Buesa, P., Walter, W. A., Wiedmann, M. & Craig, E. A. (1998). *The EMBO journal* 17, 3981–3989.
- Polier, S., Dragovic, Z., Hartl, F. U. & Bracher, A. (2008). *Cell* 133, 1068–1079.
- Radermacher, M., Wagenknecht, T., Verschoor, A. & Frank, J. (1987). *Journal of microscopy* 146, 113–136.
- Raine, A., Lovmar, M., Wikberg, J. & Ehrenberg, M. (2006). *The Journal of biological chemistry* 281, 28033–28038.
- Ramakrishnan, V. (2002). *Cell* 108, 557–572.
- Raue, U., Oellerer, S. & Rospert, S. (2007). *The Journal of biological chemistry* 282, 7809–7816.
- Raviol, H., Sadlish, H., Rodriguez, F., Mayer, M. P. & Bukau, B. (2006). *The EMBO journal* 25, 2510–2518.
- Rossmann, M. G., Morais, M. C., Leiman, P. G. & Zhang, W. (2005). *Structure* 13, 355–362.
- Rüdiger, S., Germeroth, L., Schneider-Mergener, J. & Bukau, B. (1997). *The EMBO journal* 16, 1501–1507.

- Russell, D. W. & Spremulli, L. L. (1979). *J. Biol. Chem.* 254, 8796–8800.
- Rutkowska, A., Mayer, M. P., Hoffmann, A., Merz, F., Zachmann-Brand, B., Schaffitzel, C., Ban, N., Deuerling, E. & Bukau, B. (2008). *The Journal of biological chemistry* 283, 4124–4132.
- Saibil, H. R. (2008). *Current opinion in structural biology* 18, 35–42.
- Sali, A., Potterton, L., Yuan, F., van Vlijmen, H. & Karplus, M. (1995). *Proteins* 23, 318–326.
- Sanvito, F., Piatti, S., Villa, A., Bossi, M., Lucchini, G., Marchisio, P. C. & Biffo, S. (1999). *The Journal of cell biology* 144, 823–837.
- Sanvito, F., Vivoli, F., Gambini, S., Santambrogio, G., Catena, M., Viale, E., Veglia, F., Donadini, A., Biffo, S. & Marchisio, P. C. (2000). *Cancer research* 60, 510–516.
- Schluenzen, F., Tocilj, A., Zarivach, R., Harms, J., Gluehmann, M., Janell, D., Bashan, A., Bartels, H., Agmon, I., Franceschi, F. & Yonath, A. (2000). *Cell* 102, 615–623.
- Schlünzen, F., Wilson, D. N., Tian, P., Harms, J. M., McInnes, S. J., Hansen, H. A., Albrecht, R., Buerger, J., Wilbanks, S. M. & Fucini, P. (2005). *Structure (Camb)* 13, 1685–1694.
- Schmeing, T. M., Huang, K. S., Strobel, S. A. & Steitz, T. A. (2005). *Nature* 438, 520–524.
- Schmeing, T. M., Voorhees, R. M., Kelley, A. C., Gao, Y.-G. G., Murphy, F. V., Weir, J. R. & Ramakrishnan, V. (2009). *Science (New York, N.Y.)* 326, 688–694.
- Schuermann, J. P., Jiang, J., Cuellar, J., Llorca, O., Wang, L., Gimenez, L. E., Jin, S., Taylor, A. B., Demeler, B., Morano, K. A., Hart, P. J., Valpuesta, J. M., Lafer, E. M. & Sousa, R. (2008). *Molecular cell* 31, 232–243.
- Schuette, J.-C. C., Murphy, F. V., Kelley, A. C., Weir, J. R., Giesebrecht, J., Connell, S. R., Loeke, J., Mielke, T., Zhang, W., Penczek, P. A., Ramakrishnan, V. & Spahn, C. M. (2009). *The EMBO journal* 28, 755–765.
- Schuwirth, B. S., Borovinskaya, M. A., Hau, C. W., Zhang, W., Vila-Sanjurjo, A., Holton, J. M. & Cate, J. H. (2005). *Science (New York, N.Y.)* 310, 827–834.

- Selmer, M., Dunham, C. M., Murphy, F. V., Weixlbaumer, A., Petry, S., Kelley, A. C., Weir, J. R. & Ramakrishnan, V. (2006). *Science* (New York, N.Y.) 313, 1935–1942.
- Semenyuk, A. V. & Svergun, D. I. (1991). *Journal of Applied Crystallography* 24, 537–540.
- Senger, B., Lafontaine, D. L., Graindorge, J. S., Gadai, O., Camasses, A., Sanni, A., Garnier, J. M., Breitenbach, M., Hurt, E. & Fasiolo, F. (2001). *Molecular cell* 8, 1363–1373.
- Si, K. & Maitra, U. (1999). *Molecular and cellular biology* 19, 1416–1426.
- Sicheri, F. & Yang, D. S. (1995). *Nature* 375, 427–431.
- Söding, J., Biegert, A. & Lupas, A. N. (2005). *Nucleic Acids Res* 33.
- Sonenberg, N. & Hinnebusch, A. G. (2009). *Cell* 136, 731–745.
- Sorzano, C. O., Marabini, R., Velázquez-Muriel, J., Bilbao-Castro, J. R., Scheres, S. H., Carazo, J. M. & Pascual-Montano, A. (2004). *Journal of structural biology* 148, 194–204.
- Spahn, C. M., Gomez-Lorenzo, M. G., Grassucci, R. A., Jørgensen, R., Andersen, G. R., Beckmann, R., Penczek, P. A., Ballesta, J. P. & Frank, J. (2004). *The EMBO journal* 23, 1008–1019.
- Spahn, C. M. & Penczek, P. A. (2009). *Current opinion in structural biology* 19, 623–631.
- Spahn, C. M. T., Beckmann, R., Eswar, N., Penczek, P. A., Sali, A., Blobel, G. & Frank, J. (2001). *Cell* 107, 373–386.
- Svergun, D. (1999). *Biophysical Journal* 76, 2879–2886.
- Svergun, D. (2001). *Biophysical Journal* 80, 2946–2953.
- Svergun, D. I., Burkhardt, N., Pedersen, J. S., Koch, M. H., Volkov, V. V., Kozin, M. B., Meerwink, W., Stuhrmann, H. B., Diedrich, G. & Nierhaus, K. H. (1997). *Journal of molecular biology* 271, 602–618.
- Tang, G., Peng, L., Baldwin, P., Mann, D., Jiang, W., Rees, I. & Ludtke, S. (2007). *Journal of Structural Biology* 157, 38–46.

- Tenson, T. & Ehrenberg, M. (2002). *Cell* 108, 591–594.
- Teter, S. A., Houry, W. A., Ang, D., Tradler, T., Rockabrand, D., Fischer, G., Blum, P., Georgopoulos, C. & Hartl, F. U. (1999). *Cell* 97, 755–765.
- Topf, M., Baker, M. L., Marti-Renom, M. A., Chiu, W. & Sali, A. (2006). *Journal of molecular biology* 357, 1655–1668.
- Topf, M., Lasker, K., Webb, B., Wolfson, H., Chiu, W. & Sali, A. (2008). *Structure* 16, 295–307.
- Trabuco, L. G., Villa, E., Mitra, K., Frank, J. & Schulten, K. (2008). *Structure (London, England : 1993)* 16, 673–683.
- Trabuco, L. G., Villa, E., Schreiner, E., Harrison, C. B. & Schulten, K. (2009). *Methods (San Diego, Calif.)* 49, 174–180.
- Valenzuela, D. M., Chaudhuri, A. & Maitra, U. (1982). *J. Biol. Chem.* 257, 7712–7719.
- van den Berg, B., Ellis, R. J. & Dobson, C. M. (1999). *The EMBO journal* 18, 6927–6933.
- van Heel, M., Harauz, G., Orlova, E. V., Schmidt, R. & Schatz, M. (1996). *J Struct Biol* 116, 17–24.
- Vazquez-Laslop, N., Thum, C. & Mankin, A. S. (2008). *Molecular cell* 30, 190–202.
- Volkov, V. V. & Svergun, D. I. (2003). *Journal of Applied Crystallography* 36, 860–864.
- Voss, N. R., Gerstein, M., Steitz, T. A. & Moore, P. B. (2006). *Journal of molecular biology* 360, 893–906.
- Walter, P., Ibrahimi & Blobel, G. (1981). *J. Cell Biol.* 91, 545–550.
- Wiedmann, B., Sakai, H., Davis, T. A. & Wiedmann, M. (1994). *Nature* 370, 434–440.
- Wimberly, B. T., Brodersen, D. E., Clemons, W. M., Morgan-Warren, R. J., Carter, A. P., Vornrhein, C., Hartsch, T. & Ramakrishnan, V. (2000). *Nature* 407, 327–339.
- Woolhead, C. A., McCormick, P. J. & Johnson, A. E. (2004). *Cell* 116, 725–736.
- Yonath, A. (2006). *Nature* 444, 435–436.

Zhang, X., Settembre, E., Xu, C., Dormitzer, P. R., Bellamy, R., Harrison, S. C. & Grigorieff, N. (2008). *Proceedings of the National Academy of Sciences* 105, 1867–1872.

CURRICULUM VITAE

PERSONAL PROFILE

Name Marco Gartmann
Date of birth 06.11.1979
Place of birth Eberswalde-Finow, Germany
Citizenship German
Marital status Single

EDUCATIONAL AND PRACTICAL TRAININGS

2006-2010 PhD thesis at the Gene Center Munich, Prof. Dr. Roland Beckmann, Ludwig-Maximilians-Universität (LMU) Munich
2005 Diploma thesis in the lab of Dr. Roland Beckmann, Berlin
“Untersuchungen zur Struktur und Funktion des SRP-Rezeptors”
2000-2005 Studies in Biochemistry, University Potsdam
1999-2000 Basic military service
1992-1999 Grammar school, Alexander von Humboldt Gymnasium, Eberswalde

LANGUAGES

German and English

PUBLICATIONS

Gartmann, M., Blau, M., Armache, J., Mielke, T., Topf, M., Beckmann, R. (2010). Mechanism of eIF6 mediated inhibition of ribosomal subunit joining. *JBC*, in press

Bhushan, S.*, **Gartmann, M.***, Halic, M., Armache, J., Jarasch, A., Mielke, T., Berninghausen, O., Wilson, D.W., Beckmann, R. (2010). alpha-helical nascent polypeptide chains visualized within distinct regions of the ribosomal exit tunnel. *Nature Struct Mol Biol.*, in press (*These authors contributed equally to this work)

Seidelt, B.*, Innis, C.A.*, Wilson, D.W., **Gartmann, M.**, Armache, J., Villa, E., Trabuco, L.G. Becker, T., Mielke, T., Schulten, K., Steitz, T.A., Beckmann, R. (2009). Structural Insight into Nascent Polypeptide Chain-Mediated Translational Stalling. *Science* **326** (5958), 1412-1415, (*These authors contributed equally to this work)

Kuhn, C.-D., Geiger, S.R., Baumli, S., **Gartmann, M.**, Gerber, J., Jennebach, S., Mielke, T. Tschochner, H., Beckmann, R., and Cramer, P. (2007). Functional Architecture of RNA Polymerase I. *Cell* **131** (7), 1260-1272.

Halic, M., **Gartmann, M.**, Schlenker, O., Mielke, T., Pool, M.R., Sinning, I., Beckmann, R.. (2006) Signal recognition particle receptor exposes the ribosomal translocon binding site. *Science* **312** (5774), 745-747

München, 04.12.2009

Marco Gartmann